

NOVEL ARCHITECTURES AND
FABRICATION TECHNIQUES FOR
DISTRIBUTED FEEDBACK LASERS FOR
COMMUNICATION

BEN JAMES SALMOND



A REPORT SUBMITTED AS PART OF THE REQUIREMENTS FOR THE DEGREE
OF DOCTOR OF PHILOSOPHY
AT THE SCHOOL OF PHYSICS AND ASTRONOMY
CARDIFF UNIVERSITY
CARDIFF, WALES

July 2025

Supervisors Dr. Samuel Shutts, Prof. Michael Wale, Dr. Wyn Meredith

Abstract

This thesis describes the development of laterally coupled (LC) distributed feedback (DFB) lasers on InP-based material. The first part of this work demonstrates the design, fabrication and measurement of high-order LC-DFBs using I-line photolithography. Measurements of devices revealed the successful demonstration of single-mode lasing, with a side mode suppression ratio (SMSR) of 25 dB observed. Some lateral mode instability, however, was noted as a result of broadening of the central ridge portion of the grating structures. The second part of this work was concerned with the comparison of varying the grating order LC-DFB laser diodes on both commercially grown quantum well (QW) material and InAs/InAlGaAs quantum dot (QD) material grown using metal organic chemical vapour deposition (MOCVD). A comparison of 3rd and 11th order LC-DFB devices revealed higher spectral purity in the high-order grating structures, achieving side mode suppression values exceeding 50 dB. 11th order devices were also compared on the two material systems. Sub-threshold gain measurements using the Cassidy method suggested that the QD material had an optical gain width almost 20 nm broader than the QW material. Spectral measurements of both devices also exhibited a significantly wider region of DFB mode operation for the QD device, by virtue of the broadened gain spectrum in the QD material system. The final portion of this work investigated the use of direct milling of 1st order grating structures using bismuth and gold focused ion beams (FIBs). Two types of structures were investigated, one where the gratings were milled directly on the ridge waveguide (RWG) and one where they were milled adjacent to the RWG. Various milling strategies were examined and it was found that off-ridge grating structures were simpler to define using this technique, with the concentric scanning routine offering the most desirable grating structures. Modelling work

predicted that the fabricated gratings would provide coupling strength values exceeding 70 cm^{-1} with a milled depth of 76 nm. This would be sufficient to achieve $kL = 2$ for cavity lengths as low as $300 \mu\text{m}$.

Acknowledgements

I would firstly like to thank my supervisor, Samuel Shutts, for giving me the opportunity to work on this project. I have thoroughly enjoyed working with him and his support and patience throughout this project as been invaluable to me. I would also like to thank my other supervisors, Michael Wale and Wyn Meredith, for their assistance and valuable discussions throughout this project.

I would next like to thank those who helped me learn cleanroom skills and fabrication. Firstly, Tom Peach, for teaching me so much about lithography and staying late on numerous occasions while my patterns finished in the EBPG. I would also like to thank Sara-Jayne Gillgrass, for sharing some of her fabrication knowledge and Zhongming Cao for his assistance on numerous occasions. I am also grateful for the support and training I received from the ICS staff.

I would also like to thank the staff at the UCSB nanofab, in particular, Dan Read, who taught me how to use the Raith Velion and made my trips to Santa Barbara thoroughly enjoyable.

Thanks to all the members of the optoelectronics group who have assisted me throughout my PhD, in particular, the technical staff who keep everything running smoothly. Special thanks also go to Tom Simpson, for his assistance with measurements in the final months of my project.

Finally I would also like to express my thanks to my friends from the CDT, the TRH and the Cardiff University Hiking Club. Also a special thanks go to my family, for providing unconditional support to me. In particular, I want to thank my Mum, Fiona. Her encouragement and effort over the years is a large part of what has led me to this point. For this, I dedicate this work to her.

List of Publications

Journal Articles

1. B. Salmond, D. D. John, W. J. Mitchell, B. J. Thibeault, T. Richter, A. Nadzeyka, P. Mazarov, F. Meyer, J. Fridmann, Y. Yu, M. Wale, W. Meredith, P. M. Snowton, D. Read and S. Shutts. *Fabricating distributed feedback laser gratings with bismuth and gold focused ion beams*. J. Vac. Sci. Technol. B **42**, 062214 (2024).

Conference Proceedings

1. Z. Cao, M. Alsayyadi, B. Salmond, H. Gordon-Moys, J. Nabialek, R. Forrest, C. P. Alford, B. Ratiu, O. Abouzaid, Q. Li, S. Shutts and P. M. Snowton. *C- and L-band InAs/InP quantum dot lasers*. IEEE Photonics Conference (IPC), 2022.
2. S. Shutts, Z. Cao, B. Ratiu, O. Abouzaid, M. Alsayyadi, J. Nabialek, B. Salmond, H. Gordon-Moys, C. P. Alford, S-J. Gillgrass, Q. Li and P. M. Snowton. *InAs quantum dots emitting in the C and L-wavelength band*. Novel In-Plane Semiconductor Lasers XXII, 2023.

Conference Presentations

1. B. Salmond, Z. Cao, S-J. Gillgrass, T. Peach, M. Wale, W. Meredith, P. M. Snowton and S. Shutts. *High-order gratings fabricated with mask-less projection lithography for distributed feedback lasers*. Semiconductors and Integrated Optoelectronics (SIOE), Cardiff, 2023. *Poster Presentation*.

2. B. Salmond, Z. Cao, S-J. Gillgrass, T. Peach, M. Wale, W. Meredith, P. M. Snowton and S. Shutts. *High-order distributed feedback lasers fabricated with mask-less projection lithography*. UK Semiconductors, Sheffield, 2023. *Oral Presentation*.
3. B. Salmond, T. Peach, D. Read, D. D. John, W. J. Mitchell, B. J. Thibeault, T. Richter, A. Nadzeyka, P. Mazarov, F. Meyer, J. Fridmann, Y. Yu, W. Meredith, M. Wale, P. M. Snowton and S. Shutts. *1st Order Gratings for Laterally Coupled DFB lasers Fabricated with E-Beam and Focused Ion Beam Lithography*. Semiconductors and Integrated Optoelectronics (SIOE), Cardiff, 2024. *Oral Presentation*.
4. B. Salmond, D. Read, D. D. John, W. J. Mitchell, B. J. Thibeault, T. Richter, A. Nadzeyka, P. Mazarov, F. Meyer, J. Fridmann, Y. Yu, W. Meredith, M. Wale, P. M. Snowton and S. Shutts. *Direct Fabrication of Gratings on Ridge Laser Structures Using Focused Bismuth Ion Beams*. The 68th International conference on Electron, Ion and Photon Beam Technology and Nanofabrication (EIPBN), San Diego, 2024. *Oral Presentation*.

Contents

Abstract	ii
Acknowledgements	iv
List of Publications	v
1 Introduction	1
1.1 Chapter List	4
2 Background	5
2.1 Basics of Semiconductor Laser Diode Operation	5
2.1.1 Components	5
2.1.2 Band Structures and Transitions	7
2.1.3 Optical Gain	8
2.1.4 The Fabry-Perot Laser Cavity	10
2.1.5 Typical Laser Structures	11
2.2 The Distributed Feedback Laser	14
2.2.1 Theoretical Basis - Coupled Mode Theory	14
2.2.2 Uniform Gratings	17

2.2.3	Strategies for Achieving Single Mode Lasing	18
2.2.4	Buried Grating DFB Lasers	20
2.2.5	Laterally-Coupled DFB Lasers	21
2.3	Summary	24
3	Design and Simulation of Laterally Coupled DFB Lasers	25
3.1	Overview	25
3.2	Fundamental Structure and Parameters	25
3.3	Traditional DFB Simulation Techniques	28
3.4	Effective Index Alteration Technique	29
3.5	Simulation Results from LC-DFB Lasers	32
3.5.1	Optical Mode Calculation	32
3.5.2	Etch Depth	34
3.5.3	Ridge Width	35
3.5.4	Extrusion Length	37
3.5.5	Duty Cycle	38
3.5.6	Transverse Mode Selection	40
3.5.7	Selection of Coupling Coefficient	41
3.6	Summary	43
4	Experimental Methods: Fabrication and Characterisation	44
4.1	Cleaning and Surface Preparation	44
4.1.1	Solvent Cleaning	45
4.1.2	Oxygen Ashing	45
4.1.3	Acid Surface Preparation	46

4.2	Lithography	46
4.2.1	Resist Preparation and Selection	47
4.2.2	Maskless Optical Projection Lithography	48
4.2.3	Electron Beam Lithography	49
4.3	Focused Ion Beam Nanofabrication	52
4.4	Etching	54
4.4.1	Plasma Assisted Etching	55
4.4.2	Inductively Coupled Plasma Etching	55
4.4.3	Etching Considerations	56
4.5	Planarisation	58
4.6	Vacuum Deposition	59
4.6.1	Physical Vapour Deposition	61
4.7	Device Preparation	62
4.8	Device Imaging and Checks	63
4.9	Characterisation	65
4.9.1	LIV Measurements	65
4.9.2	Wavelength Measurements	66
4.9.3	Near-Field Imaging	66
4.9.4	Gain Measurement	68
4.9.5	Reduced Temperature Measurements	69
4.10	Summary	71
5	11th Order C-band DFB lasers Fabricated with Projection Lithography	72
5.1	Overview	72

5.2	Motivation	72
5.3	Simulation and Design	74
5.4	Fabrication	77
5.4.1	Process Development	77
5.4.2	Fabrication Results	79
5.5	Device Results	85
5.5.1	Room Temperature LIV Results	85
5.5.2	Room Temperature Wavelength Results	86
5.5.3	LIV results with Varying Temperature	89
5.5.4	Wavelength results with Varying Temperature	90
5.6	Summary	93
6	Grating Order Effects on LC-DFB Lasers using QD and QW Material	95
6.1	Introduction	95
6.2	Motivation	96
6.2.1	Affects of Varying Grating Order	96
6.2.2	1550 nm Quantum Dot Lasers	96
6.3	Design	98
6.3.1	Material Structure	98
6.3.2	Device Design	99
6.4	Fabrication	101
6.4.1	Process flow	101
6.4.2	Electron Beam Lithography Process Development	102
6.4.3	Fabrication Results	104

6.5	Comparison of Grating Order	109
6.5.1	LIVT Results	109
6.5.2	Spectral Results	111
6.6	Comparison of 11 th Order QW and QD Devices	116
6.6.1	LIVT Results	116
6.6.2	Gain Measurements	118
6.6.3	Spectral Results	120
6.7	Summary	123
7	Direct Milling of LC-DFB Grating Structures Using Focused Bis-	
	muth and Gold Ions	125
7.1	Introduction	125
7.2	Motivation	125
7.3	Ridge Waveguide Preparation and Testing Methodology	128
7.4	Milling Parameters	128
7.5	On-Ridge Grating Structures	130
7.5.1	Single Pixel Line Scanning Routine	130
7.5.2	Cross-sections	131
7.5.3	Area Scanning Routine	133
7.6	Off-Ridge Grating Structures	135
7.6.1	Design and Simulation	135
7.6.2	Single Pixel Line Scanning	136
7.6.3	Area Scanning	138
7.6.4	Off-Ridge Grating Cross Sections	138
7.7	Summary	141

8	Conclusions and Future Work	143
8.1	Conclusions	143
8.2	Future Work	146
8.2.1	High Order LC-DFB Lasers	146
8.2.2	1 st Order LC-DFB Lasers	146
8.2.3	FIB Device Processing	147
8.2.4	QD DFB Laser Development	147
A	Process Flows	160
A.1	Process flow for Chapter 6	160
A.2	Process flow for Chapter 6	162

List of Tables

5.1	Ridge widths, extrusion lengths and designed coupling coefficient values of the devices fabricated in this chapter.	76
5.2	Variability of key parameters on G1 DFB devices across a 15x15 mm sample.	82
6.1	Design parameters chosen for the devices in this work.	100
6.2	Designed wavelength and grating pitches for the 9 channels fabricated in this work.	100
6.3	Measured device dimensions and recalculated coupling coefficients after completion of the fabrication process.	107
6.4	Measured tuning values with current and temperatures for varying order QW devices.	114
6.5	Measured tuning values and SMSR for the channel 1 11 th order QW and QD devices.	121
A.1	Detailed process flow for the fabrication of low open area LC-DFB lasers with projection lithography.	160
A.2	Detailed process flow for the fabrication of high open area LC-DFB lasers.	162

List of Figures

1.1	A conventional WDM link for optical communications.	3
2.1	A simplified schematic showing basic principles of a standard Fabry-Perot laser.	6
2.2	Simplified band structure showing (a) spontaneous emission and (b) stimulated emission.	7
2.3	Simplified schematics showing; (a) An oxide stripe gain guided laser and (b) A ridge waveguide (RWG) laser.	11
2.4	(a) DFB device structure and (b) DBR device structure.	14
2.5	Transmission spectra of DFB laser gratings. (a) $\alpha_0 L = 0$, (b) $\alpha_0 L = 0.66$, (c) $\alpha_0 L = 1$ and (d) Quarter wave phase shifted grating with $\alpha_0 L = 1$	18
2.6	A (a) facet view and (b) side view of a RWG buried grating DFB laser.	20
2.7	(a) Early LC-DFB laser presented in [28]. (b) Typical LC-DFB RWG laser structure.	21
3.1	Required grating pitch targeting wavelengths between 1500 and 1600 nm. In this case the effective refractive index is assumed to be 3.25.	26
3.2	(a) Cross-section of an example LC-DFB laser with grating regions shown in light grey. (b) Plan view of an example LC-DFB grating structure.	28

3.3	Normalised fundamental TE modes overlayed on the ridge waveguide cross sections that make up the LC-DFB laser structure. (a) narrow, (b) wide and (c) averaged.	30
3.4	The QW epitaxial structure used in this simulation chapter and throughout this work.	32
3.5	Refractive index profile of the 9QW epitaxial structure used in this work. Inset shows the region surrounding the 9QWs in the active region.	33
3.6	Calculated optical modes overlayed on an example LC-DFB cross section. (a) Fundamental mode, TE ₀₀ (b) 2nd bound mode, TE ₁₀	34
3.7	Coupling coefficient as a function of etch depth for both a 1 st and 3 rd order LC-DFB structure. The modelled ridge width was 2 μm, the extrusion length was set to 0.5 μm and the duty cycle was 0.5. The SCH and active regions are shown in yellow and red respectively.	35
3.8	Coupling coefficient as a function of ridge width for both a 1 st and 3 rd order LC-DFB structure.	36
3.9	Fundamental TE mode profiles shown with the ridge waveguide cross section for a ridge width of (a) 0.2 μm, (b) 0.7 μm and (c) 3.0 μm.	37
3.10	Coupling coefficient for a 1 st order grating as a function of extrusion length for a selection of ridge widths. The etch depth was 1.6 μm and the duty cycle was 0.5.	37
3.11	Coupling coefficient as a function of extrusion length for both a 3 rd and 11 th order LC-DFB laser structure. The ridge width was 2 μm, the etch depth was 1.6 μm and the duty cycle was 0.5.	39
3.12	Coupling coefficient as a function of duty cycle for a (a) 1 st order grating, (b) 2nd order grating, (c) 3 rd order grating and (d) 11 th order grating. The ridge width was 2 μm, the etch depth was 1.6 μm and the extrusion length was variable depending on grating order.	40

3.13	Coupling coefficient of both the fundamental TE mode and the second TE mode as a function of (a) extrusion length with a fixed ridge width of 2.5 μm and (b) ridge width with a fixed extrusion length of 0.2 μm . In both cases the etch depth was 1.6 μm and the duty cycle was 0.5.	41
4.1	Typical RWG lithography process flow. (a) Basic epitaxial structure, (b) Deposition of the hard mask, (c) Application of photoresist, (d) Exposure of the photoresist, exposed area is darker, (e) Development of the resist, leaving the patterned RWG.	47
4.2	Simplified schematic of the Heidelberg MLA150 maskless optical projection system used in this work.	49
4.3	Example of a stitching error that has been transferred to the epitaxial structure using an etch. The gap between two writefields has meant that a line has been left unexposed in the middle of the ridge/grating structure.	52
4.4	Simplified schematic showing the FIB column of the Raith Velion used in this work.	53
4.5	A typical RWG etching process. (a) Patterned RWG in resist, (b) Dry etch process to transfer the pattern into the hard mask, (c) Stripping of the resist to prepare for the epitaxial etch, (d) Etching of the epitaxial structure, (e) Removal of the remaining hard mask using a dry or wet etch process.	54
4.6	A BCB planarisation process. (a) RWG structure following the etch process, (b) Spin coating of the BCB dielectric, (c) Back etching of the BCB to reveal the top of the RWG.	59

4.7	A lift-off process for p-contact deposition. (a) Application of photoresist, (b) Exposure of the resist using photolithography, exposed areas are darker, (c) Development of the resist with the resist undercut shown, (d) Deposition of the p-contact using a line-of-sight technique, (e) Stripping of the resist to reveal the p-contact, (f) Deposition of the n-contact on the underside of the device following a substrate thinning procedure.	60
4.8	An example of a laser bar which has been lapped, cleaved, mounted and wirebonded. These devices are ready for measuring at this point.	63
4.9	An example of a near-field profile from a RWG laser diode. The FWHM can be used to estimate the current spreading for calculating current density.	67
4.10	Schematics showing the experimental set ups used in this work. (a) light current voltage temperature measurements, (b) spectral measurements and (c) near-field measurements.	70
5.1	Designed device structure for this work. The grating structure of InP is shown in grey, the separate confinement structure is shown in red and the dielectric window layer is shown in green.	75
5.2	Coupling coefficient as a function of extrusion length for the three ridge widths fabricated.	76
5.3	Result of attempting to pattern the ridge and grating structure in a single resist exposure in AZ2020 photoresist.	77
5.4	(a) Deposition of SiO ₂ hard mask. (b) Patterning of grating into AZ2020 photoresist. (c) Etching of grating pattern into oxide hard mask. (d) Patterning of ridge gap in AZ2020 photoresist. (e) Deposition of additional SiO ₂ hard mask for the ridge. (f) Completed hard mask including ridge and grating following lift-off procedure. (g) Completion of LC-DFB structure following ICP-RIE.	78

5.5	(a) Optical micrograph of the grating structure patterned in AZ2020 photoresist. (b) Scanning electron micrograph of the completed SiO ₂ hard mask following lift-off procedure. (c) Scanning electron micrograph of a RWG FP control device. (d) Top down scanning electron micrograph of a G1 DFB device following ICP-RIE. (e) G1 DFB device imaged on a 45° tilt.	80
5.6	Histograms describing the measurement of (a) duty cycle and (b) pitch for G1 DFB devices across a 15x15 mm sample.	82
5.7	Coupling coefficient for the average grating fabricated in this work as a function of duty cycle for both the fundamental TE mode and 2nd order TE mode. Shaded areas show the standard deviation values in duty cycle.	83
5.8	LIV characteristics of the (a) R3 FP device and (b) G1 DFB device.	85
5.9	(a) Emission spectra of the G1 DFB device and the R3 FP device at room temperature. (b) Emission spectra of the G1 DFB device shown on a log scale, with SMSR indicated.	87
5.10	Peak wavelength and SMSR as a function of current at a temperature of 25°C for the G1 DFB device.	88
5.11	LIV curves under pulsed current operation at varying temperatures for the (a) R3 FP device and (b) G1 DFB device.	89
5.12	(a) Threshold current, (b) threshold current density, (c) natural log of threshold current density and (d) slope efficiency as a function of temperature for the R3 FP and G1 DFB device.	91
5.13	Normalised emission spectra as a function of temperature for both the (a) R3 FP and (b) G1 DFB device. (c) Average wavelength as a function of temperature for both devices.	92
6.1	Layer diagrams showing the epitaxial structures containing the (a) quantum well active region and (b) quantum dot active region . .	98
6.2	High open area RWG LC-DFB structure fabricated in this work. .	99

6.3	Measured peak wavelength as a function of cavity length for broad area devices fabricated on the QD material used in this work. . .	101
6.4	(a) Deposition of SiO ₂ hard mask using e-beam evaporation. (b) Grating structure patterned in AZ2020 resist. (c) Grating structure etched into the hard mask. (d) Completion of the grating structure following etching into the epitaxial structure.	102
6.5	(a) 1 st order and (b) 3 rd order gratings patterned into undiluted AZ2020 resist. The dose used was 50 $\mu\text{C}/\text{cm}^2$	103
6.6	(a) 1 st , (b) 3 rd and (d) 11 th order gratings in diluted AZ2020 resist using a dose of 100 $\mu\text{C cm}^{-2}$. (c) Duty cycle as a function of dose for all grating orders.	104
6.7	SEM images of (a) 1 st order, (b) 3 rd order and (c) 11 th order devices following the etching of the epitaxial structure. (d) shows a 1 st order device following the BCB planarisation process.	106
6.8	Cross sections of (a) 1 st order, (b) 3 rd order and (c) 11 th order devices following the completion of the fabrication.	107
6.9	LIVT results for QW devices with varying grating orders. (a) and (b) show the LIV curves for channel-4 3 rd and 11 th order device respectively. (c) shows the threshold current density as a function of temperature for the 6 devices measured. (d) shows the slope efficiency, defined between threshold and 1 mW of power output, as a function of temperature for the 6 devices measured.	110
6.10	Emission spectra recorded at 20 °C and 180 mA for a (a) 3 rd order and (b) 11 th order channel-4 devices.	111
6.11	Peak wavelength as a function of current at varying temperature for the 11 th order (a) channel-3, (b) channel-4, (c) channel-5 and 3 rd order (d) channel-4, (e) channel-5 and (f) channel-6. Only the regions where single mode lasing was observed are shown.	112
6.12	SMSR heatmaps for the 11 th order (a) channel 3, (b) channel 4, (c) channel 5 and 3 rd order (d) channel 4, (e) channel 5 and (f) channel 6.	113

6.13	Emission spectra of a 3 rd order channel-5 device at a stage temperature of 35 °C and a driving current of (a) 80 mA, (b) 90 mA and 100 mA	115
6.14	(a) and (b) show the LIV curves for varying temperature for the channel 1 QW and QD devices respectively. (c) shows the threshold current density as a function of temperature for both materials under pulsed and CW operation. (d) shows the slope efficiency as a function of temperature for both devices on both materials.	117
6.15	Net modal gain spectra for the both materials at 250 K, calculated using the Cassidy method. The driving current for the QW device was 0.78 kA/cm ² and 1.42 kA/cm ² for the QD device.	119
6.16	Wavelength characteristics of 11 th order channel 1 devices on both the QW and QD material. Peak wavelength as a function of current for varying temperature is shown for the (a) QW device and (b) QD device. SMSR heatmaps are also shown for the (c) QW device and (d) QD device.	121
7.1	Schematics showing the (a) on-ridge and (b) off-ridge grating structures [123].	127
7.2	Schematic illustrating the scanning routines used in this work [123].	129
7.3	Gratings milled on-ridge with the SPL scanning routine and bismuth ions with a dose of (a) 158 nC/cm and 1 loop and (b) 264 nC/cm and 1000 loops. Gold ions with a dose of (c) 150 nC/cm and 1 loop and (d) 250 nC/cm and 1000 loops [123].	131
7.4	Cross-section of a grating milled on-ridge using gold ions and a dose of 400 nC/cm [123].	132
7.5	On ridge test structures milled with a single loop and (a) 50 nm designed gap size with a dose of 50 000 μC/cm ² . (b) 100 nm gap size with a dose of 30 000 μC/cm ²	133

7.6	(a) cross section of the off-ridge LC-DFB structure. (b) coupling coefficient as a function of grating offset for a grating with an etch depth of 1.5 μm , a grating depth of 100 nm, a ridge width of 2 μm and a grating length of 500 nm.	135
7.7	Off-ridge test structures milled using the SPL scanning routine and (a) A single loop with a dose of 150 nC cm and (b) 1000 loops with a dose of 264 nC cm [123].	136
7.8	Gap size as a function of number of loops using gold ions with a dose of 150 nC cm and an SPL scanning routine [123].	137
7.9	Off-ridge test grating structure milled with a dose of 52 800 $\mu\text{C}/\text{cm}^2$	138
7.10	Cross sections of off-ridge test structures. (a) SPL with dose of 120 nC cm. (b) longitudinal with a dose of 120 000 $\mu\text{C}/\text{cm}^2$. (c) concentric with a dose of 120 000 $\mu\text{C}/\text{cm}^2$ [123].	139
7.11	Milled depth as a function of dose for off-ridge test structures milled using longitudinal and concentric scanning routines.	140

Chapter 1

Introduction

Semiconductor laser diodes find applications across a vast range of sectors in the modern world. They have found uses in consumer applications such as CD players, laser pointers, printers and rangefinders, as well as large scale infrastructure projects such as optical communication networks. The laser diode has been particularly influential in the telecoms industry, as they are essential in fibre links, allowing information to be transmitted almost instantly across the world.

Due to the fact optical fibres exhibit low attenuation windows between the wavelengths 1260 - 1360 nm (O-band) and 1530 - 1565 nm (C-band), these wavelengths are used in optical communication networks. The C-band offers the lowest attenuation for modern fibres, therefore, it is generally used for long-range high bandwidth applications. Indium phosphide (InP) is the dominant material for emission in the C-band range. The reason for this is that whilst the band gap of InP is 1.34 eV, which corresponds to a wavelength of around 925 nm, it is an efficient substrate material for growing alloys that do correspond to C-band wavelengths. Specifically, the lattice constant of InP is 5.87 Å and is matched to $\text{In}_{0.53}\text{Ga}_{0.47}\text{As}$, which has a band gap of 0.748 eV corresponding to a wavelength of 1.65 nm. To achieve the desired emission wavelengths around 1550 nm, quaternaries of $\text{In}_x\text{Ga}_{1-x}\text{As}_y\text{P}_{1-y}$ can be used, where an x value corresponding to $0.47y$ provides a lattice match to InP [1]. The other common quaternary used in InP-based laser diodes is $\text{Al}_x\text{Ga}_y\text{In}_{1-x-y}\text{As}$, which has the benefit of a larger conduction band offset. This results in improved high temperature performance owing to the prevention of carrier leakage [2]. Quaternaries such as these are used

in the active regions of InP-based C-band laser diodes and as well as providing the substrate, InP provides the upper and lower cladding layers which form the waveguide and vertical confinement of light.

The large bandwidth required for long-range communications is typically achieved using wavelength division multiplexing. A diagram illustrating a typical set up for a wavelength division multiplexing (WDM) system is shown in Figure 1.1. The system consists of a series of transmitters which are designed to emit at specific wavelengths called channels. The transmitters are independently modulated to produce the bitstream, which enters a multiplexer. The purpose of the multiplexer is to combine the signals from all the transmitters and send them down a single mode fibre. Depending on the transmission distance, optical amplifiers may be included in the fibre. Finally, a demultiplexer at the other end separates the channels into their receivers [3]. In these systems, the bandwidth depends on the number of channels, therefore, reducing the wavelength spacing between the channels is essential for increasing bandwidth. Standard laser diodes would not be sufficient for these systems, as the many wavelengths produced by the Fabry-Perot laser cavity would travel along the optical fibre at different speeds. This phenomenon is known as dispersion and renders the transmitted signals unreadable over long distances [4]. As a result, the transmitters in WDM systems must be spectrally pure. This is achieved using single mode laser diodes, usually distributed Bragg reflector (DBR) or distributed feedback (DFB) lasers. In both examples, a Bragg grating is used to select the lasing wavelength, which depends on the pitch and refractive index of the grating. The only difference between the DBR laser and the DFB laser is that in the former there are one or two separate grating reflectors surrounding a gain section and in the latter the grating is distributed throughout the laser cavity. In WDM systems, the DFB is the most common as the fabrication is generally simpler and narrow linewidths can be achieved [1]. Using these emitters modern dense WDM (DWDM) systems can achieve bandwidths exceeding 17 Tb/s over distances longer than 10 000 km [5].

The transmitters used in WDM systems are typically buried grating DFB laser diodes. This means that the grating is contained within the epitaxial structure, necessitating an interruption of the growth process known as regrowth. This process is complex, increases cost and places stringent demands on wafer preparation

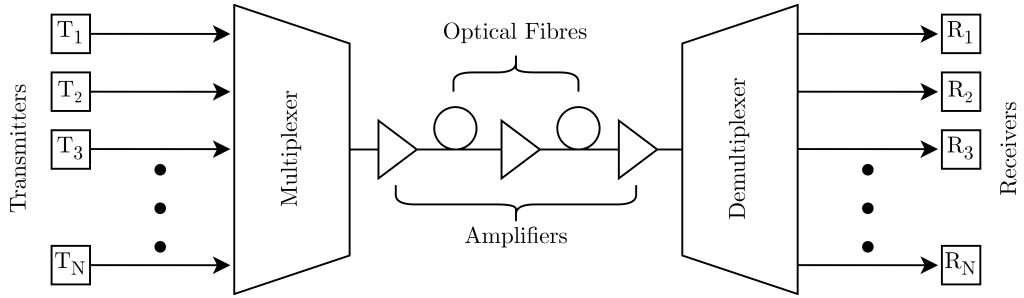


Figure 1.1: A conventional WDM link for optical communications.

and cleanliness. In some sectors therefore, the removal of the regrowth process would be beneficial. An example of this is photonic integrated circuits (PICs), specifically InP generic integration, which provides the ability to monolithically integrate all active and passive components completely [6, 7]. This technology has been successfully commercialised by companies such as Infinera, Lumentum and others. Despite the significant development that has gone into this technology, at the time of writing, the defect density of state-of-the-art InP PICs is as much as a factor of 10 higher than in the silicon integrated circuit industry [8]. One of the major reasons for this is the often-multiple regrowth steps required in the fabrication of complex InP PICs. Minimising the number of regrowth steps is, therefore, required to bring the defect levels of these devices down. For the DFB laser specifically, significant development has gone into regrowth-free device geometries. The most widely reported example of this is called the laterally-coupled DFB (LC-DFB) laser, which involves having the grating on the surface of the device coupled laterally to the optical mode. As well as reducing defects and fabrication complexity, the use of LC-DFB lasers as transmitters in InP PICs offers greater design flexibility and potentially a smaller footprint due to the fact that alignment is not required between the grating and ridge waveguide (RWG) structure. Despite significant development into these structures, commercialisation has been slow, partly due to the challenging nature of their fabrication. The aim of this thesis is to investigate novel device designs and fabrication methods in an attempt to simplify the fabrication of InP-based LC-DFB lasers targeting the C-band.

1.1 Chapter List

Chapter 2 Background

This chapter gives a brief account of the background theory for semiconductor laser diodes as well as DFB laser diodes.

Chapter 3 Design and Simulation of Laterally Coupled DFB Lasers.

The design parameters and modelling techniques used in this thesis are described.

Chapter 4 Methods: Fabrication and Characterisation.

The experimental techniques used in this thesis, including fabrication techniques and characterisation methods, are introduced.

Chapter 5 11th Order C-band DFB lasers Fabricated with Projection Lithography.

The design, fabrication and characterisation of 11th order gratings using projection lithography is presented. The results from an 11th order DFB laser are compared with a conventional Fabry-Perot ridge waveguide device.

Chapter 6 Grating Order Effects on LC-DFB Lasers using QD and QW Material.

The fabrication and performance of varying order LC-DFBs are compared in this chapter. Additionally, a comparison is made between high order LC-DFB lasers on both quantum well and quantum dot material.

Chapter 7 Direct Milling of LC-DFB Grating Structures Using Focused Bismuth and Gold Ions.

The fabrication of 1st LC-DFB grating structures using focused ion beam nanofabrication is presented. The suitability of this technique for on-ridge and off-ridge grating structures is compared.

Chapter 8 Conclusions and Future Work.

The thesis finishes with a discussion on the conclusions of this work followed by commentary on potential future work.

Chapter 2

Background

This chapter will give a brief overview of the theoretical background information of this work. This will begin with a discussion of general semiconductor laser diode theory, followed by a more specific discussion on distributed feedback lasers.

2.1 Basics of Semiconductor Laser Diode Operation

This section will describe the principles of operation of semiconductor lasers. The building blocks of a laser diode will be discussed, followed by the band structures that facilitate the emission of light. Additionally, the concept of optical gain will be introduced. The section will conclude by describing conventional laser diode structures, as these are essential in understanding the devices presented in this work.

2.1.1 Components

In general, there are three basic requirements for laser operation. Firstly, a source of energy is required, known as a pump source. Secondly, a cavity is needed to provide optical feedback and finally a gain medium is necessary to provide the photons that will be propagated in the cavity [1]. A typical Fabry-Perot (FP) semiconductor laser is shown in Figure 2.1. In this case the pump source is provided by an electrical current, while the cavity is generated by two cleaved

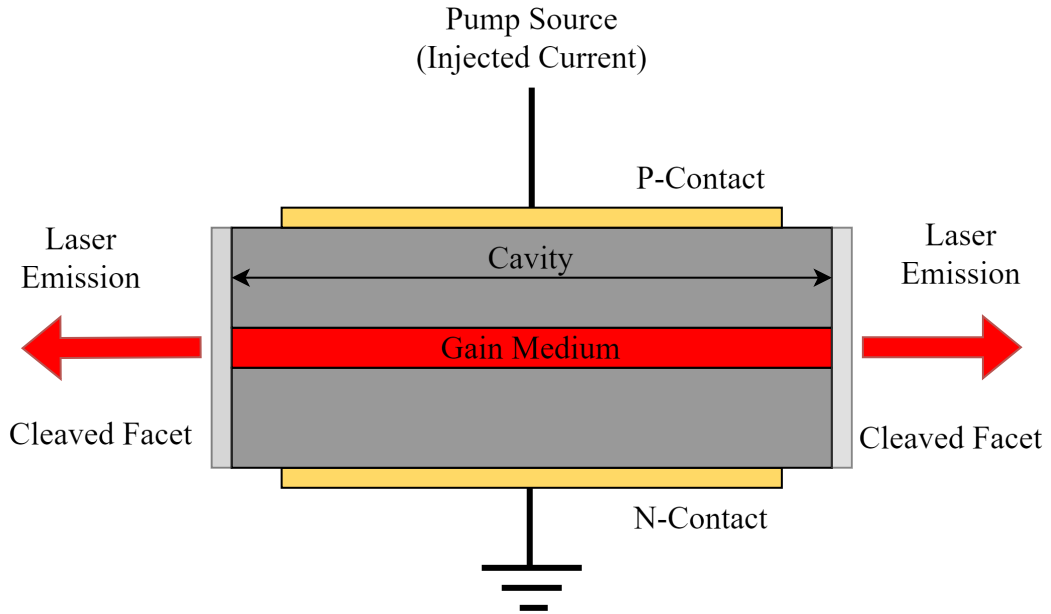


Figure 2.1: A simplified schematic showing basic principles of a standard Fabry-Perot laser.

facets at either end of the device. The reflection coefficient of these facets is approximately 0.31 so they provide the necessary reflections for optical feedback whilst still allowing some light out. Notably the use of two cleaved facets mean light is emitted at both ends so high reflection coatings are sometimes used to increase the light output of a single facet, which is more practical in reality. The requirement of the gain medium is to provide population inversion, where there are statistically more carriers in higher energy states than lower. From here stimulated emission can occur and light is emitted. Direct band gap semiconductors make excellent gain media as radiative recombination occurs readily in these materials. For laser diodes, the most basic structure to achieve recombination is called the pn junction. This is a structure where one side of the junction is p-doped and the other side is n-doped. The result of this is the migration of carriers from either side to the other close to the interface. The region around the interface, therefore, has no free carriers and is called the depletion region. Under forward bias, the potential barrier between the regions decreases and the width of the depletion region decreases, which allows carriers to begin flowing across the junction. Since carriers are flowing across the junction, electrons and holes can recombine with each other and emit photons [9]. Modern laser diodes

implement more advanced versions of the p-n junctions, such as the p-i-n junction. In this case an undoped region is included (intrinsic), which is designed to encourage recombination through the trapping of carriers. An example of this type of structure is called the separate confinement heterostructure (SCH), which will be described in section 2.1.5.

2.1.2 Band Structures and Transitions

The operation of a laser diode depends on the release of photons through the recombination of charge carriers (electrons and holes). The transitions that occur in semiconductors occur between the conduction and valence bands. Within these bands there is a continuum of energy states, intraband transitions among these states do not usually result in light emission but still influence the performance of laser diodes [10]. For light emission the interband transitions are of the most importance. Important transitions in semiconductor lasers are illustrated for a simplified two-level system in Figure 2.2. Through the addition of energy, which in the case of a laser diode involves the application of an electrical bias across the diode, some electrons will be elevated to the higher energy level. When they spontaneously decay and recombine with a hole (Figure 2.2a), a photon can be released. The energy of this photon is given by

$$\hbar\omega = E_2 - E_1, \quad (2.1)$$

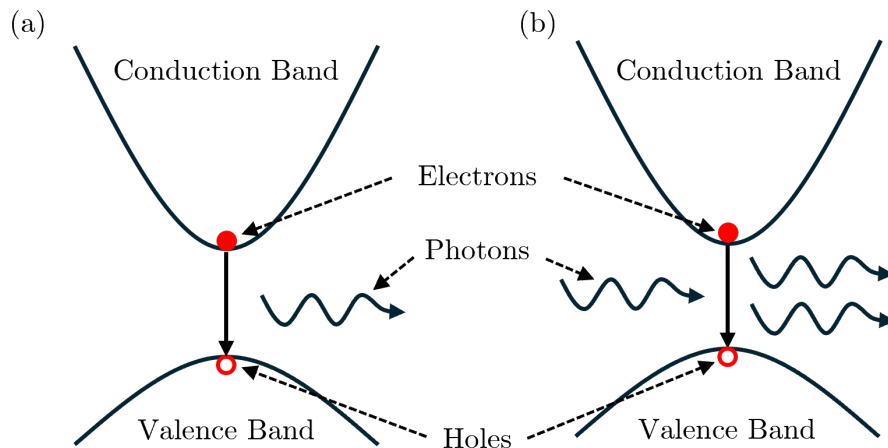


Figure 2.2: Simplified band structure showing (a) spontaneous emission and (b) stimulated emission.

where \hbar is Planck's constant divided by 2π and ω is the frequency. $E_2 - E_1$ is related to the band gap and it determines the wavelength of the emitted photons. In some cases, an electron in the higher energy level can recombine in response to incoming photons (Figure 2.2b). This is known as stimulated emission and is an essential process in lasers. In these transition processes, the energy and wavevector must be conserved. The conservation rule for the wavevector means that only direct band gap semiconductors can be used where light emission is required [10].

2.1.3 Optical Gain

As has been mentioned earlier, population inversion is required to achieve optical gain. This means that the probability of a higher energy state being occupied exceeds that of the lower energy states. If the probability of occupation of the lower state is f_1 and the probability of the higher state being occupied is f_2 , the probabilities can be written as

$$f_1 = \frac{N_1}{N}, f_2 = \frac{N_2}{N}, \quad (2.2)$$

where N is the total number of electrons, N_1 is the number of electrons on the lower energy state and N_2 is the number in the higher energy state. In a laser, stimulated emission results in electrons transitioning to the lower energy state, which in turn releases a photon. As such, the number of photons increases proportionally to the occupation probability of the higher energy state. The number of electrons which will allow an energy transition to the lower state is given by

$$Nf_2(1 - f_1), \quad (2.3)$$

where $1 - f_1$ is the probability of the lower energy state not containing any electrons. The rate of change of the number of photons, N_p also varies with the number of photons present in the system. Moreover, some photons can also be absorbed in the material if they induce the upward transitions. Including this along with the rate, C , the net rate that photons are added to the material is given by

$$\left[\frac{dN_p}{dt} \right] = CN(f_2 - f_1)N_p. \quad (2.4)$$

The key part of this equation is the section within the bracket. If f_2 is greater than f_1 the probability of an electron being in the higher energy state is higher than the probability of it being in the lower one, in which case optical gain has been achieved. We can define the optical gain coefficient, G , which is the increase in the energy of the light beam over the distance travelled. This is given by

$$G = \frac{1}{\Delta L} \frac{\Delta E}{E}, \quad (2.5)$$

where E is the product of the number of photons and the photon energy, $E = N_p h\nu$. We can incorporate equation 2.4 into equation 2.5 since the change in energy over distance is equal to the change in energy over time divided by the beam velocity. This leads to the following, using $\nu_{ph} = c/n$,

$$G = \frac{CN(f_2 - f_1)N_p h\nu}{\nu_{ph} N_p h\nu} = \frac{CN}{\nu_{ph}} (f_2 - f_1). \quad (2.6)$$

The probabilities of f_1 and f_2 can be described by the Fermi function, where the conduction band and valence band both have their own quasi-fermi levels which depend on the carrier population within them. The condition described by equation 2.4 can therefore be written as

$$\begin{aligned} E_{F2} - E_{F1} &> E_2 - E_1 \\ \Delta E_F &> h\nu. \end{aligned} \quad (2.7)$$

This is the gain condition and it specifies that for a given photon energy, in order to achieve gain the separation between the quasi-Fermi levels of the conduction and valence band must exceed that energy [11].

2.1.4 The Fabry-Perot Laser Cavity

The condition for population inversion in the gain medium has been described in the previous section. Population inversion on its own is not enough to achieve laser action, however, as feedback is required in the form of a resonator. As described earlier and shown in Figure 2.1, the feedback from an FP resonator is generated through the use of a cleaved facet at each end of the device. A resonator of this type only supports a discrete set of modes, which can be described as standing waves. The condition for resonance is given by

$$\sin(n_{eff}k_0L) = 0, \quad (2.8)$$

where L is the cavity length, n_{eff} is the effective refractive index and $k_0 = \omega/c$ is the wavenumber in vacuum. This condition gives rise to a series of equally spaced modes located at $n\pi$, known as longitudinal modes. Since the gain has a finite width, a number of these modes will lase in an FP device. The spacing of these modes is called the free spectral range (FSR) and is given by

$$\Delta\lambda = \frac{\lambda^2}{2n_gL} \quad (2.9)$$

where n_g is the group index and λ is the wavelength in vacuum. The gain condition within an FP cavity is given by

$$1 - \sqrt{R_1R_2} \exp(gt_hL) = 0, \quad (2.10)$$

where R_1 and R_2 are the reflectivities of the two mirrors and g is the gain coefficient, which when Rearranging equation 2.10, can be written as

$$gt_h = \frac{1}{L} \ln \frac{1}{\sqrt{R_1R_2}}. \quad (2.11)$$

The guided modes or lateral modes, which propagate along the waveguide, are not fully confined in the active region of the device. The light outside of these regions does not contribute to the gain, so must be considered as the internal loss. This provides

$$\Gamma g_{th} = \alpha_i + \frac{1}{2L} \ln \left(\frac{1}{R_1 R_2} \right) \quad (2.12)$$

where α_i is the internal loss and Γ is the confinement factor. The confinement factor represents the overlap of the optical mode with the active region and its product with g_{th} provides the modal gain, g_{modal} .

2.1.5 Typical Laser Structures

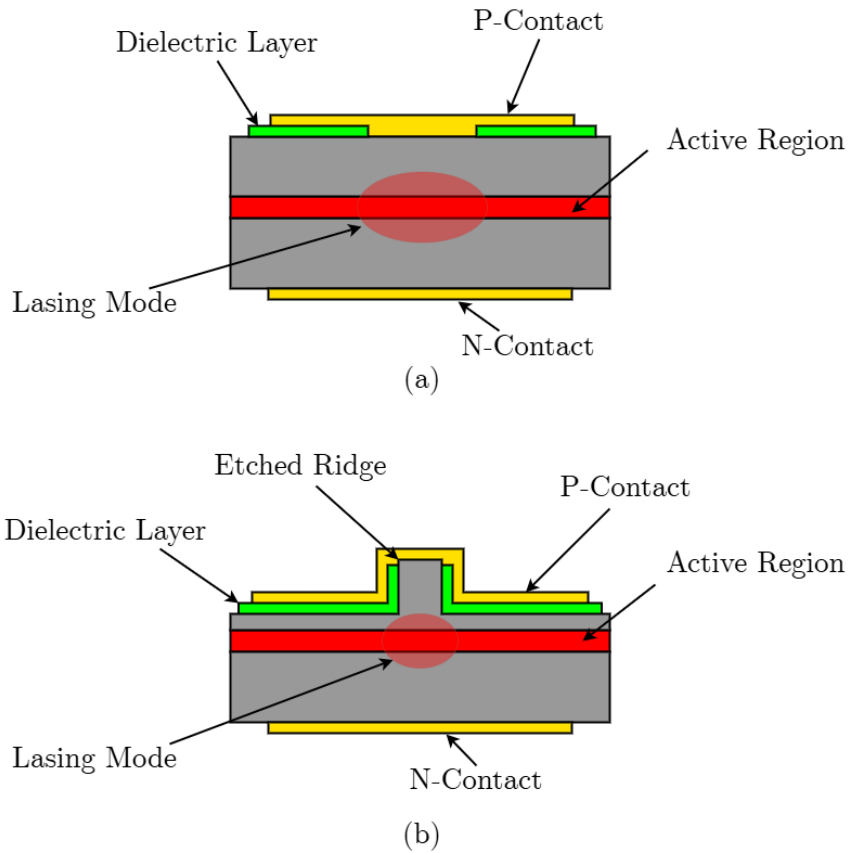


Figure 2.3: Simplified schematics showing; (a) An oxide stripe gain guided laser and (b) A ridge waveguide (RWG) laser.

The earliest laser diodes were based on pn junctions, which were described earlier in this chapter. The efficiency of these devices was limited as a result of poor optical and carrier confinement, however, which are necessary for reduced threshold current and improved efficiency [1]. In order to remedy this, the double heterostructure was introduced [12]. This design includes an active layer which is sandwiched between two higher bandgap layers known as cladding layers. The

double heterostructure provides improved efficiency over the pn junction due to the improved carrier confinement due to the potential well that is created by the active region. Additionally, higher band gap materials typically have a reduced refractive index. This means that the double heterostructure also provides a waveguiding effect, confining the light around the active region. This concept was expanded further by the introduction of the separate confinement heterostructure (SCH). In this structure, the active region, which is used for carrier confinement, is separated from the waveguide layers that facilitate optical confinement. The active region itself consists of multiple quantum wells with surrounding barriers and cladding. The result is a dramatic improvement in laser performance over double heterostructure lasers, specifically, reduced threshold current, improved power conversion efficiency and higher output powers [13, 14]. For this reason, the majority of modern laser diodes utilise the SCH. In terms of lateral confinement for the light and carriers, there are two main ways of doing this. The first of these is known as a stripe laser structure. In this case, the optical mode is defined by the location of the p-contact on top of the device which aims to cause lasing underneath the contact only, as a result this method is sometimes called gain guiding. The contact stripe can be defined on its own using photolithography or a dielectric layer can be used which has a window in it defining the stripe. An example of this is shown in Figure 2.3a. These structures are easy to fabricate and so are often used to assess the quality of an epitaxial growth. The lack of lateral optical confinement leads to increased loss compared to other structures and current spreading reduces electrical efficiency. As such, these devices are generally not used commercially [1]. More complex structures are required for reduced threshold current and efficiency. An example of such a structure is called the ridge waveguide (RWG) laser. In this example, which is shown in Figure 2.3b, a narrow ridge is etched to either just above or through the active region. In the space left after the etch, dielectric is deposited which results in variation of the refractive index, resulting in strong confinement of the light underneath the ridge as well as electrical confinement of carriers laterally as they can only pass through the ridge [15]. Since current spreading is also reduced in this structure, the threshold current and efficiencies of these devices are improved significantly over the stripe laser [11]. The final type of laser structure which will be described here is the buried heterostructure (BH) laser diode. In this design, a stripe is defined and etched as in the case of the RWG laser. For a BH laser, however, the

etch continues through the active region. From there, low refractive index, high bandgap material is grown to encase the active region [16].

2.2 The Distributed Feedback Laser

Now that an overview of basic laser theory and background has been provided, more complex laser structures such as the ones fabricated in this work can be discussed. This section will cover the principles behind distributed feedback (DFB) laser operation including commonly used grating structures and methods for achieving single mode emission.

2.2.1 Theoretical Basis - Coupled Mode Theory

As previously mentioned, the addition of grating structures in lasers is often done to act as a filter for desired wavelengths of light. This works due to the modulation of the refractive index or gain/loss, which causes certain wavelengths of light to be reflected preferentially. There are two main ways of implementing a grating in a laser structure, these are known as distributed Bragg reflector (DBR) and the DFB laser. Simplified diagrams of these two structures are shown in Figure 2.4. Here it can be seen that the DBR laser describes a cavity with gratings at one or both ends of the laser cavity, acting as mirrors, whereas the DFB laser includes a grating throughout the cavity. The operating principle in both devices is similar, and as such, so is the theory. The operating principles of DFB lasers are described

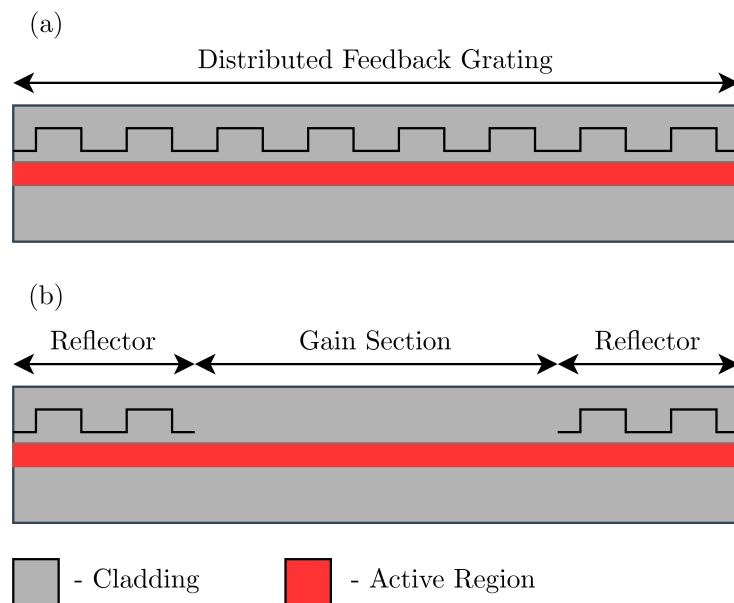


Figure 2.4: (a) DFB device structure and (b) DBR device structure.

by coupled mode theory, which was introduced by Kogelnik and Shank in 1972 [17], following their presentation of the first ever DFB laser a year earlier [18]. This theory describes the DFB laser in terms of two counter propagating waves in the z direction of the cavity. Each wave receives light from the other at each section in the grating. The modulation of both the refractive index and the gain can be considered in the following way

$$\begin{aligned} n(z) &= n + n_1 \cos(2\beta_0 z) \\ \alpha(z) &= \alpha + \alpha_1 \cos(2\beta_0 z), \end{aligned} \tag{2.13}$$

where n and α are the average of the refractive index and gain constant in the cavity respectively and n_1 , α_1 are the amplitudes of the modulation. Since $\beta_0 = n\omega/c$ at the Bragg condition, and assuming that the variation in the gain and refractive index are small, the k constant of Maxwell's wave equation can be written as

$$k^2 = \beta^2 + 2j\alpha\beta + 4\kappa\beta\cos(2\beta_0 z). \tag{2.14}$$

This leads to the coupling coefficient κ , which is described by

$$\kappa = \frac{\pi n_1}{\lambda_0} + \frac{1}{2}j\alpha_1. \tag{2.15}$$

This is an extremely important parameter for simulating DFB lasers, as it provides a measure of the how strong the backwards scattering in each of the counter-propagating waves is and thus, describes the degree of feedback provided by the grating. Considering the Maxwell equation for electric field, in the form

$$\frac{d^2 E}{dz^2} + k(z)^2 E = 0, \tag{2.16}$$

we can substitute equation 2.14 into it, which yields a second order differential equation. When solved, this provides the solution

$$\begin{aligned}
E(z) &= E_r(z) + E_s(z) \\
E_r(z) &= R(z)\exp(-i\beta_0 z) \\
E_s(z) &= S(z)\exp(i\beta_0 z).
\end{aligned} \tag{2.17}$$

Using equation 2.16, the wave equations for R and S , which are often referred to as the coupled wave equations, can be extracted.

$$\begin{aligned}
-\frac{dR}{dz} + (\alpha_0 - i\delta)R &= i\kappa S \exp(-i\Omega) \\
\frac{dS}{dz} + (\alpha_0 - i\delta)S &= i\kappa R \exp(i\Omega)
\end{aligned} \tag{2.18}$$

Where δ is called the detuning and is defined through the expression

$$\delta = \frac{\beta^2 - \beta_0}{2\beta_0} \approx \beta - \beta_0. \tag{2.19}$$

This is related to the wavelength and a detuning value of zero corresponds to the Bragg wavelength, which is given by

$$\lambda_B = \frac{2n_{eff}\Lambda}{m}, \tag{2.20}$$

which is another key equation in the design of DFB lasers. It states that the Bragg wavelength of the laser is dependent on the pitch of the grating, Λ , the effective index of the optical mode, n_{eff} and the grating order, m . A transfer matrix can be applied to the problem as follows [19, 20],

$$\begin{bmatrix} E_r(0) \\ E_s(0) \end{bmatrix} = \mathbf{F} \begin{bmatrix} E_r(L) \\ E_s(L) \end{bmatrix} \tag{2.21}$$

where L is the length of the grating and the transfer matrix, \mathbf{F} is given below.

$$\mathbf{F} = \begin{bmatrix} F_{11} & F_{12} \\ F_{21} & F_{22} \end{bmatrix} \quad (2.22)$$

The individual components of this matrix are given by,

$$\begin{aligned} F_{11} &= \left[\cosh(\gamma L) - \frac{\alpha_0 - i\delta}{\gamma} \sinh(\gamma L) \right] \exp(i\beta_0 L), \\ F_{12} &= \frac{i\kappa}{\gamma} \sinh(\gamma L \exp[-i\beta_0 L + \Omega]), \\ F_{21} &= -\frac{i\kappa}{\gamma} \sinh(\gamma L \exp[-i\beta_0 L + \Omega]), \\ F_{22} &= \left[\cosh(\gamma L) + \frac{\alpha_0 - i\delta}{\gamma} \sinh(\gamma L) \right] \exp(i\beta_0 L), \end{aligned} \quad (2.23)$$

where a new term has been introduced, γ , which is defined by the following.

$$\gamma^2 = (\alpha_0 - i\delta)^2 + \kappa^2 \quad (2.24)$$

The power transmissivity and reflectivity can be derived from the matrix elements and are given by the equations below [20].

$$\begin{aligned} T &= \frac{1}{|F_{11}|^2} \\ R &= \frac{|F_{21}|^2}{|F_{11}|^2} \end{aligned} \quad (2.25)$$

Using this transfer matrix formalism, the behaviour of a number of grating structures can be described.

2.2.2 Uniform Gratings

The most basic type of DFB laser grating is the uniform grating. This describes a grating that does not change throughout the length of the cavity. For a uniform

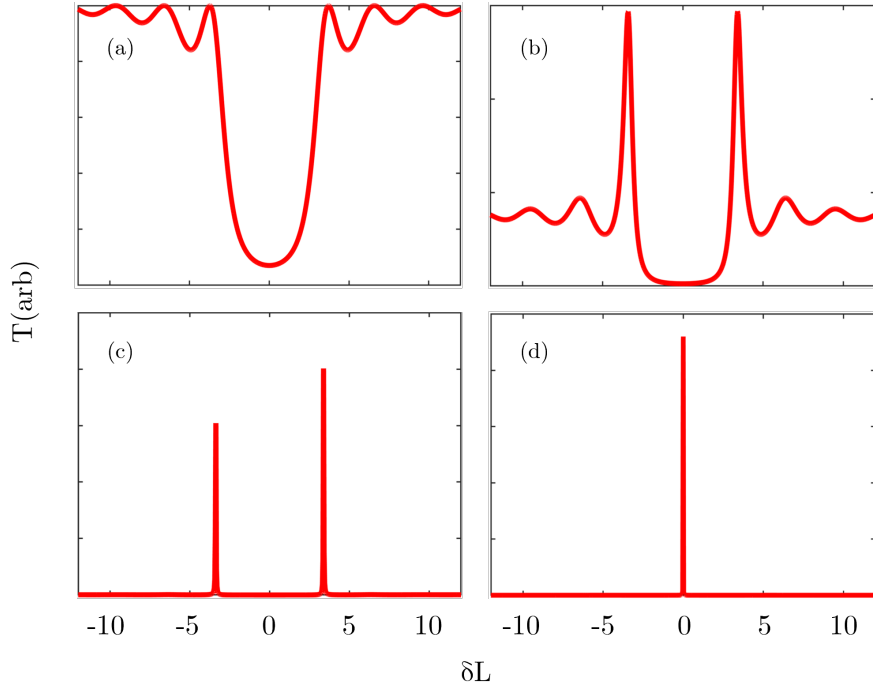


Figure 2.5: Transmission spectra of DFB laser gratings. (a) $\alpha_0 L = 0$, (b) $\alpha_0 L = 0.66$, (c) $\alpha_0 L = 1$ and (d) Quarter wave phase shifted grating with $\alpha_0 L = 1$.

grating with a coupling coefficient multiplied by the cavity length, $\kappa L = 2$ and zero gain present in the cavity i.e. $\alpha_0 = 0$, the transmission spectrum can be calculated by 2.25. The result of this is shown in Figure 2.5a. Here, the characteristic stopband of the Bragg grating is observed. When gain is added to the cavity, the transmission spectra change slightly. Figure 2.5b and 2.5c show the transmission spectra when the gain value is $\alpha_0 L = 0.66$ and $\alpha_0 L = 1$, respectively. It can be seen that two lasing modes emerge either side of the Bragg wavelength, when gain is applied. For applications that require single mode behaviour, this is not ideal and significant work has gone into developing techniques to remove this behaviour.

2.2.3 Strategies for Achieving Single Mode Lasing

The description of a uniform grating shown above assumes that the facets are located exactly on a grating interface. In reality, this is not likely to be the case, as a device cleave cannot be made with such high precision. Therefore, unless the device is coated with anti-reflective (AR) coatings, the facet-grating phase

relationship will determine whether the device is single mode. Using facets as-cleaved will result in some single mode devices, however, this is not suitable for wafer scale fabrication, as the yield is dependent on the distribution of facet phase across all devices [21, 22]. The application of a highly reflective (HR) coating on one facet and an AR coating on the other is commonly used to remedy this issue as then only the HR facet phase contributes to the single mode yield [23]. This leads to the possibility of deliberately adding a phaseshift to the grating to guarantee single mode emission. Such a phase shift can be described by splitting the cavity into two sections where the phase at the interface between the two sections is related to the phase at the start of the cavity through the equation

$$\theta_2 = \theta_1 + 2\beta_0 L_1. \quad (2.26)$$

Since the phase shift is located between the two sections, the phase at the beginning of the second cavity can be written as

$$\theta_3 = \theta_2 + \Delta\Omega = \theta_1 + 2\beta_0 L_1 + \Delta\Omega. \quad (2.27)$$

Incorporating a phase shift in the cavity equal to π , results in a single transmission peak centered on the Bragg wavelength (Figure 2.5d). This phase shift corresponds physically to a grating offset in the second half of the cavity by half the pitch, $\Lambda/2$. Substituting this into equation 3.1 gives the following [20]

$$\frac{\Lambda}{2} = \frac{\lambda_B}{4n_{r0}} = \frac{\lambda}{4}. \quad (2.28)$$

This means that in order to achieve a phase shift equal to π a shift in the grating that equals one quarter of the Bragg wavelength needs to be added. Typically, a grating with a phaseshift is combined with AR coatings on both facets to remove the FP resonator longitudinal modes. This results in very high single mode yield and wavelength control compared to the HR/AR facet coating scheme [24], however, devices with quarter wavelength phaseshifts often suffer from high spatial hole burning (SHB) due to the photon energy being high at the phaseshift [25]. As a result, DFB lasers using the HR/AR facet coating scheme generally exhibit

reduced threshold currents and higher efficiency, with the cost of reduced wavelength control [23]. Work has been done to limit the SHB in devices incorporating phaseshifts. For example the application of two $1/8$ wavelength phaseshifts has been shown to limit the effect [26].

2.2.4 Buried Grating DFB Lasers

Commercially, the most successful type of DFB laser is the buried grating DFB laser. In this type of device, the grating is located close to the active region within the epitaxial structure, as shown in Figure 2.6. This is typically achieved by growing the lower epitaxial layers, usually including the active region, then defining and etching the grating structure into a high index layer [27]. From here, the upper layers are grown on top of this structure. Interrupting the epitaxial growth in this way is known as regrowth or overgrowth. Placing the grating within the structure, offers the highest coupling efficiency possible as the overlap between the grating and the optical mode is maximised. As such, the depth of the grating usually only needs to be tens of nanometres deep. From a fabrication perspective, the regrowth process places stringent demands on surface cleanliness and can introduce defects into the epitaxial structure. In wafer-scale manufacturing, these issues have been overcome to some extent, although the complexity of the regrowth process is heavily associated with the high cost of DFB laser modules.

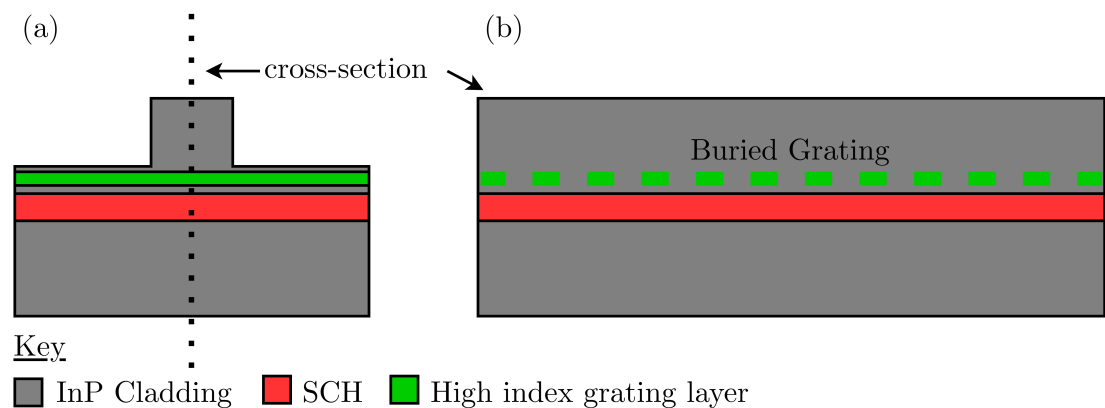


Figure 2.6: A (a) facet view and (b) side view of a RWG buried grating DFB laser.

2.2.5 Laterally-Coupled DFB Lasers

Owing to the complex nature of buried grating DFB laser fabrication, considerable effort has gone into simplifying it. The typical method is to use a laterally-coupled DFB (LC-DFB) grating structure. The fabrication of a LC-DFB laser is performed by growing all the epitaxial layers, then defining and etching the grating and sometimes the RWG onto the top of the structure.

The first demonstration of a LC-DFB laser was published in 1991 by researchers from the University of Illinois, utilising a similar structure to that shown in Figure 2.7a [28]. Whilst this work demonstrated the working principle of the LC-DFB laser, its performance was relatively poor. Specifically, it had a low side mode suppression (SMSR) value, which is a key metric of performance in DFB lasers as it defines the ratio between the lasing peak and the second highest peak and, therefore, the spectral purity. Later in 1994, R. D. Martin and colleagues further demonstrated the potential of these devices, showing a LC-DFB laser based on InGaAs-GaAs-AlGaAs [29]. This device exhibited a threshold current of 11 mA with a SMSR value of 30 dB. Then in 2000, Chen et al presented a LC-DFB on InGaAsP/InP which exhibited a threshold current of 17 mA and an SMSR value of 45 dB [30]. In this example, the grating was integrated onto the RWG, which is still most commonly used LC-DFB structure. An illustration of this type of structure is shown in Figure 2.7b. The benefit of this over the structure shown in Figure 2.7a is that the etching of corrugated sidewalls is simpler than etching deep trenches and the structure benefits from the index guiding properties of the RWG.

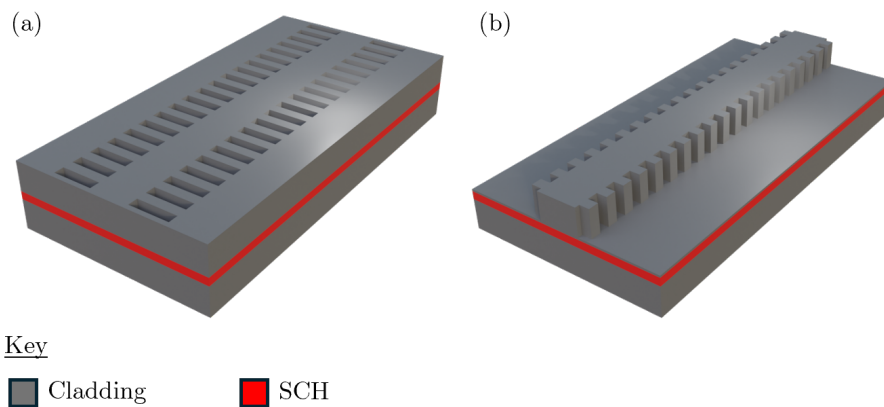


Figure 2.7: (a) Early LC-DFB laser presented in [28]. (b) Typical LC-DFB RWG laser structure.

In the early examples of LC-DFBs lasers described above, the gratings used were index coupled, however, complex coupled gratings can also be fabricated. In 1999 researchers from the University of Würzburg presented a complex coupled LC-DFB laser using periodic strips of chromium deposited either side of the RWG using a lift-off process. The complex nature of the metals refractive index results in a modulation of the gain. Using this method a threshold current of 9 mA was achieved with an SMSR value exceeding 45 dB [31]. The yield of these structures is high due to the asymmetric threshold gain value of the two modes either side of the grating stopband. As a result, this structure has since been commercialised by Nanoplus nanosystems and a wide range of wavelengths can be accessed on many different material systems using this technique [32]. The main disadvantage of using the metallic gratings, however, is the increased loss in the structure due to proximity of the metal to the optical mode.

In the examples discussed so far, electron beam lithography was utilised as the patterning method for the gratings. This patterning method is time consuming and expensive, so efforts have been made to implement higher throughput techniques. An example of this includes holographic or interference lithography, which uses the interference pattern of two laser to pattern the periodic grating structure. Researchers from Tsinghua University presented an LC-DFB laser on AlInGaAs/InP using this technique. The device exhibited a threshold current of 34 mA and a SMSR value of 45 dB emitting in the C-band [33]. More recent work has also utilised this patterning technique to achieve high performance LC-DFB lasers [34]. The disadvantage of this technique is that design flexibility is reduced as only periodic structures (without phaseshifts) can be patterned. Nanoimprint lithography is another example of a high-throughput technique which can be used to pattern LC-DFB lasers. Work performed at the Technical University of Tampere demonstrated a 3rd order LC-DFB laser on GaAs based material, which exhibited an SMSR value of 50 dB [35]. Stepper lithography has also been used in the patterning of 3rd order gratings. An example is work by Dridi et al, which demonstrated a device on InGaAsP/InP with a SMSR value of 50 dB [36].

Some of the examples above utilise higher order gratings to achieve DFB laser operation. The use of these designs simplifies the fabrication complexity due to their larger feature sizes. Moreover, higher order gratings have also attracted interest due to their ability to provide high SMSR values without the need for

phase shifts [37, 38]. Typically, 3rd order gratings are used, however higher order gratings have been implemented previously. For example, work by Fricke et al presented DBR lasers with 6th and 7th order gratings on GaAs material, achieving SMSR values of over 30 dB. In this case I-line lithography was used to pattern the gratings [39]. Another example of a high order grating is work performed by Slight and colleagues on the GaN material system. In this work, LC-DFB lasers with 39th order gratings were demonstrated with SMSR values of over 35 dB [40].

Implementation of higher order gratings particularly on the InP material system has been limited and experimental comparisons between grating orders have not been reported. The work described in this thesis attempts to address this. Alongside this, a new fabrication methodology for LC-DFB gratings using direct milling with a focused ion beam is presented for cases where a 1st order grating is required such as short cavity length devices.

2.3 Summary

This chapter has introduced the basic theory underpinning the work presented in this thesis. A brief introduction in the theory of laser diodes was provided. This section presented the three components that form the laser, the pump source, the gain medium and the resonant cavity. The idea of population inversion was discussed and its importance in achieving optical gain. Furthermore the threshold gain condition was described. Common laser diode structures were described, namely, the oxide isolated stripe laser, the RWG laser and the BH laser. Specifically, the various ways in which these devices confine both light and carriers to improve performance.

Specific theory detailing the DFB laser was also provided. An overview of coupled mode theory was presented, along with the introduction of the coupling coefficient. Moreover, a transfer matrix was applied to the DFB laser structure, which allowed the examination of behaviour in various DFB grating structures. Specifically, it was shown that a uniform grating results in the propagation of two degenerate modes either side of the Bragg wavelength. Methods for removing this degeneracy were presented, including facet coating schemes and the introduction of a phase shift. Finally, two types of DFB laser were described; the buried grating DFB laser and the LC-DFB laser, which is the subject of this thesis.

Chapter 3

Design and Simulation of Laterally Coupled DFB Lasers

3.1 Overview

This chapter will describe the design and modelling process used in this work. The variable dimensions and parameters involved will be described, followed by an overview of traditional simulation techniques and adaptations made when considering LC-DFB lasers. The chapter will conclude by describing the effect of changing dimensions on the coupling coefficient.

3.2 Fundamental Structure and Parameters

The first step in a DFB laser design process is usually to ascertain the desired lasing wavelength of the finished device. Primarily, the devices fabricated in this work were targeted in the c- and l-band of the electromagnetic spectrum, which correspond to a wavelength range of 1530-1565 nm and 1565-1625 nm respectively. The Bragg wavelength, λ_B , of a DFB grating is provided by the equation

$$\lambda_B = \frac{2n_{eff}\Lambda}{m}, \quad (3.1)$$

where n_{eff} is the effective index of the optical mode, Λ represents the pitch of the grating and m is the grating order. Figure 3.1 shows the required grating pitch

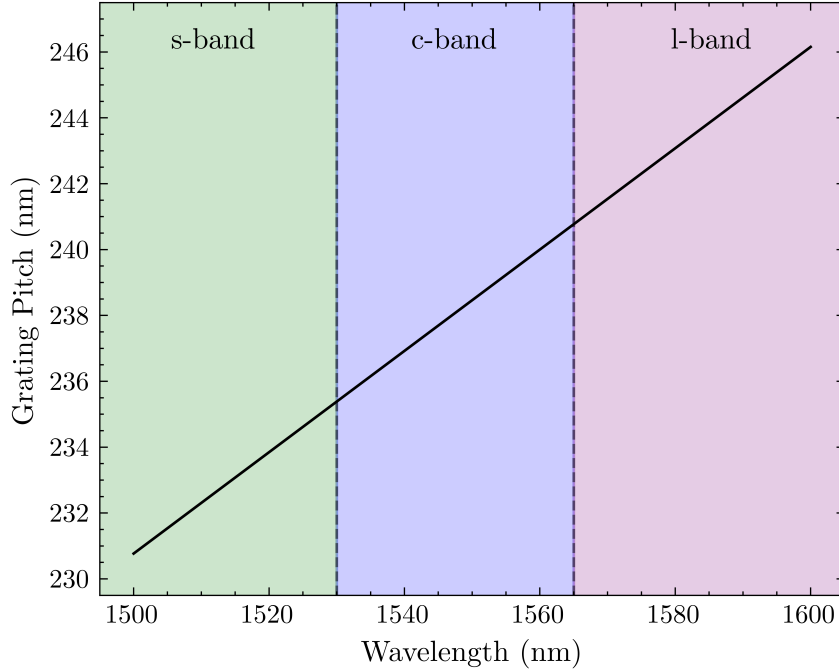


Figure 3.1: Required grating pitch targeting wavelengths between 1500 and 1600 nm. In this case the effective refractive index is assumed to be 3.25.

for emission wavelength between 1500 and 1600 nm using an effective refractive index of 3.25. In order to target the c-band the grating pitch must be between approximately 235 and 241 nm and for 1550 nm specifically, the grating pitch must be 238 nm. For increased grating order, these numbers are simply multiplied by the grating order. Therefore, to target 1550 nm using a 3rd order grating, a pitch of 712 nm is required. In addition to pitch selection, there are a number of parameters that can influence the coupling coefficient of the grating. Related to the grating pitch is a parameter known as the duty cycle. This parameter describes the ratio between the grating teeth length, L_{teeth} and the pitch. This can be written as

$$\gamma = \frac{L_{teeth}}{\Lambda}, \quad (3.2)$$

which means that to achieve a duty cycle of 0.5 for a grating pitch of 240 nm, the gap between grating teeth would need to be 120 nm. This parameter is particularly important for higher order gratings, as will be shown in section 3.5.5. Furthermore, the duty cycle also dictates the minimum feature size, which is

relevant when considering which patterning methods are appropriate during fabrication. Additional parameters are shown in Figure 3.2, which shows an example cross-section of the LC-DFB structure along with the plan view of the structure. The ridge width, W_R refers to the width of the narrowest portion of the ridge structure, excluding the gratings which extend by length L_E which is referred to in this work as the extrusion length. The whole structure is etched to a depth of d . In the example shown in Figure 3.2, the whole structure is encapsulated in benzocyclobutene (BCB) 3022-46 which provides the refractive index contrast for the grating, which is set in the upper InP cladding of the epitaxial stack. The selection of BCB as the dielectric for this structure has multiple benefits. Firstly, BCB can be used to encapsulate the grating structure entirely, eliminating air gaps and keeping the contact metals away from the structure, which would increase the design complexity. Secondly, BCB is effective at passivating exposed semiconductor surfaces, which is essential for reducing non-radiative surface recombination in laser diodes [41, 42]. Additionally, BCB has a low dielectric constant of around 2.65, making it more attractive for devices that are to be modulated at high frequency due to reduced parasitic capacitance. The application of BCB is also relatively simple as it can be spin coated. Other dielectrics such as SiO_2 or SiN are often deposited using complex techniques such as plasma enhanced chemical vapour deposition (PECVD) or atomic layer deposition (ALD), which are more expensive and time consuming compared to spin coating. Finally, BCB also has very high thermal stability compared to other spin-on polymers such as SU-8. This means that it remains unchanged during subsequent high temperature processing steps such as contact annealing. For the designs in this work, the BCB was assumed to have a refractive index of 1.535 [43], however, a variation of up to 3% has been observed in previous studies by other members of the optoelectronics group at Cardiff University.

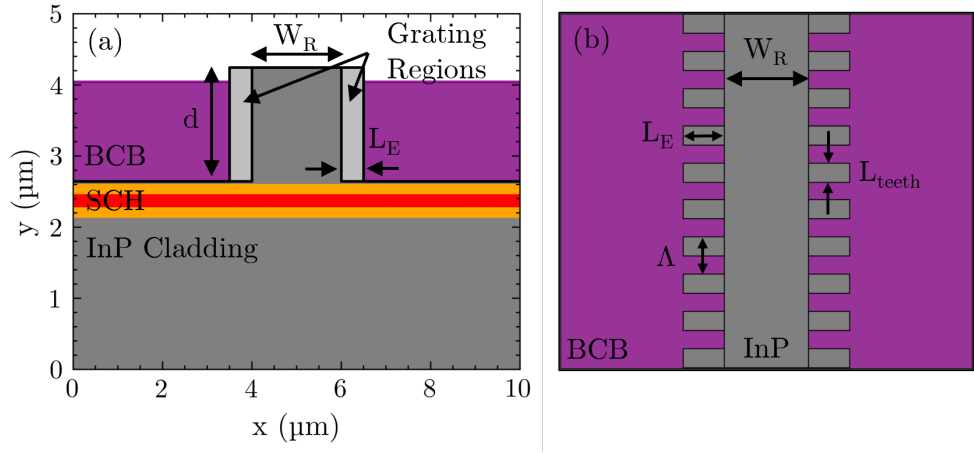


Figure 3.2: (a) Cross-section of an example LC-DFB laser with grating regions shown in light grey. (b) Plan view of an example LC-DFB grating structure.

3.3 Traditional DFB Simulation Techniques

Traditional modelling for buried grating DFB structures is based on the modified coupled mode equations presented by Streifer, Scifres and Burnham in 1975 [44]. In this work they presented a general expression for the coupling coefficient given by

$$\kappa = \frac{k_0^2}{2\beta_0 P} \int_0^g A_p \varepsilon_0^2 dx, \quad (3.3)$$

where P is the power contained in the optical mode, β_0 is the propagation constant within the grating region and A is given by

$$A = -\frac{(n_2^2 - n_1^2)}{\pi m} \sin(\pi m \gamma), \quad (3.4)$$

where n_1 is the lower refractive index and n_2 is the higher refractive index. In this case only one dimension is considered, which is only valid when the grating is spread sufficiently large under the lasing stripe that it covers the entire optical mode. For a more accurate model, the proximity of the grating to the optical mode in both the lateral and vertical direction needs to be considered as the grating may not be continuous underneath the ridge. Applying this we can write an expression in two dimensions, inserting equation 3.4 into equation 3.3.

$$\kappa = \frac{k_0}{2n_{eff}}(n_2^2 - n_1^2) \frac{\int \int_{Grating} \psi^2(x, y) dx dy}{\int_{-\infty}^{\infty} \int_{-\infty}^{\infty} \psi^2(x, y) dx dy} \frac{\sin(\pi m \gamma)}{\pi m} \quad (3.5)$$

The fractional component of equation 3.5 containing the integrals describes the extent to which the optical mode overlaps with the grating region in two dimensions. This value is called the confinement factor, Γ_g and allows this traditional kappa calculation to be presented in a simpler way as shown below, assuming that $n_1 + n_2 = 2n_{eff}$.

$$\kappa = k_0(n_2 - n_1)\Gamma_g \frac{\sin(\pi m \gamma)}{\pi m} \quad (3.6)$$

This expression for the coupling coefficient is accurate, with the assumption that the refractive index contrast is relatively low. In a buried grating InP device, the grating is typically made up of a high refractive index layer with refractive index of between 3.5 and 4, grown on top of the InP cladding with a refractive index of 3.16. This is not the case for a laterally coupled DFB laser where the dielectric which is deposited on top of the structure forms the lower refractive index part of the grating. This means that the refractive index modulation can be much larger since the refractive index of BCB for example is around 1.5 at 1550 nm. Adaptations need to be made, therefore, when modelling LC-DFB lasers.

3.4 Effective Index Alteration Technique

As previously mentioned, the traditional method for calculating the coupling coefficient is not suitable for LC-DFB laser gratings. The main reason for this is the large refractive index contrast present in a LC-DFB. Laakso and colleagues presented a method for calculating the coupling coefficient in LC-DFB lasers specifically, in 2008 [38]. This was chosen as the method for all coupling coefficient calculations performed in this work. The reason is that it provides the ability to calculate the coupling coefficient for higher order gratings as well as 1st order structures. It was also chosen for its simplicity compared to other techniques where radiation mode calculations are required [45]. Additionally, these methods consider gain coupling also which is not required for the devices fabricated in this work as the intention was to avoid any modulation of the loss or gain. The

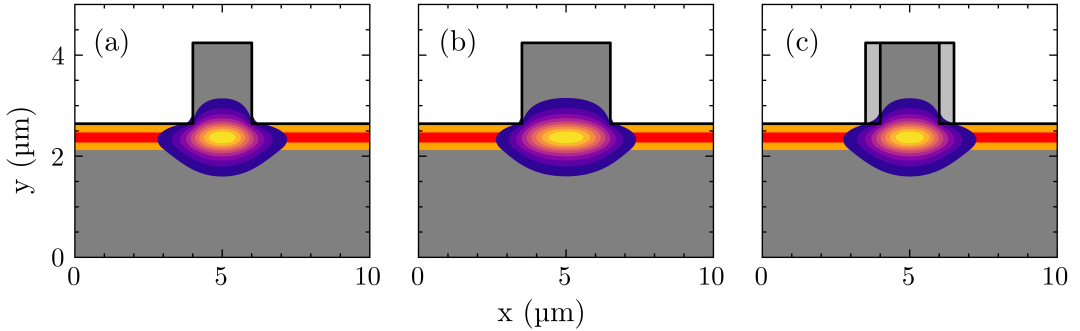


Figure 3.3: Normalised fundamental TE modes overlaid on the ridge waveguide cross sections that make up the LC-DFB laser structure. (a) narrow, (b) wide and (c) averaged.

method presented in [38] is based on the introduction of slices that make up the grating structure. These are two dimensional cross-sections of each section of the grating, referred to as narrow and wide. The narrow section defines the section within a grating gap and the wide section defines the section where a tooth or extrusion is located. Equation 3.5 can be adapted in the following way

$$\kappa = \frac{k_0}{2n_{eff}} \cdot (n_{eff,2}^2 - n_{eff,1}^2) \cdot \frac{\sin(\pi m \gamma)}{\pi m}, \quad (3.7)$$

where effective indices, $n_{eff,1}$ and $n_{eff,2}$ have been inserted in place of the confinement factor, Γ_g and the two refractive indices. Equation 3.7 assumes that the optical mode changes instantaneously between each section of the grating. In a first order grating, however, the length of a given section is on the order of $\lambda/4$, so this is not realistic. Therefore, the addition of an averaged waveguide was proposed, where the refractive index within the grating section is a weighted average of the two refractive indices that make up the grating. This effectively provides an equivalent waveguide in two-dimensions that is analogous to the whole grating structure. Figure 3.3 illustrates the narrow, wide and averaged waveguides with their calculated optical modes. The refractive index of the grating sections in Figure 3.3c are given by

$$n_{avg}^2(x, y) = \gamma \cdot n_{wide}^2(x, y) + (1 - \gamma) \cdot n_{narrow}^2(x, y), \quad (3.8)$$

where γ is the duty cycle. The refractive index is weighted by the duty cycle,

which means that if the duty cycle is equal to one, the average refractive index of the grating region is equal to the refractive index of InP. Similarly, if the duty cycle is equal to zero the average refractive index is equal to the refractive index of BCB. The effective indices can then be recalculated for both slices of the grating (narrow and wide). This is done using an overlap of the averaged waveguide's fundamental transverse electric (TE) mode, TE_{00} , intensity, $\psi^2(x, y)$ with the refractive index distribution, $n_i(x, y)$ of each slice.

$$n_{eff,i} = \sqrt{\frac{\int \psi^2(x, y) \cdot n_i^2(x, y) \cdot dx dy}{\int \psi^2(x, y) \cdot dx dy}} \quad (3.9)$$

These new effective index values can then be inserted into equation 3.7 to allow the calculation of more accurate coupling coefficient values.

3.5 Simulation Results from LC-DFB Lasers

This section describes the simulation results based on the QW epitaxial structure used in this work. The initial mode calculation process will be described, followed by detailed examination of each variable in the design process detailed in Figure 3.2.

3.5.1 Optical Mode Calculation

In order for the modelling techniques described above to be used, the optical modes present in the waveguides must first be calculated i.e. to calculate the effective index of the mode. For this task, the finite difference mode (FDM) solver in Photon Design's FIMMWave software was used. This was chosen for its ability to effectively calculate modes in waveguides with large refractive index steps, such as the case here [46]. The three waveguides that make up the LC-DFB structure were defined as a series of layers with a given refractive index corresponding to the 9QW epitaxial structure used in this work. The epitaxial structure, which was grown by the Compound Semiconductor Centre Ltd, is shown in Figure 3.4. The substrate was n-type InP, upon which, a 1500 nm n-type InP lower cladding was grown. This was followed by the SCH, which consisted of 9 InAlGaAs QWs

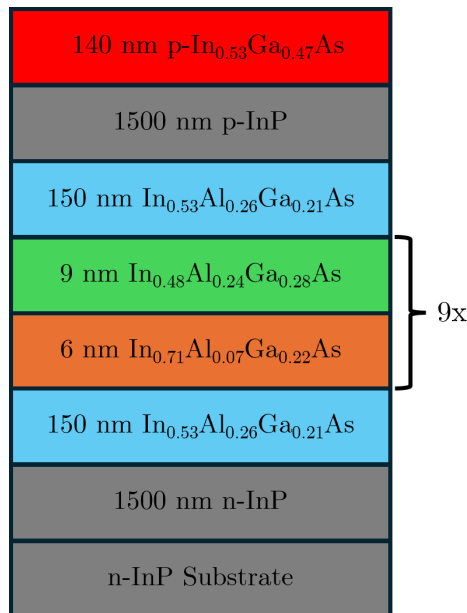


Figure 3.4: The QW epitaxial structure used in this simulation chapter and throughout this work.

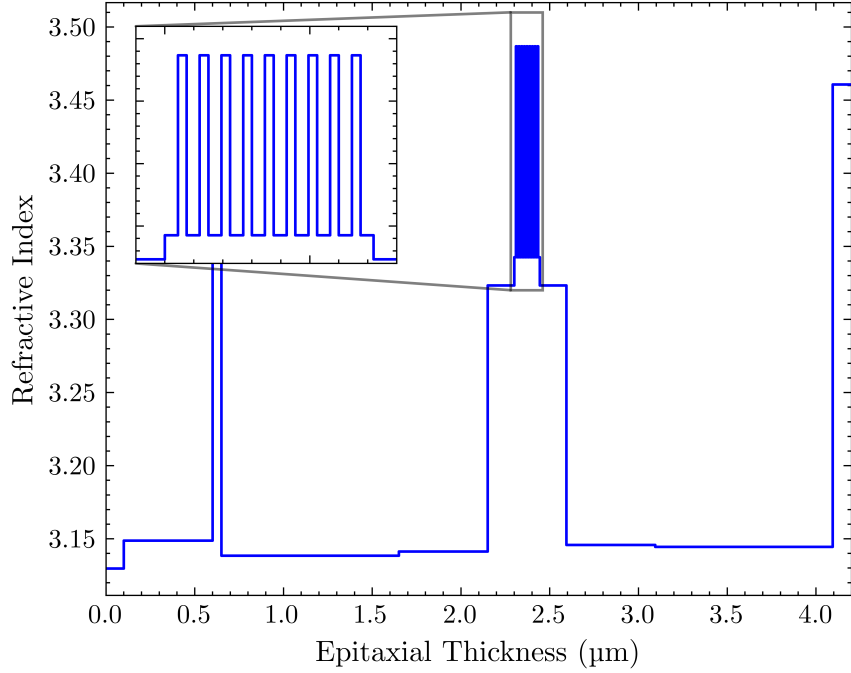


Figure 3.5: Refractive index profile of the 9QW epitaxial structure used in this work. Inset shows the region surrounding the 9QWs in the active region.

surrounded by two 150 nm InAlGaAs cladding layers. On top of the SCH a p-type InP upper cladding layer was grown with a thickness of 1500 nm. The final layer was a highly doped (10^{19} cm^{-3}) InGaAs contact layer, which aids in the formation of an ohmic contact during metallisation. The refractive index profile of this epitaxial structure is shown in Figure 3.5. In this graph, the zero value on the x-axis represents the bottom of the epitaxial stack, below which, the n-type InP substrate is located. The SCH can be seen at $2.2 \mu\text{m}$ above the substrate, including the QW structures that make up the active region as detailed in the inset of Figure 3.5. The lower refractive index portions either side of the SCH represent the lower and upper n- and p-type cladding regions that make up the waveguide. The high refractive index portion at the top of the epitaxial structure is the highly doped contact layer. Additionally, a high refractive index layer can be seen at $0.6 \mu\text{m}$ above the substrate. This was a micro transfer printing release layer and was unused in this work. Using this refractive index profile, the modes were then calculated and implemented in the effective index alteration method described in the previous section. Figure 3.6 shows both the TE_{00} and TE_{10} mode calculated for the averaged waveguide in an example structure. As seen in this Figure, the overlap of the grating region, Γ_g is small compared to if the

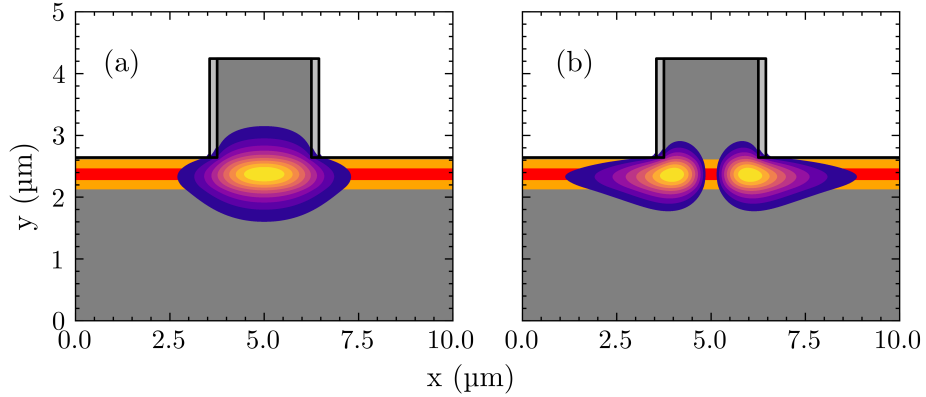


Figure 3.6: Calculated optical modes overlaid on an example LC-DFB cross section. (a) Fundamental mode, TE_{00} (b) 2nd bound mode, TE_{10} .

grating was positioned directly above the active region. This region, however, determines the coupling coefficient of the grating and so careful examination of the design parameters is necessary to optimise the overlap and thus obtain the correct coupling coefficient.

3.5.2 Etch Depth

The etch depth is an important parameter in the design process of a RWG laser. For a standard FP RWG laser structure, the ridge must be etched deep enough to provide the benefits associated with the lateral confinement provided by a RWG which include reduced threshold current and improved device efficiency. The etch depth also has a profound effect on the coupling coefficient of a LC-DFB. Figure 3.7, shows the coupling coefficient as a function of etch depth for both a first order grating and a third order grating. For both structures modelled here the ridge width was set to a value of $2\ \mu\text{m}$, the extrusion length was set to $0.2\ \mu\text{m}$ and the duty cycle was 0.5. At low etch depths of around $1.2\ \mu\text{m}$ the coupling coefficient is negligible since the grating is far away from the optical mode. In this regime, the etch depth is not sufficient to provide effective lateral confinement of the optical mode so the laser would effectively be gain guided due to current spreading underneath the ridge. According to Figure 3.7, as the etch depth is increased, the coupling coefficient increases rapidly especially for the 1st order device considered here. This continues as the grating is etched through the active region and the coupling coefficient stabilises at etch depths of around $3\ \mu\text{m}$. The reason for this is that at deeper etch depths, the optical mode is fully confined in

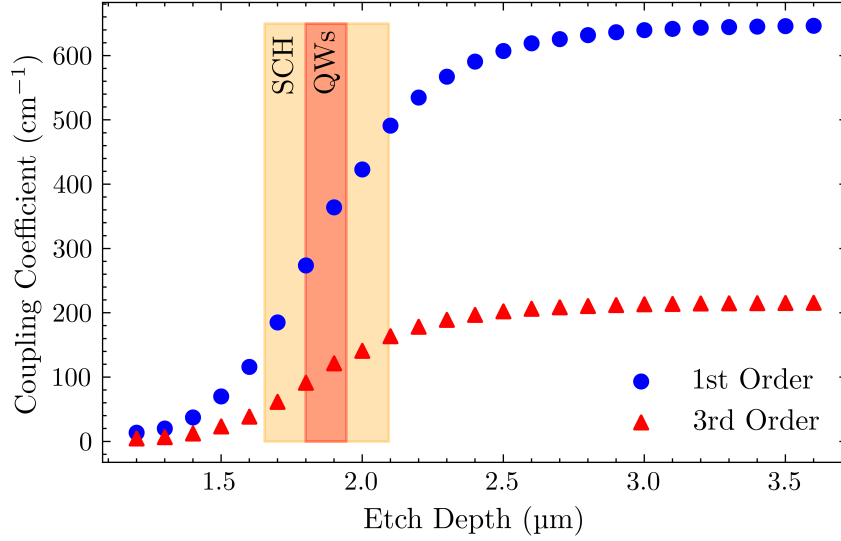


Figure 3.7: Coupling coefficient as a function of etch depth for both a 1st and 3rd order LC-DFB structure. The modelled ridge width was 2 μm , the extrusion length was set to 0.5 μm and the duty cycle was 0.5. The SCH and active regions are shown in yellow and red respectively.

the ridge so no further overlap of the mode with the grating region can be realised. From a design point of view, it would make more sense to design the laser with a deep etched RWG as the coupling coefficient is not sensitive to etch depth, which in some cases can be difficult to control accurately. In practise, however, etching through the QWs is not desirable as it is well known that dry etching introduces surface defects which can propagate through the active region, as well as introducing surface recombination [1]. These issues affect the performance and long term reliability of a laser diode [47]. As such, the etch depth was targeted to be in the region of 1.4 - 1.6 μm as this meant that the grating region was close enough the active region to provide meaningful coupling coefficient without etching into the SCH.

3.5.3 Ridge Width

The ridge width, W_R , refers to the width of the narrowest portion of the LC-DFB structure. For a FP RWG laser structure this width is chosen to be narrow enough that the device exhibits a single transverse mode. Doing this guarantees that the TE_{00} mode will be the lasing mode. The ridge must not be made too narrow, as the resistance increases with reduced device area. These factors place limits

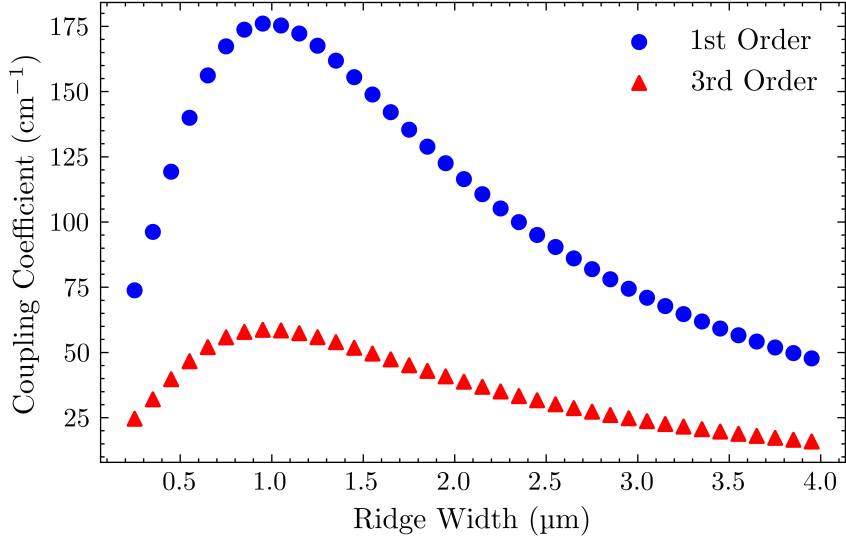


Figure 3.8: Coupling coefficient as a function of ridge width for both a 1st and 3rd order LC-DFB structure.

on the range of ridge widths than can be designed for the LC-DFB structures fabricated in this work. The ridge width also impacts the performance of the grating structure. Figure 3.8 shows the coupling coefficient as a function of ridge width for both a 1st order grating and a 3rd order grating. In this case the etch depth was fixed at a value of 1.6 μm , the extrusion length was chosen to be 0.2 μm and the duty cycle was 0.5 in both cases. It can be seen from Figure 3.8 that the coupling coefficient exhibits a maximum value at a ridge width of around 1 μm , beyond which, the coupling coefficient decreases steadily. This is due to the fact that widening the ridge causes the optical mode to be contained more within the ridge and as a result the overlap with the grating region is reduced. Reducing the ridge width also results in a sharp decline in coupling coefficient. The reason for this is that a narrower ridge causes the optical mode to be confined more strongly in the vertical direction, causing it to be pushed under the ridge. As a result, the grating sees less of the optical mode resulting in a diminished coupling coefficient. These effects are illustrated in figure 3.9, which shows the fundamental TE mode profile for different ridge widths. Also worth mentioning, is that the coupling coefficient is less sensitive to changes in both etch depth (Figure 3.7) and ridge width at higher grating orders. In Figure 3.8 for example, between a ridge width of 1.5 and 2 μm , the coupling coefficient declines by approximately 50 % for a 1st order grating. This decline is only 5 % for the 3rd order grating. This

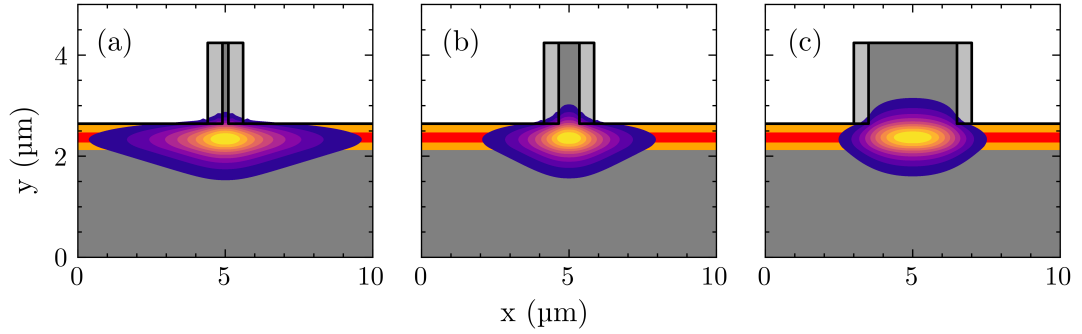


Figure 3.9: Fundamental TE mode profiles shown with the ridge waveguide cross section for a ridge width of (a) $0.2\ \mu\text{m}$, (b) $0.7\ \mu\text{m}$ and (c) $3.0\ \mu\text{m}$.

highlights the fact that increasing grating order relaxes demands on fabrication despite resulting in a reduced coupling coefficient. In this work, it was desired to ensure only a single transverse mode lasing, therefore, designs favoured ridge widths between 1.5 and $2\ \mu\text{m}$.

3.5.4 Extrusion Length

Extrusion length describes the extent to which the gratings extend beyond the ridge in the LC-DFB structure. The effect on the coupling coefficient when

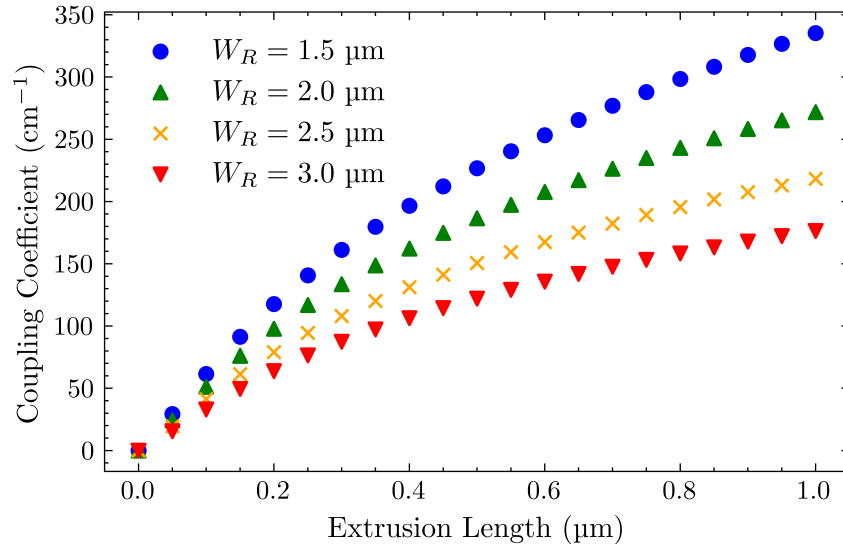


Figure 3.10: Coupling coefficient for a 1st order grating as a function of extrusion length for a selection of ridge widths. The etch depth was $1.6\ \mu\text{m}$ and the duty cycle was 0.5 .

changing the extrusion length for different ridge widths is shown in Figure 3.10. It can be seen that as the extrusion length is increased from zero, there is initially a sharp increase in coupling coefficient, however, as the extrusion length is increased further, the change in coupling coefficient becomes more gradual. As a result, extrusion length is perhaps the most fabrication friendly parameter considered here as coupling coefficient is not as sensitive to changes in this value as compared with the etch depth. Additionally, with high resolution patterning methods such as electron beam lithography this value can be controlled extremely well with precision on the order of 10s of nanometres or less. As a result, during the design process, the extrusion length was often used to fine tune the coupling coefficient once the other parameters had been chosen. Figure 3.10 shows how extrusion length affects the coupling coefficient for a 1st order grating. Notably, extrusion lengths less than 0.5 μm provide adequate coupling coefficients. When higher order gratings are considered this is not necessarily the case. Figure 3.11, shows the coupling coefficient as a function of the extrusion length for both 3rd and 11th order gratings where the etch depth was kept constant at 1.6 μm , the ridge width was selected to be 2 μm and the duty cycle was 0.5. Here it can be seen that when the extrusion length is 1 μm , the coupling coefficient is around 8 times higher in a 1st order grating than for an 11th order device and 4 times higher than a 3rd order grating. This highlights the fact that when increasing the grating order, higher extrusion lengths may be required to achieve the necessary coupling coefficient. This has implications for mode selection, which will be discussed later in this chapter.

3.5.5 Duty Cycle

The effect of duty cycle on the coupling coefficient of the LC-DFB structure is illustrated in Figure 3.12 for different grating orders. Figure 3.12a shows the coupling coefficient as a function of duty cycle for a 1st order grating, where the ridge width is 2 μm , the etch depth is 1.6 μm and the extrusion length is variable depending on grating order. In this case a single peak in the coupling coefficient is observed at a duty cycle of 0.6. As one increases the grating order the number of peaks and points where the coupling decays to zero also increases. This is described by the sine term in equation 3.7, which includes the grating order, m . Also shown in Figure 3.12, is that for all grating orders, the coupling coefficient peaks at a duty cycle higher than 0.5. This is not the case for a buried

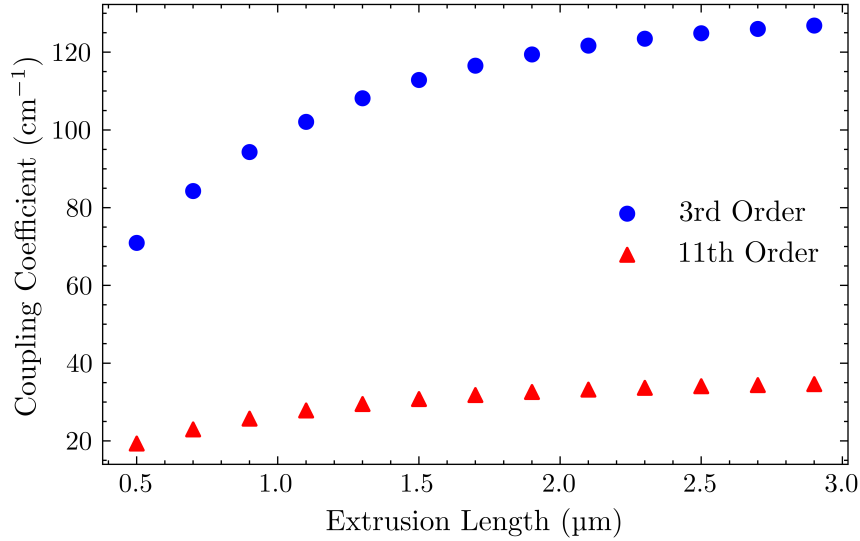


Figure 3.11: Coupling coefficient as a function of extrusion length for both a 3rd and 11th order LC-DFB laser structure. The ridge width was 2 μm, the etch depth was 1.6 μm and the duty cycle was 0.5.

grating DFB structure where the peak coupling coefficient will always be found at a duty cycle of 0.5, for all odd values of grating order. This is explained by the weighting function described in equation 3.8. When the duty cycle is increased, the average refractive index of the grating region also increases towards the value for the upper InP cladding layer. The increase in refractive index of the material surrounding the RWG allows the optical mode to extend further out as confinement is reduced. This results in an increased overlap with the grating region leading to higher coupling coefficient. In this work, 1st, 3rd and 11th order gratings have all been fabricated. From a fabrication standpoint, a duty cycle of 0.5 is easiest to fabricate as it maximises the minimum feature size. As such 2nd order gratings were not considered due to the fact that a duty cycle of around 0.75 would need to be chosen to maximise the coupling coefficient. Targeting 1550 nm, this correspond to a minimum feature size of 120 nm, which is the same as a 1st order grating designed with a duty cycle of 0.5. Finally, for higher order gratings it is clear that increasing the grating order has implications for fabrication. Specifically, using a grating order of 11 makes defining the gratings easier, offering the ability to use lower resolution techniques. There is, however, an issue in that the inaccuracy of the duty cycle does not have to be very large before the coupling coefficient decays to zero. This presents a challenge when attempting to use photolithography to define these structures for example, as

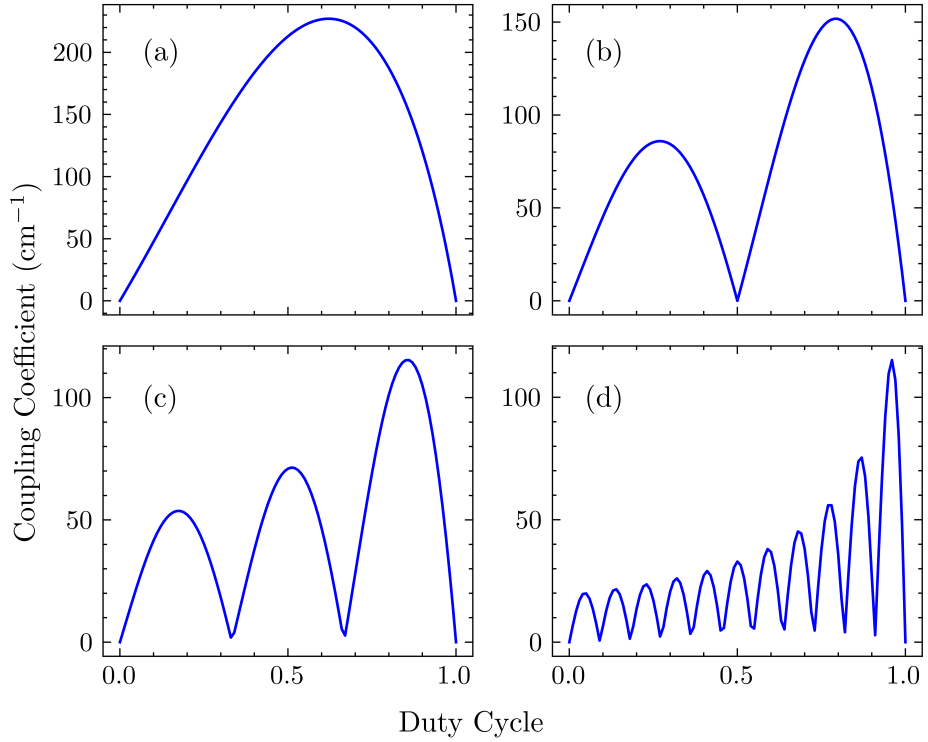


Figure 3.12: Coupling coefficient as a function of duty cycle for a (a) 1st order grating, (b) 2nd order grating, (c) 3rd order grating and (d) 11th order grating. The ridge width was 2 μm , the etch depth was 1.6 μm and the extrusion length was variable depending on grating order.

will be shown in chapter 5 of this thesis.

3.5.6 Transverse Mode Selection

In an earlier section of this chapter it was shown that in some cases the extrusion length must be made larger to facilitate lasing in LC-DFB devices with higher order gratings such as 11th order. As a result of increasing the extrusion length, the effective width of the grating structure increases. This means that in some cases the device may be able to support more than just the fundamental TE mode. In general, selection of the ridge width has been carefully chosen to limit the possibility of this happening. Nevertheless, it is important to be aware of how this effects the coupling coefficient of a LC-DFB grating. Figure 3.13 shows the coupling coefficient as a function of both the extrusion length (ridge width = 2.5 μm) and ridge width (extrusion length = 0.2 μm) for both the TE₀₀ mode and the TE₁₀ mode in a 1st order laterally coupled grating with an etch depth of 1.6 μm

and a duty cycle of 0.5. Figure 3.13a shows that at small extrusion lengths, the difference in coupling coefficient between the two modes is negligible. However, as the extrusion length is increased the TE_{10} mode exhibits a higher coupling coefficient. This is due to the shape of the optical mode, specifically, the fact that it is less confined under the ridge than the TE_{00} mode. As a result of this, the TE_{10} mode overlaps more with the grating region in the LC-DFB structure leading to a higher coupling coefficient. This is also seen in Figure 3.13b where there is a peak in coupling coefficient at around $2.7 \mu\text{m}$, after which increasing the ridge width further results in a reduced coupling coefficient. This is the same effect as was described in section 3.5.3 as at small ridge widths the optical mode begins to be pushed under the ridge and at elevated ridge widths, the mode becomes more confined within the ridge. Ultimately, the DFB lasing wavelength will be dependent on both the coupling coefficient of each of the confined transverse modes, as well as the detuning between their corresponding wavelength and the gain peak. During spectral measurements of a laser diode, higher order lateral mode lasing is characterised by a shift in the designed wavelength as the effective index of the higher order mode is different to that of the TE_{00} mode.

3.5.7 Selection of Coupling Coefficient

A discussion of how the coupling coefficient varies with a number of design parameters for a LC-DFB laser has been presented here. So far the specific ideal

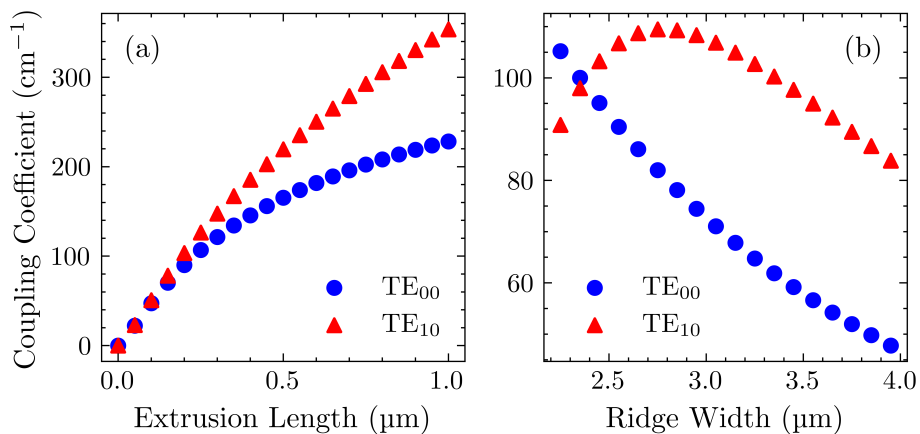


Figure 3.13: Coupling coefficient of both the fundamental TE mode and the second TE mode as a function of (a) extrusion length with a fixed ridge width of $2.5 \mu\text{m}$ and (b) ridge width with a fixed extrusion length of $0.2 \mu\text{m}$. In both cases the etch depth was $1.6 \mu\text{m}$ and the duty cycle was 0.5.

numerical values of coupling coefficient have not been considered. When selecting the ideal coupling coefficient, the targeted grating length must first be considered. This is usually the same as the cavity length in a DFB laser. The product of the coupling coefficient and the grating length, κL , ultimately decides what coupling coefficient should be targeted. In the literature, there have been various values quoted for this, depending on the type of structure being designed. Early work on the subject by Soda et al assessed the single mode yield of phaseshifted devices with varying coupling strengths. They found maximised yield when $\kappa L = 1.25$ [25]. Increasing beyond this point was found to increase the effects of spatial hole burning (SHB), which is caused by an increase in mode intensity around the phase shift section and leads to reduced side mode suppression ratio (SMSR). Work by David et al in 1991 compared the experimental and theoretical yield for various device configurations including uniform grating devices with facets as-cleaved. Their results suggest a maximum yield under these conditions when $\kappa L = 1 - 2$, depending on the degree of SHB [48]. Despite this, higher values have also been used to produce functional devices. For example, recent work by Kaneko et al in 2022 demonstrated a LC-DFB laser on InAs/InAlGaAs quantum dot material which exhibited single mode operation with an SMSR value exceeding 40 dB [49]. In this case, the designed κL value was 3 significantly higher than the previously mentioned studies recommended. Furthermore, Ye et al recently presented a LC-DFB laser integrated with a waveguide crossing. In this case, an SMSR value exceeding 45 dB was achieved. The coupling strength of this device was measured to be 65 cm^{-1} and the cavity length was $600 \mu\text{m}$, providing a κL value of 3.9 [50]. These results suggest that higher κL values can also achieve stable single mode performance. In this work, κL values between 1.25 and 3 have been targeted, with a wide range chosen to account for changes in the coupling strength as a result of variation in the device dimensions during fabrication.

3.6 Summary

This chapter has described the modelling techniques used to design the LC-DFB grating structures in this work. An introduction to the effective index alteration techniques was provided along with an overview of how changing parameters affects the coupling coefficient.

Traditional methods for calculating the coupling coefficient are not suitable for LC-DFB lasers due to the fact that the amplitude of the refractive index is assumed to be small. A method for calculating the coupling coefficient for LC-DFB lasers specifically was presented in [38]. Here the LC-DFB grating structure is separated into three waveguides, narrow, wide and averaged. The modulation is then described in terms of new effective indices, which are given by the overlap of optical mode of the averaged waveguide with the refractive index distribution of the narrow and wide waveguides.

Varying etch depth has a profound effect on the coupling coefficient at low etch values and stabilises at high etch values. Increasing the ridge width initially results in increased coupling coefficient until it peaks at around $1\ \mu\text{m}$ beyond which a decreased coupling coefficient is observed. Increasing the extrusion length results in increased coupling coefficient, with the rate of increase being increased at shorter extrusion lengths. Altering the duty cycle changes the coupling coefficient significantly, with higher duty cycles offering greater coupling coefficient values generally. Increasing the grating order introduces a series of peaks in the coupling coefficient dependence on duty cycle, which corresponds to the grating order term in the sine function. If a waveguide supports more than the TE_{00} mode, then higher order modes can exhibit higher coupling strengths and, therefore, may be preferred during operation of the device.

The gratings fabricated in this work have been designed with coupling coefficient values between 1.25 and 3, which corresponds to the range of recommended values quoted in the literature.

Chapter 4

Experimental Methods: Fabrication and Characterisation

This chapter will describe the experimental techniques used in both the fabrication and characterisation of the devices in this work. This will begin with a discussion of all the fabrication methods utilised in this work, along with examples of their use in a RWG process flow. This will be followed by a presentation of the characterisation methods and equipment used in device measurement.

4.1 Cleaning and Surface Preparation

Sample cleaning is an important step in any fabrication process as the existence of unwanted particles can destroy individual devices and reduce yield. The first component of minimising unwanted particles is through the use of the cleanroom environment. A cleanroom is a laboratory where the number of particles in the air is known and controlled through the use of air filtration and laminar or turbulent airflow. In addition to this, the temperature and humidity of the environment is also controlled. All of the fabrication in this work was carried out in class 1000 cleanrooms, with lithographic processes carried out in a class 100 area of the same cleanrooms.

4.1.1 Solvent Cleaning

Despite the controlled environment, it is still inevitable that some particle contamination of the semiconductor wafers will occur. For this reason, solvent cleaning is carried out throughout the fabrication process. This procedure is utilised to remove organic materials such as photoresist and oils [51]. If resist has been used, this begins with immersion in a dedicated resist stripper, usually at an elevated temperature. In this work NMP1165 has been used as well as MLO-07, for this purpose. Following this, the sample is immersed in the following order; acetone, methanol and isopropanol (IPA). The order is important because acetone is the best for removal of organic impurities but it leaves a residue that is hard to remove if allowed to dry. Methanol is effective at removing this residue and so is used second. IPA is the final solvent because it rinses the acetone and methanol residue effectively and evaporates slowly, removing contaminants in the process and leaving no residue. A rinse in de-ionised (DI) water can also be used at the end of this process as a final rinse to prepare for future processing. During all of these solvent cleaning steps, ultrasonic can also be used to physically agitate the surface and speed up the cleaning procedure. In this work, all processing was performed on InP tiles, which is relatively fragile compared to other III-Vs such as GaAs. Therefore, extra care was taken through the use of reduced ultrasonic power to avoid breaking the sample.

4.1.2 Oxygen Ashing

Oxygen ashing is a plasma etching technique that is used to remove organics from the wafer. The mechanism for this is the dissociation of the oxygen molecule into more volatile products including carbon monoxide and carbon dioxide. Ashing was used throughout the fabrication processes in this work. It was utilised at the end of the general solvent cleaning procedure described in section 4.1.1 as a final resist removal step, as well as after the development in any lithographic process. This serves as a descum to remove the very thin layers of resist that exist after development. Leaving these could hinder the adhesion of deposited materials in further processes. Although ashing is an extremely useful technique in maintaining substrate cleanliness, it can leave an oxide in exposed indium phosphide, this sometimes requires removal which is described in section 4.1.3.

4.1.3 Acid Surface Preparation

Ensuring good adhesion of deposited materials is vital for optimal device performance. As mentioned in section 4.1.2, an oxide can be present on the surface of InP either as a result of oxygen ashing or simply exposure to air. For good adhesion at for example, contact-metal or dielectric-semiconductor interfaces, it is helpful to remove the oxide layer leaving a fresh InP layer. This is done by immersing the wafer in a solution that etches the native oxide away. There are a number of appropriate solutions described in the literature for both InP and GaAs [52, 53]. Typically however, the solutions involve a strong acid such as hydrochloric acid (HCl) or base such as ammonium hydroxide (NH_4OH) diluted in de-ionised water. In this work, the top-layer of the epitaxial structures usually consisted of a highly doped InGaAs layer so a solution of $\text{NH}_4\text{OH}:\text{H}_2\text{O}$ (1:10) was chosen to remove the native oxide prior to dielectric or p-contact metals. Since the n-contacts were deposited onto the InP substrate a different chemistry was used to remove the native oxide. In this case a solution of $\text{HCl}:\text{H}_2\text{O}$ (1:1) was used.

4.2 Lithography

Lithography is the process by which, patterns are added to semiconductor material. An example of a lithography process for the definition of a RWG is shown in Figure 4.1. The process begins with the epitaxial stack, upon which a hard mask is deposited using the technique described in section 4.6.1. A light/electron sensitive polymer is then applied to the surface, as shown in Figure 4.1c. The resist is then exposed, which either damages the bonds in the resist molecules (positive tone) or cross-links the resist (negative tone). Figure 4.1d illustrates this for a negative tone photoresist. Following exposure, the sample is then immersed in a developer, which selectively removes resist. In the example shown in Figure 4.1e, the unexposed resist has been removed. Following a lithography process, the pattern can be transferred to the semiconductor material through either an additive process such as deposition and lift off, which will be described in section 4.6, or a subtractive process like etching (section 4.4). In this work, a number of lithography techniques were used to define the ridges and gratings that constitute the LC-DFB laser cavity, the oxide isolation regions to facilitate current flow and the metal contacts. Two techniques have been used in this work, which

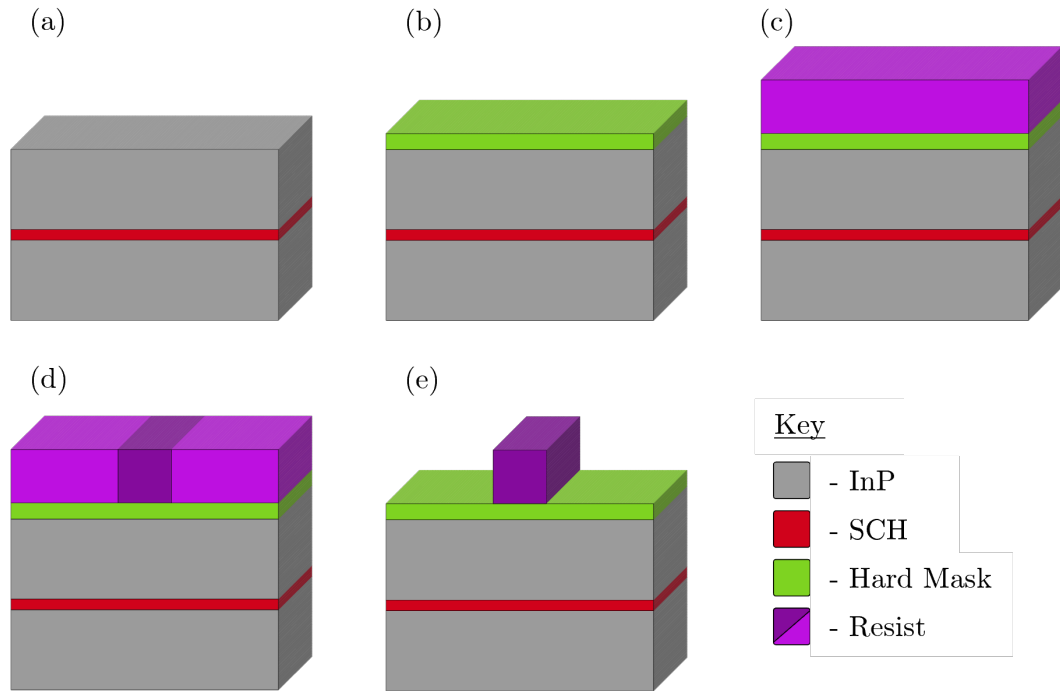


Figure 4.1: Typical RWG lithography process flow. (a) Basic epitaxial structure, (b) Deposition of the hard mask, (c) Application of photoresist, (d) Exposure of the photoresist, exposed area is darker, (e) Development of the resist, leaving the patterned RWG.

were mask-less projection lithography and e-beam lithography. The following sections will describe these technologies as well as some important considerations in lithography processes.

4.2.1 Resist Preparation and Selection

To guarantee resist adhesion to the substrate, several steps were undertaken. Once a cleaning procedure has been applied such as that described in section 4.1, the surface was prepared for the resist applications by performing a dehydration bake, followed by the application of an adhesion promoter. Many options for this step exist, however, in this work both Ti-Prime and Hexamethyl Disilazane (HMDS) were used. Adhesion promoters work by introducing a submonolayer on the surface of the material making the surface slightly hydrophilic, improving resist adhesion in the process [54].

Choosing the correct resist is extremely important and there are many options available. The decision generally comes down to what subsequent step will be

carried out with the resist in place. For example if a deposition and lift off is being performed, a large undercut would be desired so that the resist removal solvent can access the resist under the deposited material. If an etch will be performed the primary concern is that the resist is sufficiently resistant to the etch in order to provide high selectivity for the material being targeted by the etch. Additionally for a dry etch, a more vertical profile is generally required so as to promote a vertical profile in the etch. In this work, a number of resists have been used. For the majority of the photolithography, the AZ family of negative photoresists were used due to their ability to provide vertical profiles for etching as well as undercuts for lift off depending on how they are processed. Additionally, an electron beam lithography process using diluted AZ2020 has been developed for the fabrication of LC-DFB gratings, which will be described in chapter 6.

The process of applying the resist was done through the use of spin coating. This involved dropping the required amount of resist onto the wafer and spinning at speeds of 1000's of rpm. Spin speed is the primary way of controlling the thickness of the resist and resist manufacturers will typically provide data describing thickness as a function of spin speed. The final step in preparing the resist is known as a softbake. This bake was used to remove the remaining solvent from the resist after it had been spun.

4.2.2 Maskless Optical Projection Lithography

The traditional method of performing optical lithography in a research environment involves using a mask aligner which involves shining light through a physical mask, that contains the design to be patterned, onto the sample. In high throughput applications such as silicon chip manufacturing optical projection lithography systems are used (also known as steppers) with reticles as the physical mask. There is a large cost associated with physical mask/reticle production however, as they are usually patterned externally with e-beam lithography. Furthermore, changes cannot be made to the mask once it has been made, so it is difficult to adapt the design as is often required in a research environment. In response to these issues considerable effort has gone into developing mask-less lithography techniques [55]. An example of one of these techniques is maskless optical projection lithography (MOPL). In this work, two MOPL systems were used, the first was a Heidelberg MLA150 a schematic of which is shown in Figure 4.2. In

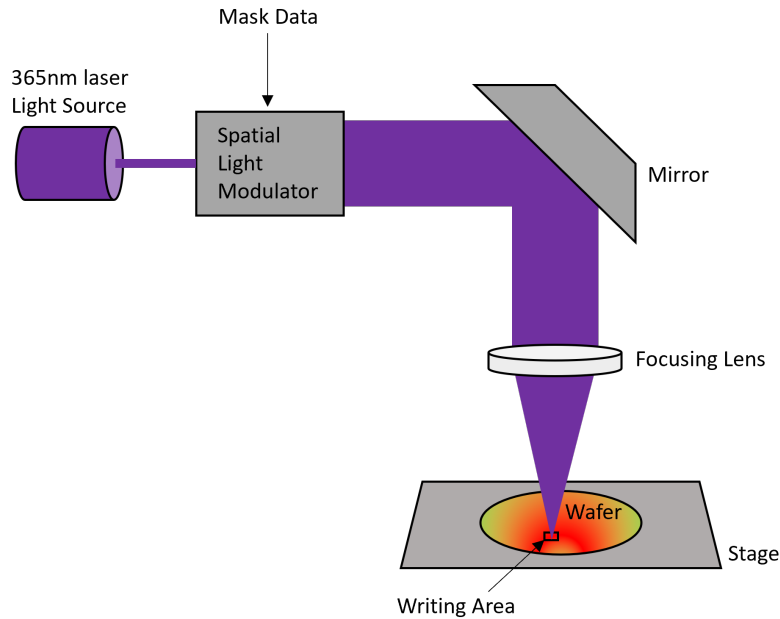


Figure 4.2: Simplified schematic of the Heidelberg MLA150 maskless optical projection system used in this work.

this system the spatial light modulator (SLM), which is an array of electrically controlled micromirrors, takes the place of the physical mask. The mask data is transferred to the SLM from which tilts the mirrors to produce the required image [56]. This image is beamed through a series of projection optics and onto the wafer surface. This makes this system more like a stepper than a traditional mask aligner as only a small area of the wafer is being exposed at a given time. The second MOPL system used in this work was a Durham Magneto Optics Microwriter ML3 pro. The principle of operation is the same for this system however a digital micromirror device (DMD) is used instead of the SLM. The DMD is also an array of mirrors but is slightly simpler in that the mirrors can either be on or off and are set before an exposure rather than controlled during exposure such as in a SLM [57]. The result of this is slightly longer exposure times but resolution is similar.

4.2.3 Electron Beam Lithography

For 1st - 3rd order DFB lasers operating at 1550nm, the minimum feature size is on the order of 100-300 nm. Therefore, there are a limited selection of methods that can pattern closely spaced designs at this resolution. The most developed of

these, particularly in research environments is electron beam lithography (EBL). An EBL tool utilises an electron emission source such as a tungsten tip or a field emission gun (FEG). The electrons from the source are focused onto the sample through a series of electrostatic lenses. In this work, a Raith 5200+ 100kV electron beam lithography system was used. A full discussion of EBL is beyond the scope of this work. There are, however, a number of basic concepts that are very relevant in the fabrication of DFB laser gratings. These will be described below.

Proximity Effect and Correction

In EBL the resolution is limited by two main things. The first of these is aberrations in the electron optics used to focus the beam. This cannot be corrected by the user as it is generally an attribute of the system being used. The second limiter of resolution in EBL is known as the proximity effect. Broadly this describes how the electrons scatter as they interact with both the resist and the substrate. The result of this is that exposed patterns become wider than intended due to the resist being exposed outside the region defined by the designed pattern. There are two types of scattering that electrons undergo when they enter a material. The first of these is known as forward scattering where an electron has a collision with an electron in either the resist or the substrate. These are generally small angle collisions and if they occur with an electron in the resist, the molecule may be broken by this interaction. The second type of interaction is called backscattering. In this case the electron collides with the nucleus of an atom, usually within the substrate. Collisions of this nature result in large changes in direction of the electrons while they retain most of their energy. As such the electrons re-penetrate the resist at distances far away from their initial point of incidence, resulting in more exposure of the resist. It is the backscattering interactions that are the main cause of the proximity effect. The electrons coming straight from the beam are known as primary electrons and as they interact with the resist they lose energy in the form of secondary electrons. It is these secondary electrons that cause the exposure of the resist predominantly. Since it is not the point like beam that causes most of the exposure however, there is a broadening of the exposed area in practise. It is worth noting that beam energy changes the interactions in the resist significantly. A higher beam energy results in greater penetration and less forward scattering allowing thicker resists to be used but at the cost of

increased backscattering as more electrons are entering the substrate. Using a beam with lower energy results in less backscattering but forward scattering is increased meaning that thinner resists must be used [58].

Whilst a hindrance, the proximity effect can be mitigated using a proximity effect correction. Significant effort has gone into accurate simulations of the proximity effect and commercial software is available that provides highly accurate and customisable proximity effect corrections. In this work, the commercial software provided by GenISys, called Tracer and Beamer, were used exclusively for EBL proximity corrections. Tracer performs Monte Carlo simulations to calculate the absorbed energy spread at given points in the resist. The output of this is a point spread function (PSF) that describes the absorbed energy in the resist at any position [59]. This can then be combined with the Beamer software to perform the final proximity effect correction on the desired pattern. Whilst other types of proximity effect correction exist, most commercial software, including Beamer, use what is called the dose modulation method. This method involves dividing the design into a number of shapes that are each given a designated dose such that they will be patterned true to the design. The result of this is that shapes that are in close proximity to other shapes will be given a reduced dose to compensate for the effects from neighbouring shapes and those that are isolated will be given an increased dose. Applying a correction in this way will make the dimensions of the features that are patterned closer to the designed values.

Beam and Patterning Parameters

Alongside, proximity effect correction there are a few other parameters that must be chosen during the data preparation process. The first of these is the beam step size (BSS) which defines the distance between individual beam shots. This must be chosen with the expected diameter of the beam spot in mind so as to avoid leaving areas unexposed. Reducing the BSS will increase the size control along with improving the smoothness of feature edges as long as an appropriate beam current is used to limit the size of the beam spot. This comes at a cost of increased patterning time, however [58].

Another patterning parameter that is important, especially for DFB lasers where there are long continuous patterned areas, is the writefield. When considering the writefield both the size and alignment are important. Practically, the writefield

is the area that can be patterned by deflection of the electron beam. Patterning beyond this region requires a stage movement to be performed which may cause errors in the pattern called stitching errors. An example of a stitching error, which has been transferred to the epitaxial structure using an etch is shown in Figure 4.3. These errors can be minimised through the use of writefield alignment procedures or advanced techniques such as multipass writing. The EBL tool used in this work had a writefield size of approximately 1 mm.

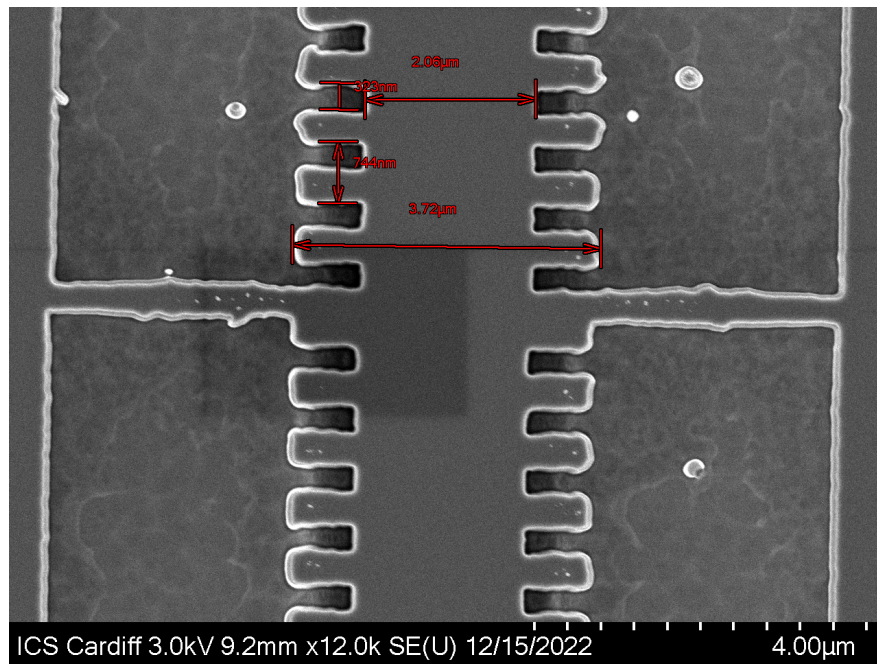


Figure 4.3: Example of a stitching error that has been transferred to the epitaxial structure using an etch. The gap between two writefields has meant that a line has been left unexposed in the middle of the ridge/grating structure.

4.3 Focused Ion Beam Nanofabrication

Another type of patterning method which has been used extensively in this work is focused ion beam (FIB) nanofabrication. This technique is, in some ways, a combination of etching and lithography. Like EBL, FIB nanofabrication is a direct write technique, that involves dividing the designed pattern into individual pixels or beam shots. Unlike EBL, however, the FIB can be used to remove material during patterning, removing the need for a resist. Alongside this, FIB can be used to pattern resist [60], selectively implant regions of a substrate [61] and deposit material on a substrate for subsequent inspection [62]. The FIB

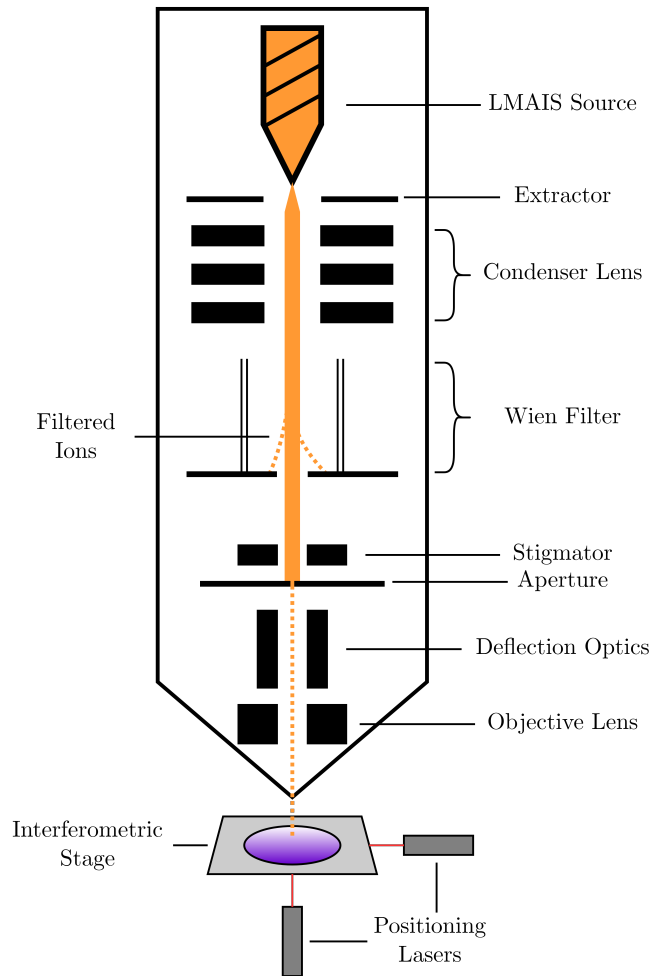


Figure 4.4: Simplified schematic showing the FIB column of the Raith Velion used in this work.

nanofabrication system used in this work was a Raith Velion, which included a top-down FIB column with an angled scanning electron microscope (SEM) column. A simplified schematic of the FIB column of the Velion is shown in Figure 4.4. The source is a liquid metal alloy ion source (LMAIS). In this work, both a gallium bismuth lithium (GaBiLi) and a gold germanium silicon (AuGeSi) source were used. The advantage of these sources is that varying size ions can be included, which facilitates faster milling with heavy ions like Bi and Au, whilst allowing imaging with smaller ions such as Li. The ions are selected with a Wien filter which removes unwanted ions depending on voltage applied to it. The lenses included in the system are similar to an EBL system, with the beam current controlled by an aperture set, which limits the flow of ions. The Velion system also has an interferometric stage, which is fairly unique among FIB systems. This

facilitates patterning over a large area with stitching like an EBL system. FIB nanofabrication offers a wide range of flexibility over patterning methods and has been used to directly mill grating structures, which will be described in chapter 7 of this thesis.

4.4 Etching

In many cases, once a lithography step has been performed, there is a requirement to transfer the designed pattern into the epitaxial structure. If the intention is to remove material during this pattern transfer, then etching is used. Etching can be separated into two types; dry etching and wet etching. The chosen method for a given step depends on a number of factors but speaking generally, if a vertical sidewall is required such as for the etching of a ridge in a RWG laser, then a dry etch is used, as it provides more anisotropic etching. This means that the etch is directional usually only acting downwards onto the sample. Wet etching is used when a more isotropic etch is required. This means that the etch rate

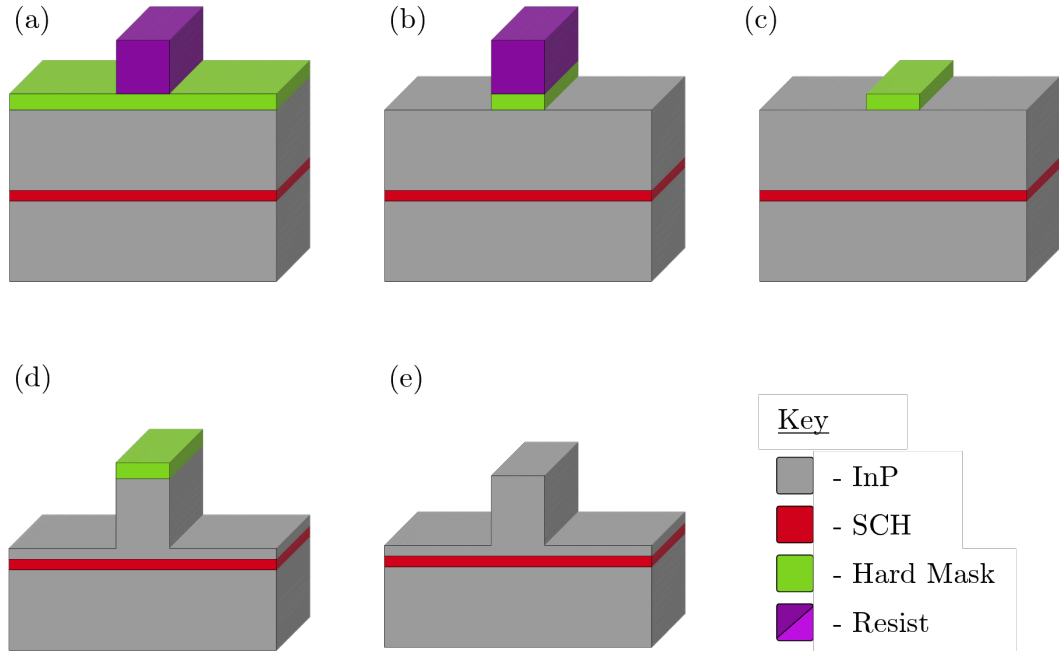


Figure 4.5: A typical RWG etching process. (a) Patterned RWG in resist, (b) Dry etch process to transfer the pattern into the hard mask, (c) Stripping of the resist to prepare for the epitaxial etch, (d) Etching of the epitaxial structure, (e) Removal of the remaining hard mask using a dry or wet etch process.

laterally is approximately the same as the rate vertically although it does vary somewhat depending on crystal structure. Both have their use in semiconductor laser fabrication. An example of an etch process for a RWG laser is shown in Figure 4.5. The process begins with the RWG defined in resist, using the method shown in Figure 4.1. This is followed by a dry etch of the hard mask, transferring the RWG into this layer (Figure 4.5b). The remaining resist is then stripped, as shown in Figure 4.5c. The epitaxial structure can then be etched to create the RWG, as shown in Figure 4.5d. Once the remaining hard mask has been removed using an additional etch, the RWG structure is complete (Figure 4.5e). There are a number of considerations that must be made when deciding on an etch process. A brief account of these and the specific etching techniques used in this work is provided in the following sections.

4.4.1 Plasma Assisted Etching

Plasma assisted etching can be described as any etching process that uses a plasma to generate reactive species which etch the target material chemically. This can be done in a purely chemical way in which case the resulting etch will be fairly isotropic, or the etch can be assisted kinetically, by encouraging the ions to interact with the material in a directional way. Reactive ion etching (RIE) is an example of such a technique, where a radio frequency (RF) field is applied to the target substrate. This field causes ionisation of the gas molecules in the chamber and a plasma is generated. As a result of the RF field, electrons move up and down the chamber. Those that are deposited on the target material cause it to build up a charge. Since there is a voltage difference between the positive plasma and the negative sample, the ions in the chamber move towards the sample where they undergo chemical reactions, removing the target material. Since the ions are impacting in a vertical way, the etch profile is strongly anisotropic [51]. In this work, RIE has been used extensively for the back etching of benzocyclobutene (BCB) which is a spin on dielectric as well as for the etching of hard masks.

4.4.2 Inductively Coupled Plasma Etching

RIE etching (described in the previous section) offers a rather slow etch rate. The major reason for this is that the plasma density is limited. One way of increasing the density of plasma and thus increasing the etch rate, is to use inductively

coupled plasma (ICP) RIE. In this case, the plasma is generated by an RF coil around the chamber rather than parallel electrodes like in a standard RIE system. This, along with a separate RF generator powering the substrate holder, means that the plasma flux can be controlled independently by changing the inductive power [63]. The degree to which the ions are accelerated is controlled by changing the RF power on the substrate holder. As a result of this, ICP-RIE systems offer a high degree of process control, meaning that the etch rate can be tuned precisely along with the etching profile achieved [64]. Furthermore, ICP-RIE systems can provide high-density plasmas even at lower pressure, which results in reduced sidewall roughness and improved anisotropy over RIE [65]. For these reasons, ICP-RIE has been used extensively in this work both for etching hard masks as well as transferring patterns into InP epitaxial structures. Particular considerations for etching InP laser structures will be described in the following section.

4.4.3 Etching Considerations

There are a number of parameters that must be considered when developing an etch process on InP-based epitaxial structures. Additionally, before pattern transfer into the epitaxial structure can take place, often a hard mask must be etched, which adds further complexity. This section will attempt to discuss some of the key considerations involved in etch process development.

Etch Gases

The first consideration is the decision on which gases will be used to generate the plasma and thus remove the target material. Three things should happen in this process; firstly the reactive species within the plasma should be absorbed onto the surface of the target material. Secondly, a chemical reaction will occur at the interface and thirdly, the resulting products should be removed. Commonly chosen compounds for dry etching in general include species containing fluorine, chlorine or oxygen. Oxygen is typically employed when removing polymers and organic compounds such as in the cleaning process of ashing described in section 4.1.2. For InP based epitaxial structures, fluorine based compounds cannot be used, as indium fluorides are not volatile. Therefore, chlorine based etches are typically used for the removal of InP materials. Because of the relatively low

volatility between indium and chlorine, this type of dry etch is typically done at elevated temperatures of around 200°C. This ensures a reasonable etch rate and a profile with minimised surface roughness [66]. In this work, a chlorine/argon ICP etch has been used exclusively to transfer patterns into InP epitaxial structures. Since this type of etch requires high temperatures, the standard option of using photoresist or EBL resist as the etch mask for this would not work, as photoresist would degrade at these elevated temperatures. As a result, hard masks are often used in a two-step process where the first etch is performed at ambient temperature with resist acting as a mask to transfer the pattern into the dielectric hard-mask. This is then followed by removal of the resist and a second etch of the InP epitaxial structure with the dielectric acting as the mask. This means that the first etch chemistry must be chosen such that the dimensions of the original pattern in resist are preserved as well as possible and the profile of the mask etch is suitable. Specifically, any side wall angle that exists in the hard mask will be patterned into the target material to some degree as the mask recedes in the etch. In this work SiO₂ hard masks were used and ICP-RIE etch steps using C₄F₈ + O₂ chemistries as well as RIE etching using SF₆ + N₂ were used to etch this material. The addition of oxygen in the ICP-RIE etch encourages the removal of the polymer which is deposited as a result of the fluorine reacting with the SiO₂. The SF₆ based RIE etch was used where EBL resists such as Poly methyl methacrylate (PMMA) were required as the inert nitrogen in this recipe limited how quickly the PMMA was stripped.

Mask Selection and Selectivity

Mask selection is a major determinant of etch quality particularly when it comes to the etch profile. For example, if there is significant surface roughness in an etch mask this will be transferred to the real structure. In the case of a semiconductor laser, this will have an impact on device performance, particularly if the surface is interacting with the lasing mode of the device. Furthermore, having high quality interfaces is essential for gratings, so getting mask selection right is extremely important in the fabrication of LC-DFB lasers. Since the first mask in an etch process is always a patterned mask, this selection also has lithography considerations. The resist must be chosen such that it has sufficient resistance to a dry etch whilst also providing the necessary resolution. In general there is a trade off between resolution and resist thickness. Where a thicker resist may be

more desirable for an etch it might not provide the highest possible resolution. This is especially true in EBL, and was one of the main reasons that a process for EBL was developed on the conventional negative tone photoresist, AZ2020. This allowed a high aspect ratio etch to be performed with sub 100 nm resolution. The development of this process will be described in chapter 6 of this thesis. The suitability of an etch mask is generally described by its selectivity. This is the ratio of the etch rate of the target material and the etch rate of the mask. For the fluorine based etch used in this work to etch films of SiO_2 the selectivity between the photoresist AZ2020 and SiO_2 is around 1:1. This means that if the resist was spun on to a thickness of $2\ \mu\text{m}$, then one would expect to be able to etch around the same thickness of SiO_2 . In practise however there is a degree of variability from etch to etch so it is advisable to have the resist mask be slightly thicker than the hard mask being etched. For the InP etch with chlorine based chemistry, the selectivity was found to be around 10:1. This means that a SiO_2 mask around 200 nm thick should be able to etch around $2\ \mu\text{m}$ of InP. When working with the InP material system it is often advisable to use only as much hard mask as is required, due to the fact that certain deposition techniques can cause large amounts of strain when thick films are deposited, potentially resulting in cracking of the deposited mask.

4.5 Planarisation

In the fabrication of RWG lasers, the ridge is usually encased within a dielectric to ensure that current only flows through the RWG. Additionally, when a p-contact is deposited using a line-of-sight technique such as thermal evaporation (section 4.6), the sample generally cannot have complex topography on it. Therefore, benzocyclobutene (BCB) can be used to planarise the sample for the application of contacts. Since BCB has a refractive index of around 1.5 it also acts to confine the optical mode. In this work, BCB has also been used to provide the low-index component of the LC-DFB grating structures. A typical process for applying BCB is shown in Figure 4.6. Following surface preparation procedures, the BCB is spin coated onto the sample, as shown in Figure 4.6b. Following this, the BCB is partially cured at $210\ ^\circ\text{C}$ for 40 minutes in a nitrogen atmosphere. The BCB is then back-etched so that its height is just under the height of the ridge. This provides an almost flat surface for the p-contact to be applied. The BCB also

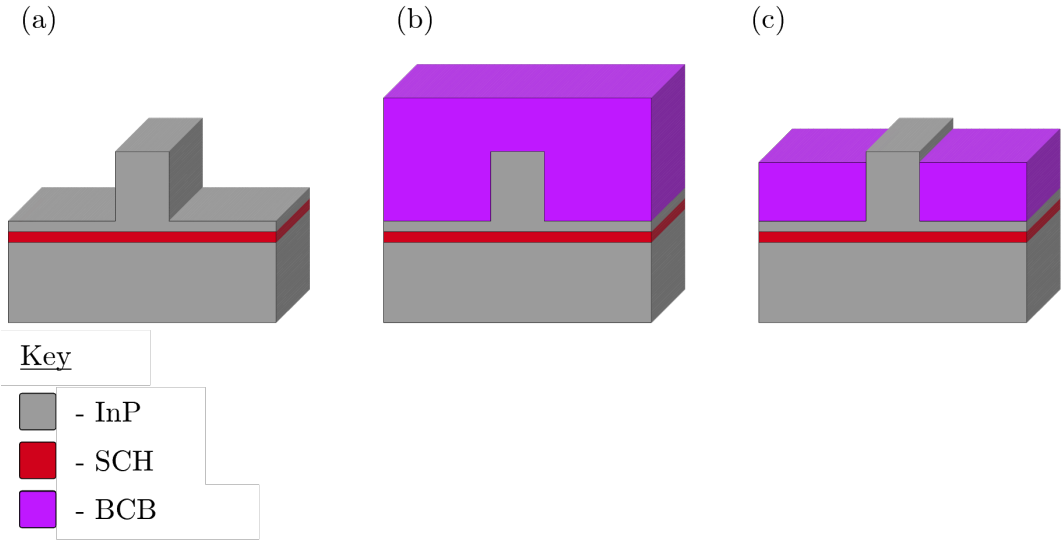


Figure 4.6: A BCB planarisation process. (a) RWG structure following the etch process, (b) Spin coating of the BCB dielectric, (c) Back etching of the BCB to reveal the top of the RWG.

requires a final hard-cure at 250 °C for 1 hour [67]. In this work, this has been combined with the annealing of the metal contacts at the end of a process.

4.6 Vacuum Deposition

In many cases, additive steps are required to transfer patterns onto the substrate. A good example of this is for metal contacts, for which an example process is shown in Figure 4.7. Here the process for depositing a p- and n-contact onto a RWG laser diode structure is shown. The process begins with a lithography process for the p-contact (Figure 4.7a-c). The resist is chosen such that an undercut is achieved, which prevents the deposited gold lining the sidewalls and preventing removal, as shown in Figure 4.7d. The sample is then immersed in resist stripper, removing both the resist and the metal on top, which is known as lift-off (Figure 4.7e). Following completion of the p-contact, the sample is thinned using a lapping process, which is described in section 4.7. After this, the n-contact can then be deposited on the substrate side of the sample (Figure 4.7f). The following section will summarise the deposition techniques used in this work and explain where they were used.

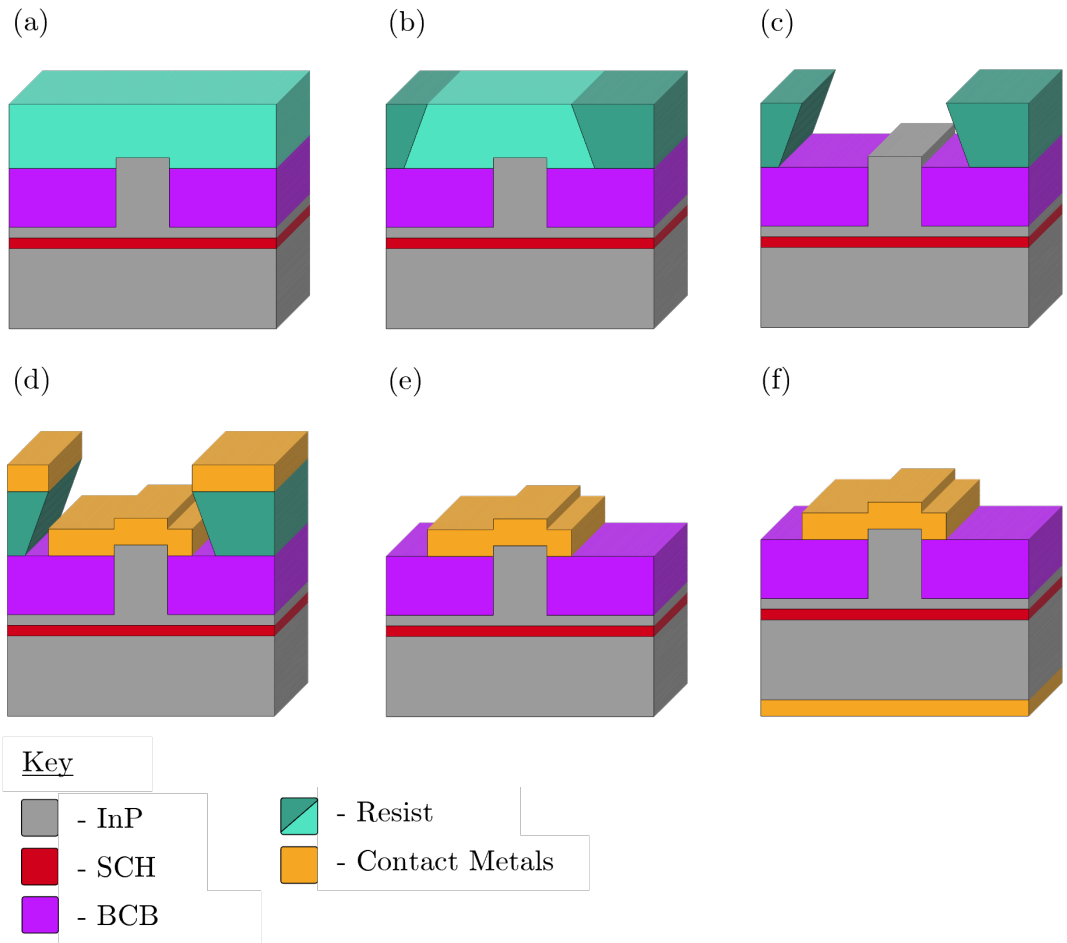


Figure 4.7: A lift-off process for p-contact deposition. (a) Application of photoresist, (b) Exposure of the resist using photolithography, exposed areas are darker, (c) Development of the resist with the resist undercut shown, (d) Deposition of the p-contact using a line-of-sight technique, (e) Stripping of the resist to reveal the p-contact, (f) Deposition of the n-contact on the underside of the device following a substrate thinning procedure.

4.6.1 Physical Vapour Deposition

Generally speaking, physical vapour deposition (PVD) describes any process where the desired deposition material is vapourised such that it is deposited onto the target substrate. It is usually done at high vacuum on the order of 10^{-6} mbar so that the mean free path of the vapourised atoms is extended to facilitate a good deposition rate.

Thermal Evaporation

Perhaps the most basic form of PVD is known as thermal evaporation. This process involves heating the desired material in a crucible or boat such that it begins to sublimate. A current is passed through the crucible in order to heat it up, which in turn heats up the deposition material. Thermal evaporation is a line-of-sight deposition method, which means that only parts of the sample that are in direct view of the deposition material will be deposited on. This can be helpful, since it facilitates easier lift off, however, if there is complex topography on the sample, thermal evaporation is not suitable as it will not cover large steps resulting in gaps in the deposited material. In this work, BCB was used to planarise the surface topography in order to allow line-of-sight deposition techniques to be used for contact deposition. Thermal evaporation has been used exclusively for depositing AuGe/Ni/Au n-contacts [68], as well as depositing Au in p-contact recipes. The other metals forming the p-contact were deposited by methods described in the following sections.

E-beam Evaporation

A similar technique to thermal evaporation, e-beam evaporation also involves heating the deposition material, such that it vapourises onto the target substrate. However, in this case the heating is provided by an electron beam that is rastered across the crucible containing the deposition material. This method is slightly more complex and expensive when compared to thermal evaporation but it provides the advantage of heating materials to higher temperature than thermal evaporation. This means that metals with higher melting points than would be suitable for thermal evaporation, such as titanium or platinum, can be deposited and deposition rates are higher. Once again, this technique is line of sight so complex topographies cannot be coated but lift-off processes are easy to

complete. In this work, e-beam evaporation has been used to deposit adhesion and buffer layers of titanium and platinum respectively for p-contacts (Ti/Pt/Au), as well as for depositing silicon dioxide hard masks for a subsequent ICP etch.

Sputtering

The final PVD technique used in this work, and the most complex, is sputtering. In this method, a highly pure source material known as a sputter target is placed within a plasma. Ions in the plasma impact the target causing atoms from it to be ejected, which then travel to the target material and condense onto it. The physics behind this technique is relatively complex compared to the other PVD techniques discussed here and is beyond the scope of this chapter. This complexity however means that sputtering is highly controllable and can provide very high quality thin films [69]. This method is also more conformal rather than being purely line of sight. This means that complex topographies can be coated but performing a lift-off with photoresist is slightly more challenging, often requiring multiple layers of resist. Other advantages of this technique include less heating in the system and a wide variety of available materials. Sputtering has been used in this work to deposit Ti in p-contact stacks as less peeling of the contacts was observed during wirebonding when the titanium layer was sputtered compared to when it was applied using e-beam deposition.

4.7 Device Preparation

In order to allow the sample to be cleaved easily and for efficient heat dissipation in the device, it is necessary to thin or lap the sample. This is done using a rotating disk with a silicon carbide abrasive attached to it. The samples in this work were thinned to 120 μm and subsequently polished to provide a high quality surface that the n-contacts could adhere well to. Following this they were cleaved into bars of lengths varying from around 250 μm to 1200 μm , which were then mounted to a copper block and TO-8 device header using silver-loaded conductive epoxy. The final step in this process, after which the devices can be measured, is wirebonding. In this work a wedge bonding system was used to attach a 30 μm thick gold wire to the p-contacts of the devices to provide current flow. The end result of this is shown in Figure 4.8.

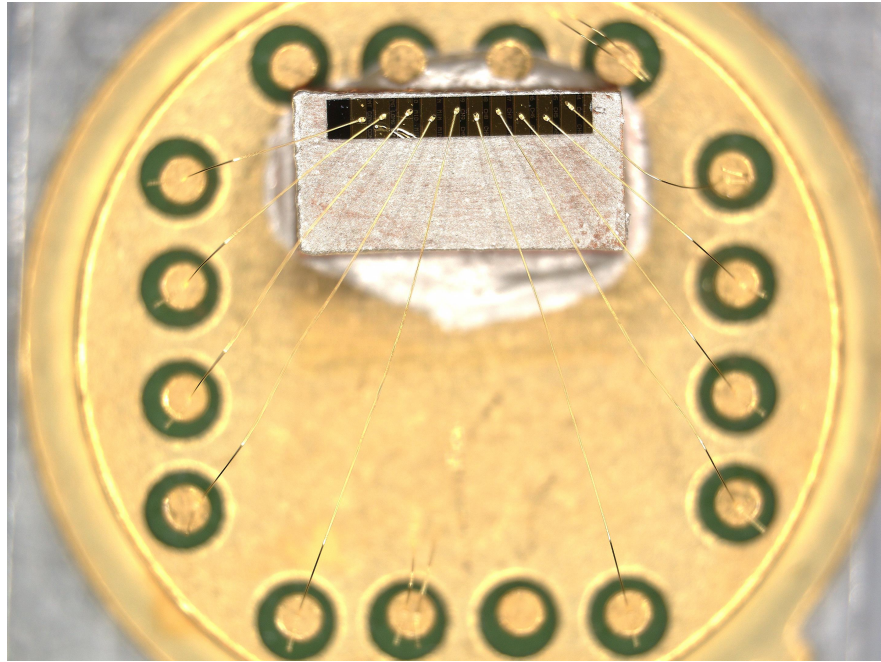


Figure 4.8: An example of a laser bar which has been lapped, cleaved, mounted and wirebonded. These devices are ready for measuring at this point.

4.8 Device Imaging and Checks

Throughout the processes described above, many checks are performed to verify the success of different steps as well as the dimensions of fabricated structures. For large scale structures on the order of microns, standard optical microscopy was used to verify the size of structures. This was also used in some cases to provide information on profile. For example, when a large undercut in a resist for a lift-off is desired, this can be seen in the optical microscope. For the DFB laser gratings fabricated in this work, higher resolution microscopy techniques are required. Scanning electron microscopy (SEM) has been used extensively for this as it is perhaps the only way to verify that a low order grating has been fabricated to the designed specification. A full discussion of SEM technology will not be provided here, however the basic principle is that electrons are emitted from a source focused onto the sample where they interact with it, either backscattering at a high angle and subsequently being detected by a backscatter detector (BSD), or generating secondary electrons which can be detected by a secondary electron detector. Both detection methods have their uses, generally speaking, backscattered electrons provide more information about the materials in the sample as there is a high dependence on atomic number Z , whereas secondary electrons

provide more information about the topography of the sample [70]. Other more exotic detection methods are available but these will not be covered here. For assessing the dimensions of DFB grating structures secondary electron detection was the preferred method. The final technique employed for checks during the fabrication was profilometry. Here a probe is scanned across the surface of a sample to generate height data. The probe itself is attached to a microlever and a laser impinging on the lever measures the change in height. High resolution scans can be performed and so this technique was used extensively to measure the depth of etches, as well as BCB step heights.

4.9 Characterisation

4.9.1 LIV Measurements

Light, current, voltage (LIV) measurements are usually the first step in the laser characterisation process. The first component of this is the LI curve which describes the light output in watts as a function of input current. This curve exhibits two regimes for a working laser. The lower current section of the curve shows a gradual increase in the output power of the laser corresponding to the amplified spontaneous emission (ASE). Once the lasing threshold is reached, a sharp increase in the power output is observed, corresponding to the region of stimulated emission. The point at which this occurs is known as the threshold current. In this work, the threshold current was calculated using the second derivative method which states that the threshold current corresponds to the maximum of the second derivative of power with respect to current. The gradient of the curve in the stimulated emission regime is known as the slope efficiency and was used throughout this work to compare the efficiency across devices. The second component of LIV characterisation is the current voltage or IV curve. This describes the voltage drop across the diode as a function of input current. The point at which voltage begins to stabilise with current is known as the turn on voltage and is typically around 0.7 V for InP-based laser diodes. The IV curve can also provide an indication of how resistive a device is [71]. A schematic of the measurement set up to perform the LIV measurement is shown in 4.10a. The devices, which were mounted onto TO-8 headers, were placed on a thermoelectric cooled (TEC), 3-axis positioning stage and an integrating sphere was positioned close to the devices to measure the output power. Under pulsed current operation, which was used to reduce the effects of self heating, current was supplied with a pulsed generator, which had a pulse frequency of 5 kHz and a pulse length of 1 μ s. The voltage and current supplied were measured using an oscilloscope. For continuous wave (CW) operation, a Keithley 2410 source meter was used, which simultaneously provided current whilst measuring the voltage.

4.9.2 Wavelength Measurements

Wavelength measurements were carried out in order to observe the emission spectra of the devices fabricated in this work. A number of parameters can be extracted from the emission spectra. The first of these is the peak wavelength which corresponds to the wavelength of maximum power output. This parameter is relevant for the DFB laser as assessing its value as a function of temperature is often necessary to confirm whether the observed mode is in fact the DFB lasing mode. Specifically, the DFB lasing mode shift is dependent on the change in refractive index with temperature. For an FP device, the shift in peak wavelength as a function of temperature follows the movement of the gain peak, which is more sensitive to changes in temperature than the refractive index. Values for this depend on the device and material used, however, for a DFB laser a shift of around 0.1 nm K^{-1} would be expected compared to around 0.5 nm K^{-1} for an FP device.

The second parameter that can be extracted from the emission spectrum is the FSR, which is given by equation 2.9. For a DFB laser, the stopband width can be calculated from a sub-threshold emission spectrum. Care must be taken, however, as both facets must be highly AR reflective, as even small facet reflections reduce the accuracy of this measurement [72]. Thirdly, in the case of a DFB laser, the side-mode suppression ratio (SMSR) can be evaluated. This is as the difference in power of the strongest longitudinal mode with the next strongest mode on a decibel scale. High performance DFB lasers for communication applications are required to have SMSR values exceeding 40 dB in order to limit dispersion, as discussed in chapter 1. In this work, the emission spectra were measured by mounting the samples onto a TEC controlled stage, then coupling the light into an optical fibre using a focusing lens. The fibre was connected to a Yokogawa AQ6370D optical spectrum analyser, which was used to record the spectrum. This experimental set up is shown in Figure 4.10b.

4.9.3 Near-Field Imaging

The near-field is defined as the optical field within one Rayleigh length of the laser facet [73]. Imaging it can provide some information on current spreading as well as the mode profile. The current spreading, along with the device cavity length provides an adjusted device area, which can then be used to calculate the

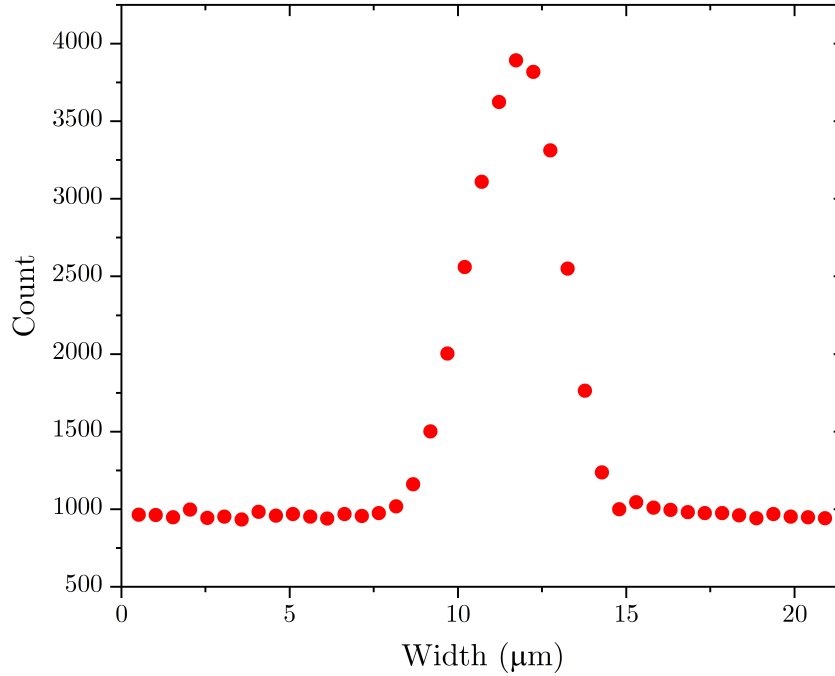


Figure 4.9: An example of a near-field profile from a RWG laser diode. The FWHM can be used to estimate the current spreading for calculating current density.

threshold current density. Typically for RWG laser diodes, the threshold current density is calculated with the area of the RWG. This method, however, does not account for the current spreading, which can be significant in RWG laser diodes. In this work, the nearfield has been measured by focusing the image facet onto an IR camera as shown in Figure 4.10c. The line profile of the image is then extracted, and the current spreading is taken as the FWHM of the line profile. This method is performed at driving current values just below the threshold current as the effects of stimulated emission can result in the underestimation of the current spreading. This methodology has been described and implemented in a number of previous studies [74–76]. An example of a typical near-field profile is shown in Figure 4.9. In this case the ridge width of the device was $2.0\ \mu\text{m}$ and the calculated current spreading value was $3.2\ \mu\text{m}$.

4.9.4 Gain Measurement

Parts of this work required the comparison of gain spectra between different material systems. Two methods exist for calculating the modal gain spectrum of a device through analysis of the ASE spectrum or sub threshold emission spectrum. The first of these is was presented by Basil Hakki and Thomas Paoli in 1975 and as such, is called the Hakki-Paoli (HP) method [77]. Since the intensity of the ASE depends on the wavelength and gain within the laser cavity, the HP method describes the modal optical gain through the equation

$$g(\lambda) = \frac{1}{L} \left(\frac{\sqrt{r(\lambda)} - 1}{\sqrt{r(\lambda)} + 1} \right), \quad (4.1)$$

where $r(\lambda)$ is the ratio between the peaks and the troughs in the ASE and L is the cavity length. The second method was proposed by Daniel Cassidy in 1984 [78]. The so-called Cassidy method proposed an alteration to the HP method by defining the optical gain as

$$g(\lambda) = \frac{1}{L} \ln \left(\frac{p(\lambda) - 1}{p(\lambda) + 1} \right), \quad (4.2)$$

where $p(\lambda)$ refers to the integral over each FP mode divided by the minimum of the mode multiplied by the FSR [10] and

$$p(\lambda) = \frac{\int_{\lambda_1}^{\lambda_2} I(\lambda') d\lambda'}{I_{min}(\lambda)(\lambda_2 - \lambda_1)}, \quad (4.3)$$

where I is the ASE intensity. Both methods provide accurate results for the gain spectrum, however, the Cassidy method is less sensitive to the resolution of the optical spectrum analyser used to obtain the ASE [79]. Therefore, the Cassidy method has been used in this work to calculate modal gain spectra. It is worth mentioning that other techniques exist to evaluate the gain spectrum as well as the absorption spectrum. An example of this is called the segmented contact method [80]. This method is also not limited to sub-threshold measurements, since it is carried out on non-lasing devices. The fabrication of additional segmented contacts on the material are required, however, so this method has not been used

in this work.

4.9.5 Reduced Temperature Measurements

In some cases, devices were required to be measured at temperatures lower than the dew point of water. This was not possible using the TEC, therefore when temperatures lower than 15 °C the devices were mounted into an Oxford Instruments Microstat cryostat system. The system was held at vacuum and liquid nitrogen was supplied for cooling. Other than these details, the systems were the same as shown in Figure 4.10.

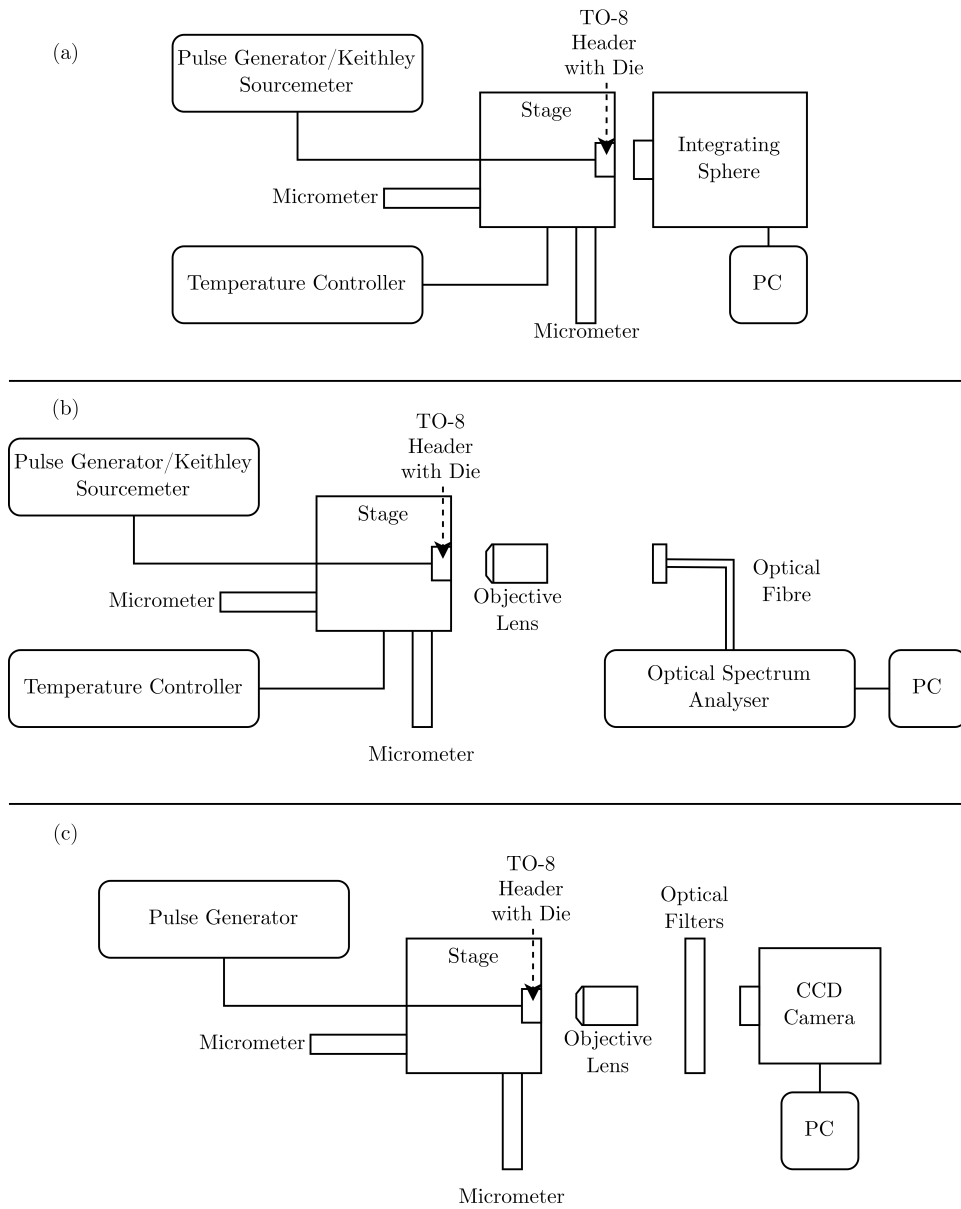


Figure 4.10: Schematics showing the experimental set ups used in this work. (a) light current voltage temperature measurements, (b) spectral measurements and (c) near-field measurements.

4.10 Summary

This chapter has introduced the experimental techniques used to fabricate and measure the devices in this work. The fabrication techniques used were described first, followed by the characterisation techniques used to measure completed devices.

Two types of lithography have been used in this work. The first of these was MOPL, which was used to pattern the grating structures described in chapter 5, as well as p-contacts throughout this work. The second lithography technique was EBL, which was used to pattern the structures described in chapter 6. The system used was a Raith EBPG 5200+ along with the beamer package, which allowed proximity effect corrections to be made. An additional patterning technique used in this work was FIB, which resulted in the work described in chapter 7. The system used was a Raith Velion, which had both a GaBiLi and AuGeSi LMAIS source fitted.

Dry etching techniques such as RIE and ICP-RIE have been used extensively in this work. For the etching of epitaxial structures a Cl_2/Ar chemistry was used and for etching dielectric hard masks, $\text{C}_4\text{F}_8/\text{O}_2$ and SF_6/N_2 chemistries were used. Thermal evaporation was used in the deposition of contact metals and e-beam evaporation was used in the deposition of hard masks. BCB was used as the dielectric in the grating structures presented in this thesis.

Completed devices were mounted onto TO-8 headers and tested. LIV measurements were undertaken to reveal key device figures of merit such as the threshold current and slope efficiency. Spectral measurements were also performed to reveal the wavelength characteristics such as the peak wavelength and the SMSR. This also allowed the calculation of the gain spectrum through the Cassidy method, which has been used to compare the gain spectrum width of devices with quantum well and quantum dot active material. The near-field emission profile of the devices was also analysed to find the level of current spreading as well as giving an indication of the mode profile.

Chapter 5

11th Order C-band DFB lasers Fabricated with Projection Lithography

5.1 Overview

This chapter will discuss the design, fabrication and measurement of 11th order DFB lasers fabricated with projection lithography. This will begin with a discussion of the motivation and aims of this work with reference to previous literature. The modelling and design process for these devices will then be presented, followed by the fabrication and process development that was undertaken to produce the devices. The chapter will conclude by presenting the device results, which will be based on a comparison of the fabricated DFB lasers and reference FP RWG devices.

5.2 Motivation

As discussed in previous chapters, significant work has gone into removing the regrowth process in DFB laser fabrication owing to its significant cost. Whilst high performance LC-DFB devices have been achieved in the literature, the vast

majority still use electron beam lithography for the definition of the grating structure, which represents a significant cost increase in a fabrication run. Other techniques which are more scalable exist and high performance devices have been demonstrated using these techniques. One example is interference lithography, which involves exposing resist with the interference pattern of two lasers. Li et al demonstrated a first order DFB laser using this technique [34]. In this case, three etch processes were used to define the structure, including an oxygen plasma etch to partially remove sections of photoresist. The ashing technique may not be the most repeatable on a larger scale, however it is required due to the fact that interference lithography can only pattern large areas. As a result, the extrusion length of the gratings cannot be controlled easily and therefore, the coupling strength. Furthermore, the use of interference lithography does not allow for the creation of phase shifts or aperiodic gratings. Nano-imprint lithography is another technique that is potentially more scalable than electron beam lithography as it uses a high resolution master to imprint the pattern into the resist. This means that once the master has been created, throughput can be very high compared with electron beam lithography [81]. This method has also been used to create DFB lasers with reasonable performance [82]. In this technology, however, there are a number of challenges that have not been fully addressed. The first of these is the high number of defects introduced by the technique [83]. Secondly, the alignment procedure is challenging compared to optical lithography, as the alignment must be performed while pressing the mold into contact with the resist. The result is potentially less accurate alignment especially when patterning on larger wafers [84]. Pattern distortion is also an issue, which is a variation in the patterned dimensions, which depends on the type of stamp used and its interaction with the resist [85].

I-line (365 nm) mask-less projection photolithography is a well-established technique offering high-throughput as well as providing a low cost of entry unlike high resolution direct write techniques. Moreover, it offers the benefit of rapid prototyping due to no physical mask being required, as is the case in contact lithography. Limited work has been presented using this method for DFB grating structures, due to the fact that the dense features found in gratings limit the achievable resolution even if the tool is theoretically capable of resolving the minimum feature size in the grating. Furthermore, since it is not a direct write technique, therefore dose correction cannot be performed. This means that novel

fabrication process flows are required to achieve LC-DFB structures using this method. The issues described mean that low order gratings are not possible with this method, therefore, higher order gratings must be used to provide the feedback necessary for single mode lasing.

The majority of LC-DFB gratings described in the literature are second and third order. Lasing from devices with these types of gratings was first described in 1972 [86] and the earliest LC-DFB lasers on the GaAs material system used 3rd order gratings [28]. Since then, both second and third order devices have been presented with reasonable performance at both 1550 and 1310 nm wavelengths [37, 87]. DFB lasers with higher order gratings than this, however, are less common particularly in the InP material system, targeting the c-band. Higher grating orders have been presented in the GaAs targeting 980 nm [39] and gallium nitride (GaN) material systems targeting visible wavelengths. Work by Slight et al is an example of this, where SMSR values exceeding 35 dB have been achieved with a 39th order grating DFB laser. This example still required the use of electron beam lithography, however, as a high duty cycle was used to achieve the necessary coupling strength [40]. The fabrication of higher order gratings in the InP material system is worth investigation for a number of reasons. The first of these is the fact that the dimensions simplify the fabrication process considerably. Increasing the order increases the minimum feature size, meaning that lower resolution, high-throughput patterning techniques can be used. Furthermore, increasing the gap size in the grating teeth reduces the aspect ratio of the structures. As a result, dry etching is easier because the effect of aspect ratio dependent etching (ARDE) is reduced [88]. Finally, previous work has indicated that high-order gratings may offer improved SMSR and linewidth even without the use of optical facet coatings [89].

In response to the issues described above, the work included in this chapter aimed to demonstrate DFB lasing in the c-band using a high order grating fabricated with I-line lithography.

5.3 Simulation and Design

The design process began with selection of the appropriate grating order. The selection process was based on the resolution of the lithography equipment used.

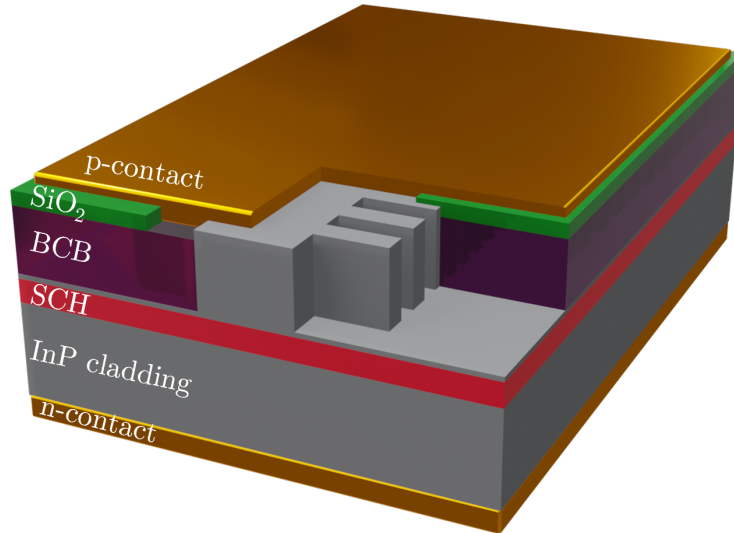


Figure 5.1: Designed device structure for this work. The grating structure of InP is shown in grey, the separate confinement structure is shown in red and the dielectric window layer is shown in green.

A Durham Magneto Optics Microwriter ML3 Pro was chosen due to the fact that it uses a digital mask. This meant that the design could be changed easily during the development process in response to testing exposure dose and duty cycle. A grating order of 11 was chosen for this work, with the required pitch calculated to be $2.6 \mu\text{m}$. This meant the minimum feature size would be $1.3 \mu\text{m}$, assuming a duty cycle of 0.5, which is within the resolution capability of the projection lithography system used. The designed structure is shown in Figure 5.1. Here the central ridge can be seen with the 11th order gratings attached on both sides of the ridge. The structure was low-open area which meant the ridge was placed in an etched trench, such that the etched area was much less than the masked area. The trench was filled with BCB 3022 spin-on dielectric. This provided electrical isolation, optical confinement, as well as forming the lower index part of the refractive index modulation for the grating. A further SiO₂ window was included on the surface. This was done to ensure a portion of the contact was metal on oxide on semiconductor rather than metal directly on BCB which in some cases can collapse under the force of the wirebonder used to affix the wires for testing. The modelling techniques described in chapter 3 were used to design appropriate

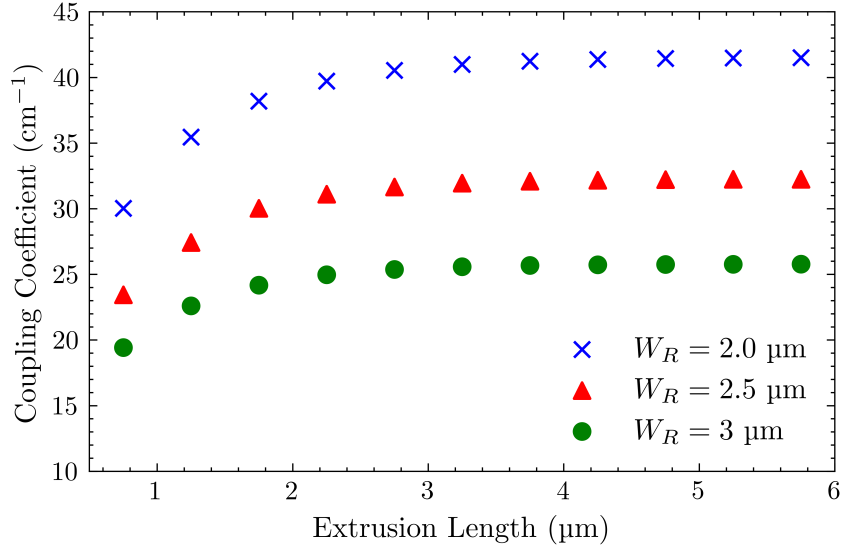


Figure 5.2: Coupling coefficient as a function of extrusion length for the three ridge widths fabricated.

coupling coefficient values for this structure. Figure 5.2 shows the results of this simulation work. The coupling coefficient is shown as a function of extrusion length for variable ridge widths. It can be seen in Figure 5.2 that at higher values, the coupling coefficient does not vary much with changes in the extrusion length. For this reason, the grating extrusion length was designed to be $4.5 \mu\text{m}$, with the ridge width being the variable parameter. The three ridge widths shown in Figure 5.2 were used, which provided a range of coupling coefficient values around the targeted value of $\kappa L = 1.5$ for a $500 \mu\text{m}$ cavity length. Full details of the designed devices are shown in Table 5.1. Standard RWG FP devices were added to verify the existence of DFB laser operation through comparison of their emission spectra.

Table 5.1: Ridge widths, extrusion lengths and designed coupling coefficient values of the devices fabricated in this chapter.

Name	Type	Ridge Width (μm)	Extrusion Length (μm)	Designed κ
G1	DFB	2.0	5.00	41.46
G2	DFB	2.5	4.75	32.22
G3	DFB	3.0	4.50	25.75
R1	FP	2.0	0	0
R2	FP	2.5	0	0
R3	FP	3.0	0	0

5.4 Fabrication

5.4.1 Process Development

The obvious route to fabricate the structure shown in Figure 5.1 would be to pattern the whole ridge and grating together in one step. This would be followed by a dry etch process to transfer the pattern into the epitaxial structure. Figure 5.3 shows a scanning electron micrograph of a LC-DFB grating structure patterned into photoresist. In this case, the interior corners of the grating have significantly rounded and there is large lateral variation of the duty cycle in each section of the grating. Furthermore, the height of the structure varies significantly, which could potentially transfer into the epitaxial material during the dry etch process, due to thinner areas of resist being etched through. These factors would inevitably result in a reduced coupling strength from the grating, compromising the single mode performance of a completed device. The reason these effects happen is that conventional lithography techniques such as projection lithography do not facilitate dose correction, as large areas of the pattern are being exposed at one time. In a direct write lithography system such as EBL, the dose could be reduced in the corners at the interior portion of the grating and increased in the outermost

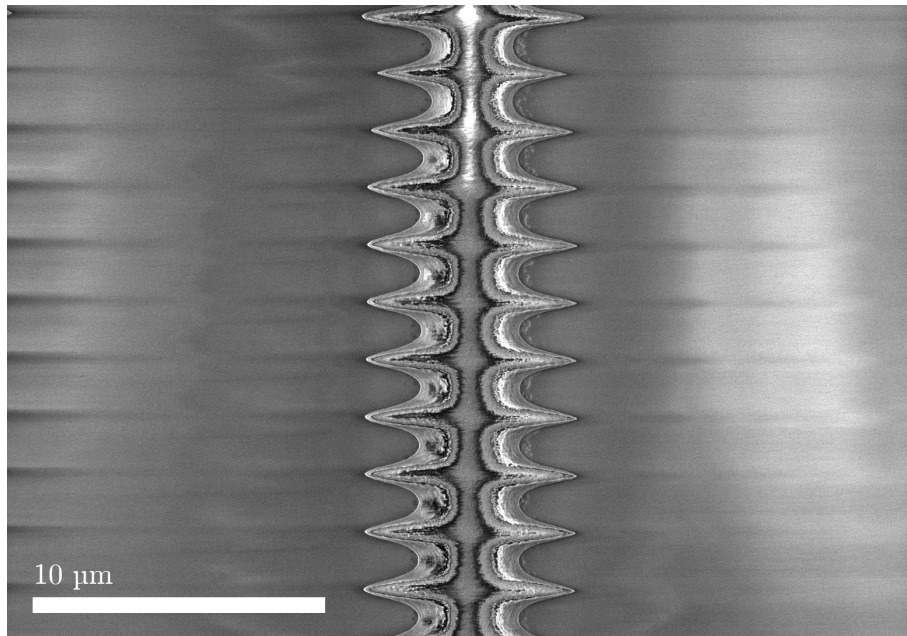


Figure 5.3: Result of attempting to pattern the ridge and grating structure in a single resist exposure in AZ2020 photoresist.

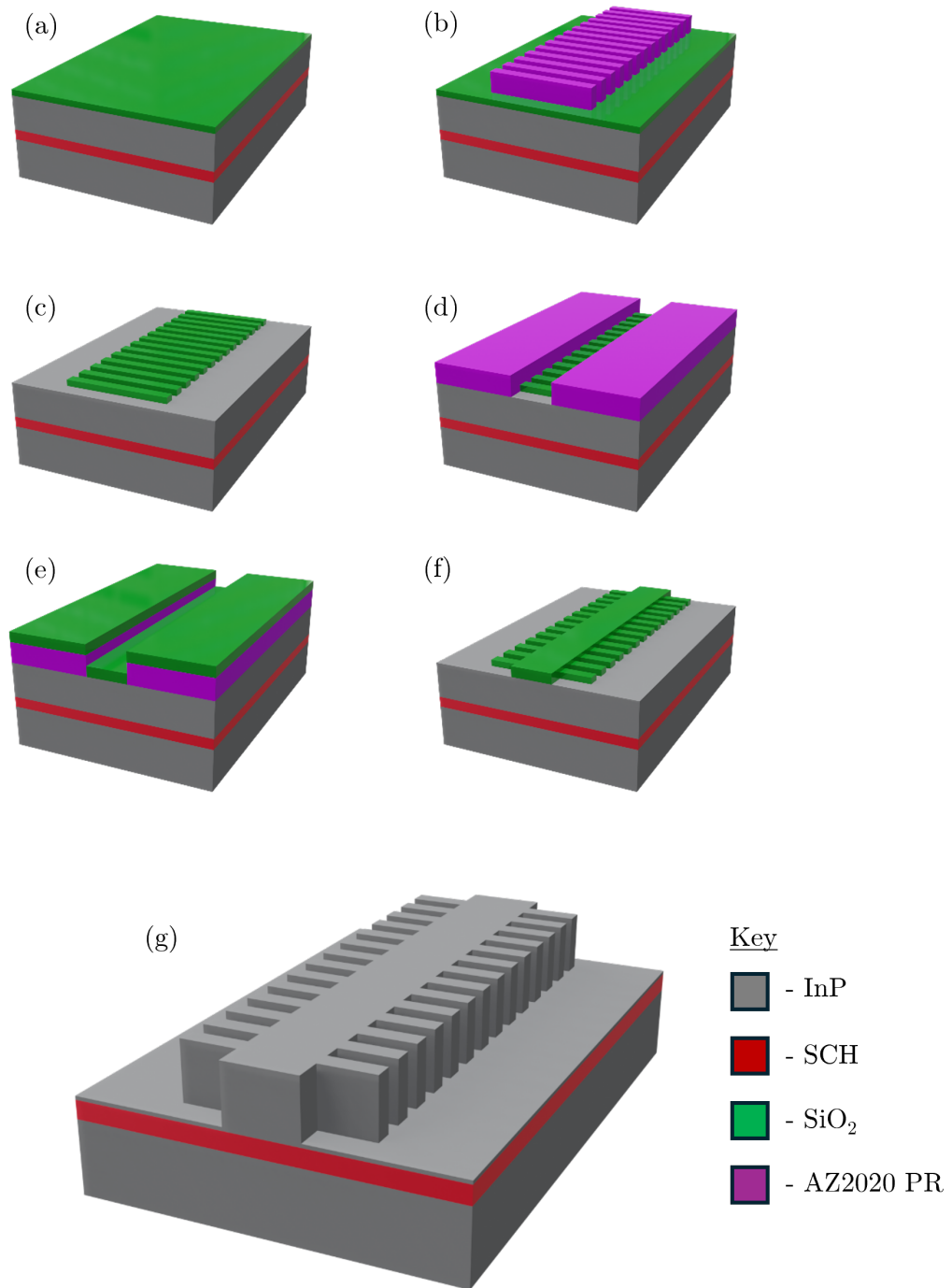


Figure 5.4: (a) Deposition of SiO₂ hard mask. (b) Patterning of grating into AZ2020 photoresist. (c) Etching of grating pattern into oxide hard mask. (d) Patterning of ridge gap in AZ2020 photoresist. (e) Deposition of additional SiO₂ hard mask for the ridge. (f) Completed hard mask including ridge and grating following lift-off procedure. (g) Completion of LC-DFB structure following ICP-RIE.

portions of the grating. This would result in sharper features throughout. The results shown in Figure 5.3 demonstrated the need for a new fabrication process if these structures were to be patterned with a non-direct write method. In order to address these issues, the process shown in Figure 5.4 was developed. This begins with the deposition of a 300 nm SiO₂ hard mask using e-beam deposition (Figure 5.4a). SiO₂ was chosen for its high selectivity in the Cl based chemistries used to etch InP. This is followed by a lithography process where 12 μm gratings are patterned into the negative-tone photoresist AZ2020. This resist was chosen due to its high resistance in ICP-RIE dry etching. The resist was spun such that it was approximately 1.3 μm thick. The resulting grating structure from this lithography step is shown in Figure 5.4b. This resist was then used as a mask to transfer the gratings into the oxide hard mask using ICP-RIE (Figure 5.4c). The addition of the central ridge portion of the mask was then made using a lift-off process. The gap for the ridge was patterned again into AZ2020 resist, as is shown in Figure 5.4d. This was then followed by the deposition of 500 nm of additional SiO₂ (Figure 5.4e). Following the lift-off procedure in NMP 1165 resist remover, only the completed mask remained, shown in Figure 5.4f. This was then used as an etch mask during the Cl₂/Ar ICP-RIE to transfer the structure into the epitaxial material, leaving the completed LC-DFB structure (Figure 5.4g). Following this process, BCB was spun onto the sample to provide electrical isolation and form the low-index part of the grating. This was followed by lithography, deposition and lift off to form the Ti/Pt/Au (10/20/500 nm) p-type top contact. The sample was then thinned to 120 μm and an n-type AuGe/Ni/Au (100/28/300 nm) bottom contact was deposited using thermal deposition. The contacts were then annealed together at 350 °C for 5 mins. Finally, the devices were prepared for measurement by cleaving into bars, mounting onto TO8 headers and bonded with 30 μm gold wire. A detailed process flow can be found in Appendix A.1.

5.4.2 Fabrication Results

Images showing various stages of the fabrication process are shown in Figure 5.5. In Figure 5.5a, an image from an optical microscope following the patterning of the 11th order grating is shown. A line profile was created of 5 periods of the grating, following which, the pitch was found to be (2.58 ± 0.01) μm. The gap between grating teeth was measured to be (0.62 ± 0.06) μm, corresponding to a duty cycle of 0.76. During the optical imaging process however, significant

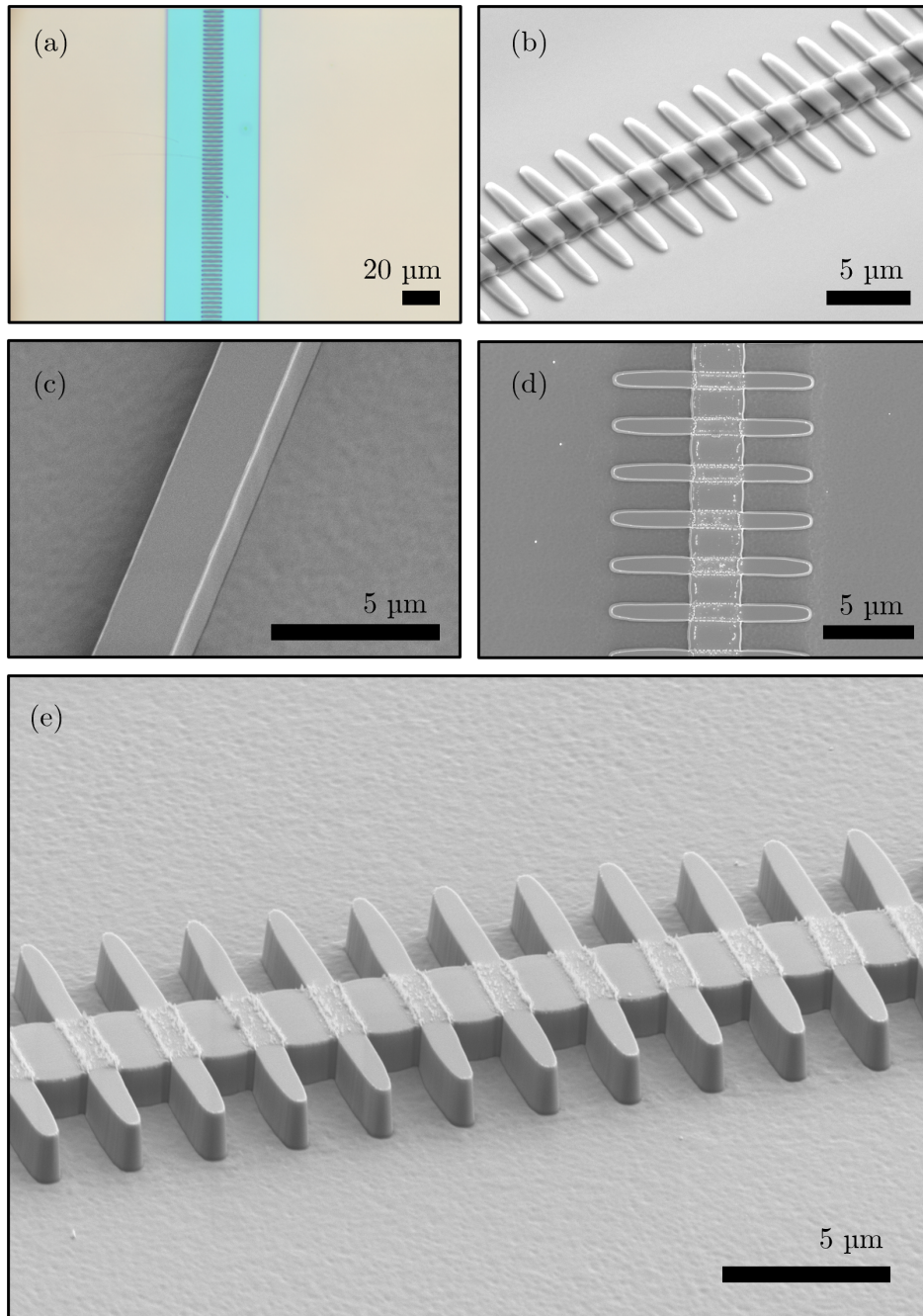


Figure 5.5: (a) Optical micrograph of the grating structure patterned in AZ2020 photoresist. (b) Scanning electron micrograph of the completed SiO_2 hard mask following lift-off procedure. (c) Scanning electron micrograph of a RWG FP control device. (d) Top down scanning electron micrograph of a G1 DFB device following ICP-RIE. (e) G1 DFB device imaged on a 45° tilt.

variation was observed in the duty cycle across the sample. This can be attributed to variation in the depth at which the light from the projection lithography system is focused in the resist. The projection lithography system uses a series of focus points distributed across the sample to determine the focus point of the resist, which is pre-calculated before writing begins. Between the focus points, the system uses a surface tracking laser system to determine the focus position during the write. The real-time laser tracking system is less accurate than the focus points which may result in differences in focus points across the sample. The resulting change in the light profile causes the dose at the edges of each grating tooth to vary resulting in a size variation across the sample. Figure 5.5b shows the completed SiO₂ hard mask following the lift off procedure used to define the ridge. The image demonstrates the sharp interior corners achievable using this method, however broadening of the ridge width was observed following this step in the process. Specifically, the ridge width of a G1 device designed at 2 μm was measured to be (2.59 ± 0.05) μm. This broadening can be attributed to the oxide deposition process and lift-off procedure. In particular, the lift-off method necessitates an undercut profile to ensure that the resist remover can access the resist to remove it. Furthermore, the hard mask was deposited using an e-beam deposition system with a rotating, angled substrate holder. Since this deposition method is a line-of-sight method it is likely that the angled nature of the substrate holder allowed oxide to be deposited over the wider area at the bottom of the resist introduced by the undercut profile. This was not observed for the RWG control devices as these ridges were patterned alongside the gratings in the first lithography step meaning a lift-off procedure was not used. For example a measured R1 device, which was designed to have a ridge width of 2 μm, was found to be (2.06 ± 0.12) μm in the oxide mask. An example RWG FP device, following the etch into the epitaxial structure and mask removal is shown in Figure 5.5c. The profile was observed to be as designed, with vertical sidewalls achieved. A top-down image of the G1 11th order DFB structure imaged using SEM, is shown in Figure 5.5d and the same structure imaged with a 45° tilt is shown in 5.5e. Qualitatively, success of the lift-off process was observed, as sharp corners at the interface between the grating regions and ridge were achieved. Some debris is also visible on the top surface of the structure. This was believed to be polymer build-up from the dry etch process used to remove the hard mask [90], as this was not visible in future runs where hydrofluoric acid was used to remove the mask. Using

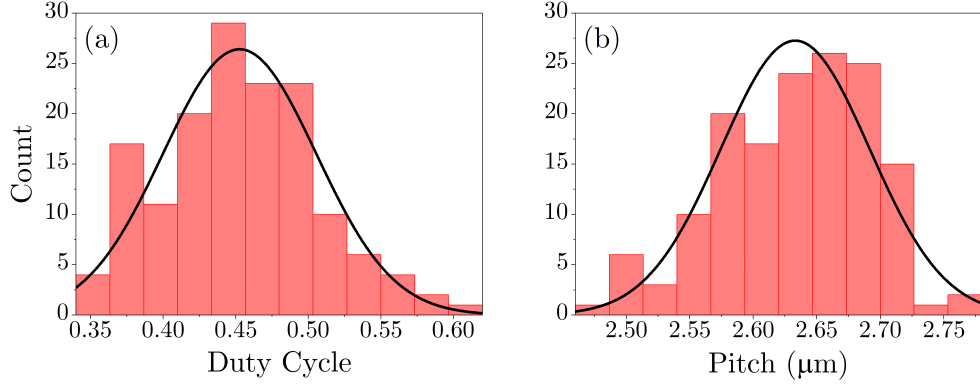


Figure 5.6: Histograms describing the measurement of (a) duty cycle and (b) pitch for G1 DFB devices across a 15x15 mm sample.

Table 5.2: Variability of key parameters on G1 DFB devices across a 15x15 mm sample.

Parameter	Designed Value	Mean Value	Standard Deviation
Ridge Width (μm)	2	3.37	0.23
Grating Pitch (μm)	2.6	2.633	0.059
Duty Cycle	0.5	0.452	0.053

the tilted image, the etch depth was measured to be $(1.493 \pm 0.018) \mu\text{m}$ with a sidewall angle of $(6.08 \pm 0.12)^\circ$. Once again, a line profile was made of the grating region, from which the pitch and duty cycle could be extracted. For the section of grating shown in Figure 5.5d, the pitch was found to be $(2.678 \pm 0.008) \mu\text{m}$ and the grating gap size was found to be $(1.791 \pm 0.021) \mu\text{m}$ which corresponded to a duty cycle of 0.33. Discrepancy in the measurement of both duty cycle and pitch at different points of the sample indicated some variability in these values. In order to quantify this, 50 top-down images of G1 devices were taken at different points across the sample using SEM. In each image, the ridge width, pitch and duty cycle were measured at 4 points giving a sample size of 200. Histograms showing the results of the measurements for pitch and duty cycle are shown in Figure 5.6, with the data extracted from these measurements shown in Table 5.2.

The data shown in Figure 5.6 and table 5.2 highlights that significant broadening of the ridge is present in the final devices. Specifically, the mean ridge width across the sample was found to be $3.37 \mu\text{m}$, over $1 \mu\text{m}$ larger than the designed value of $2 \mu\text{m}$ for the G1 DFB devices. This has been discussed previously in

this section and is attributed to broadening of the hard mask during the deposition and lift-off process. Furthermore, broadening of the ridge to this degree guarantees that the RWG will facilitate multiple lateral modes, which must be considered in the analysis of any results. The mean value for the grating pitch was found to be $2.633\ \mu\text{m}$ with a standard deviation of $0.059\ \mu\text{m}$. Since the Bragg wavelength shifts by approximately $5\ \text{nm}$ for every $10\ \text{nm}$ shift in the grating pitch, a wavelength range of $25\ \text{nm}$ corresponds to one standard deviation from the mean pitch value. Improving the variation in the grating pitch, would be possible through the use of a lithography system with a more accurate laser interferometer stage. Similar variation in the duty cycle was observed and is shown in Figure 5.6a and Table 5.2. A mean duty cycle value of 0.452 was found, with a standard deviation of 0.053 . In one standard deviation therefore, the duty cycle varies from approximately 0.4 to 0.5 . Such a variation has implications for the coupling strength of the gratings. This has been discussed in chapter 3, and the simulation work described there has been used to estimate the range of coupling strengths based on the fabrication results presented here. The result of this is shown in Figure 5.7. As previously mentioned, the broadening of the RWG portion of the DFB devices forces consideration of higher order lateral modes. Therefore, the coupling coefficient as a function of duty cycle is shown for both

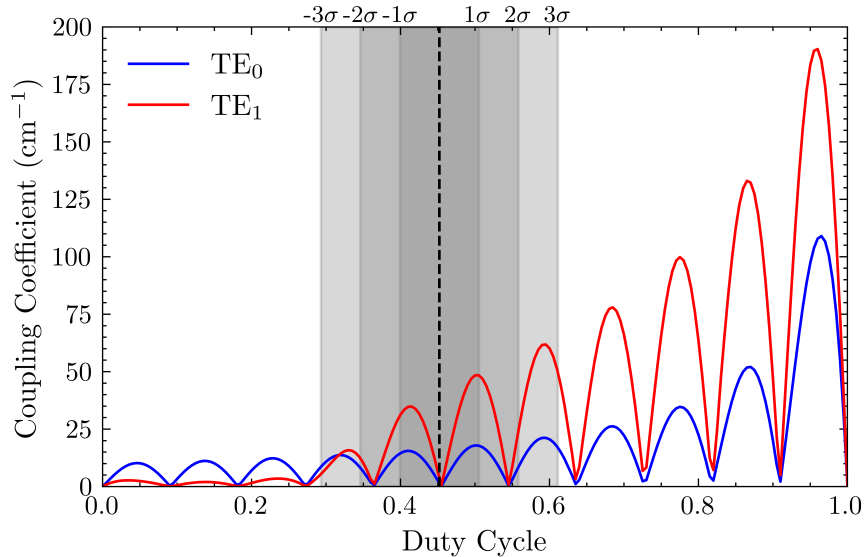


Figure 5.7: Coupling coefficient for the average grating fabricated in this work as a function of duty cycle for both the fundamental TE mode and 2nd order TE mode. Shaded areas show the standard deviation values in duty cycle.

the TE_{00} mode, and the TE_{10} mode. From Figure 5.7, it can be seen that the mean value of the duty cycle falls almost directly at a point in which the coupling strength decays to zero. Additionally, two more minima occur within two standard deviations of the mean. Due to the variation in duty cycle, a high degree of variability in the coupling coefficient is likely, which would potentially reduce the single mode yield of these devices. This would also depend on whether the duty cycle varies across the length of a single device or whether it is a longer range variation across the sample itself. Figure 5.5 also indicates that across the range of duty cycles fabricated here, the TE_{10} mode exhibits a higher coupling strength than the fundamental TE_{00} mode. This means the TE_{10} mode likely has a lower threshold gain than the fundamental mode, causing lasing in the higher order lateral mode or even mode competition and, therefore, wavelength instability. The device results discussed in the following sections will investigate this further.

5.5 Device Results

This section will describe the characterisation undertaken on the devices fabricated in this work. The main focus is on a comparison of the 11th order DFB structures with the FP RWG control devices. Of the fabricated devices shown in Table 5.1, only G1 devices exhibited single mode lasing, which was likely due to reduced coupling coefficient resulting from the broadened ridge width. As such, only G1 DFB devices will be considered in the following sections.

5.5.1 Room Temperature LIV Results

This section will begin with a discussion of the characterisation results found under pulsed current operation. All of the results described here were performed using a pulse width of 1 μ s and a frequency of 5 kHz. Figure 5.8 shows the LIV results at room temperature under pulsed current conditions for a 700 μ m device and a FP RWG control device of the same cavity length. 5.8a shows the LIV results for the R3 device. The threshold current was found to be 51.56 mA with a dual facet slope efficiency of 0.2 A/W. For the G1 DFB device, the threshold current was found to be 87.52 mA with a dual facet slope efficiency of 0.06 A/W. Since the pumped area was different in the two devices, nearfield measurements were taken of the two devices to determine the current spreading and calculate the current density values in the devices. The FWHM of the near-fields were found to be 7.44 μ m and 7.73 μ m for the R3 FP device and the G1 DFB device, respectively. The threshold current density was found to be 0.99 kA/cm² and

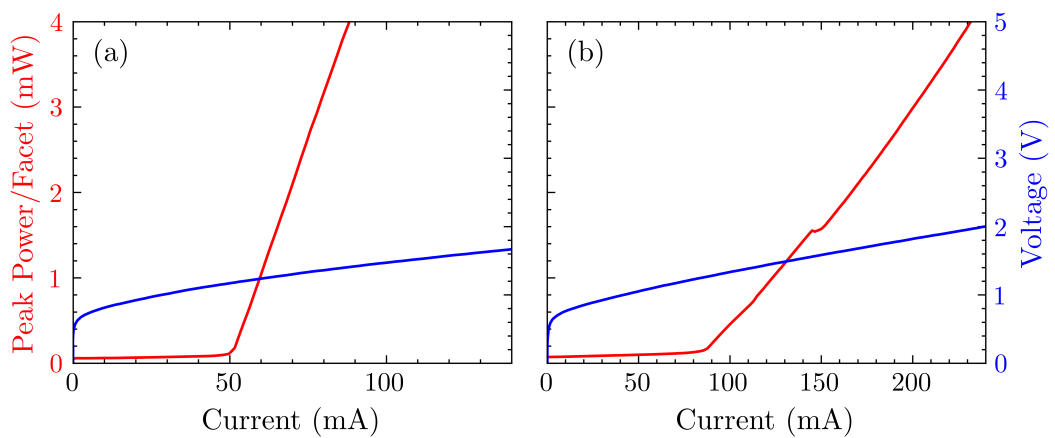


Figure 5.8: LIV characteristics of the (a) R3 FP device and (b) G1 DFB device.

1.62 kA/cm² for the FP device and DFB device, respectively. These results show both an increased threshold current density and reduced slope efficiency in the DFB device. This could be attributed to a number of factors including the increased surface area of the grating structure introducing more loss in the device due to surface recombination, particularly if the BCB has receded from the surface of the structure. Mis-alignment of the gain peak wavelength with the designed wavelength of the DFB grating may also contribute to an increased threshold current. Furthermore, higher order gratings are known to introduce diffraction losses, which may also decrease the efficiency of the device compared to a FP RWG laser [45]. Furthermore, current loss through the outer portions of the grating teeth may also contribute to a reduction in efficiency compared to the FP device. Future designs which do not electrically pump the whole DFB structure could be implemented to remedy this. Figure 5.8b also shows a power fluctuation for the DFB device at around 145 mA. Such an interruption in the normal increase in power during stimulated emission was determined to most likely be the result of a mode hop. This phenomenon will be discussed later in this section.

5.5.2 Room Temperature Wavelength Results

The emission spectra were also examined under pulsed current at room temperature using an optical spectrum analyser. Shown in Figure 5.9a is the emission spectra on a normalised linear scale for both the G1 DFB device and the FP control device. For the control device a peak wavelength of 1568.4 nm was found with multiple modes present at an average spacing of (0.46 ± 0.05) nm, which agrees with the value of 0.51 nm calculated using equation 2.9. The DFB device was found to have a peak wavelength of 1549.6 nm, with a clear single mode present on the linear scale. The difference between the DFB and control device confirms the existence of feedback from the 11th order laterally coupled grating structure. Furthermore, the detuning in the emission wavelength of the DFB with the FP device implies that the DFB lasing wavelength is detuned significantly from the gain peak, potentially contributing to the higher threshold current observed in the DFB device. The emission spectrum from the DFB device is visualised on a log scale in Figure 5.9b. Single-mode emission was observed under these conditions with a SMSR of 25 dB. The observed SMSR is less than has been reported in the literature previously, where 1st and 3rd order gratings have been used.

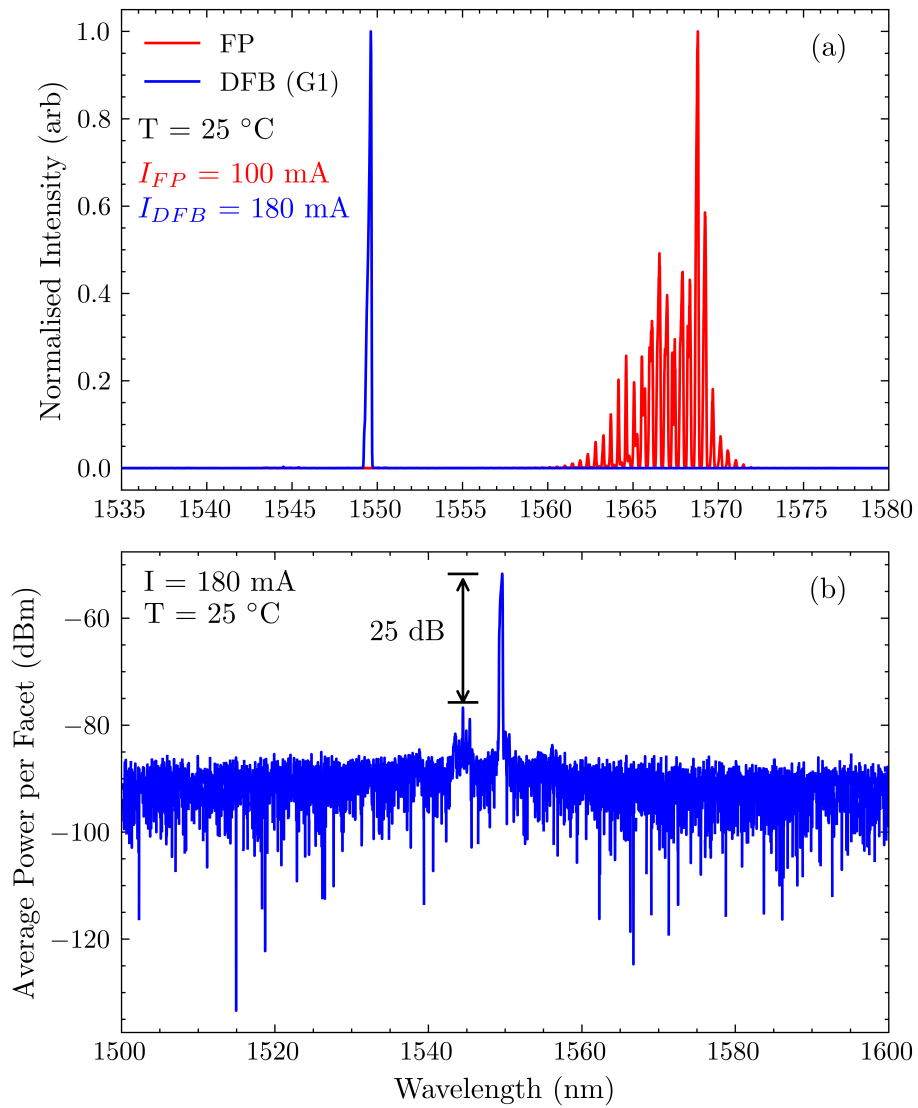


Figure 5.9: (a) Emission spectra of the G1 DFB device and the R3 FP device at room temperature. (b) Emission spectra of the G1 DFB device shown on a log scale, with SMSR indicated.

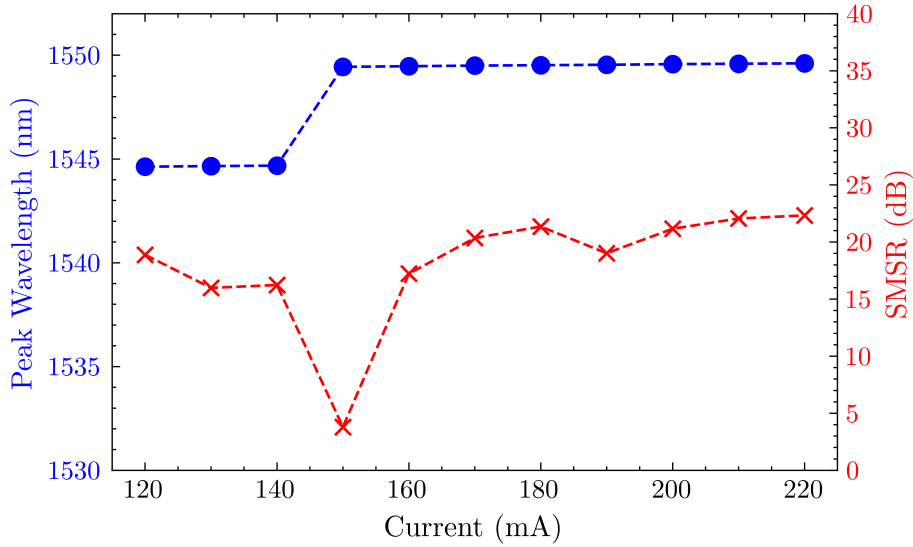


Figure 5.10: Peak wavelength and SMSR as a function of current at a temperature of 25 °C for the G1 DFB device.

For example, Li et al in 2017 reported a 1st order laterally coupled grating fabricated with interference lithography which exhibited an SMSR of 37 dB. Another example is work by Virtanen and colleagues which presented 3rd order gratings fabricated using nanoimprint lithography in the GaAs material system. This work demonstrated an SMSR value exceeding 50 dB, although in this case anti reflective coatings were used to suppress the FP cavity modes. The SMSR achieved in this work compares better to higher order grating DBR lasers reported in the literature. For example, Fricke et al reported a DBR laser with 7th order gratings also fabricated with I-line lithography. In this case an SMSR value of 30 dB was achieved. Although the value achieved in this work is less than the previous examples discussed, the spectral purity could be readily improved through the implementation of a facet coating scheme to remove the influence of the FP modes. Furthermore, the SMSR in this case was limited by the presence of a secondary mode. The secondary mode was observed at a wavelength of 1544.5 nm, which gave a spacing between the two highest power modes of 5.1 nm. The spacing of these modes indicates that multiple lateral modes are competing in the waveguide. In order to verify this, the simulation methods described in chapter 3 were used to calculate the effective index of the fundamental TE₀₀ mode and the TE₁₀ mode. These were found to be (3.271 ± 0.001) and (3.261 ± 0.002) respectively, using the measured values obtained during the fabrication (Table 6.3). Assuming

a constant grating pitch, inserting these values into equation 3.1 provides a difference in wavelength of (4.7 ± 0.8) nm, suggesting that the two observed peaks corresponded to two competing lateral modes. The second mode in this case is at a reduced wavelength due to the fact that it has a lower effective index. The competition between these modes is also observed in Figure 5.10, which shows the peak wavelength and SMSR of the DFB device as a function of pulsed current. Here a shift from the lower wavelength to the higher wavelength mode is observed at 150 mA which corresponds to the fluctuation in output power observed for in Figure 5.8b. Excluding the mode hop, the peak wavelength shifts with current at a rate of 2.4 pm/mA. At the point of the mode hop, the SMSR is also found to decay significantly, as the two modes are present. The mode competition observed here is likely the result of the broadening of the RWG discussed in the previous section of this chapter. Increasing the ridge width in this way allows multiple lateral modes to be bound in the waveguide. It appears in this case that the TE_{10} mode is selected predominantly over the fundamental TE_{00} mode as it has a higher coupling strength, as shown in Figure 5.7.

5.5.3 LIV results with Varying Temperature

The effect of changing ambient temperature has been measured by placing the devices on a TEC stage and altering the stage temperature. The LI curves have been measured for a temperature range from 20 °C to 50 °C. The results of this are shown in Figure 5.11a and b, which show the LI curves at varying temperatures for

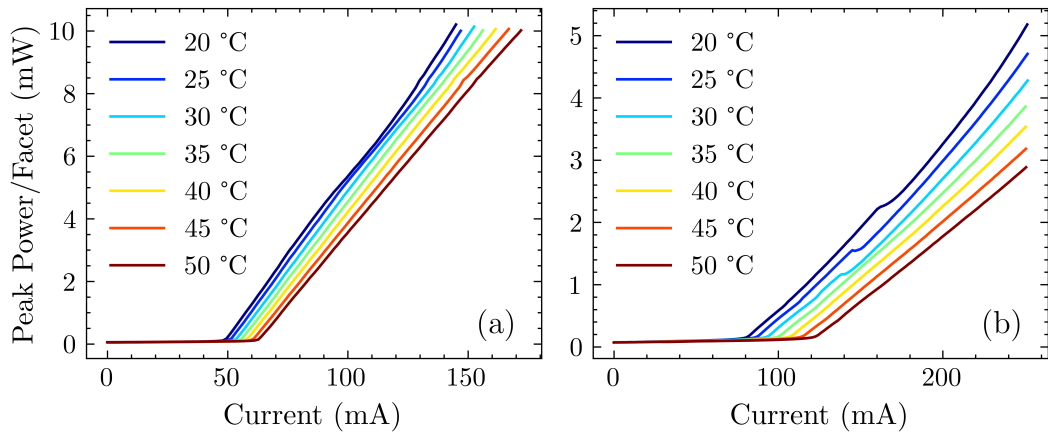


Figure 5.11: LIV curves under pulsed current operation at varying temperatures for the (a) R3 FP device and (b) G1 DFB device.

the FP control device and a DFB G1 device, respectively. Visually, the LI curves indicate an increased threshold current dependence for the DFB device compared to the FP device. Moreover, while the mode hop is visible as a fluctuation in power output from 20 °C to 35 °C, above this range no fluctuation in power is visible. This may indicate that the wavelength is more stable at higher temperatures and later sections of this chapter will discuss this possibility. Various key parameters extracted from these LI curves are presented as a function of temperature in Figure 5.12. Figure 5.12a and b show the threshold current and threshold current density as a function of temperature, respectively. A threshold current shift of 0.4 mA/K was observed for the FP control device and a shift of 1.4 mA/K for the DFB device. These values corresponded to a threshold current density shift with temperature of 0.008 kA/cm² and 0.025 kA/cm². These values confirm the increased sensitivity of threshold current with changing temperature present in the DFB device. The natural log of threshold current density as a function of temperature is shown in Figure 5.2c, from which the T_0 value can be calculated. This analysis provided a value of 126 °C for the FP control device and a value of 73 °C for the DFB device. The value of T_0 being significantly lower for the DFB when compared to the FP control is most likely a result of a detuning between the designed wavelength of the DFB laser and the wavelength at the gain peak of the active material. Since the gain peak varies with temperature at a higher rate than the refractive indices in the grating region, increasing the temperature in this case pushes the DFB further away from the gain peak. As a result, the device has to be driven harder to overcome the losses and reach threshold current and a higher T_0 value is observed. This suggests that a compromise must be made in achieving the increased spectral purity offered by the grating structure. That is, increased threshold current and sensitivity to temperature change, along with reduced slope efficiency.

5.5.4 Wavelength results with Varying Temperature

The wavelength response to varying temperatures under pulsed current operation has also been examined. Figure 5.13a and b show the emission spectra at stage temperatures varying from 20 °C to 50 °C for the FP control device and DFB device, respectively. For the FP device, a shift in the wavelength consistent with that expected as a result of the gain peak shifting with temperature is observed. This is not the case for the DFB laser, which exhibits a reduced

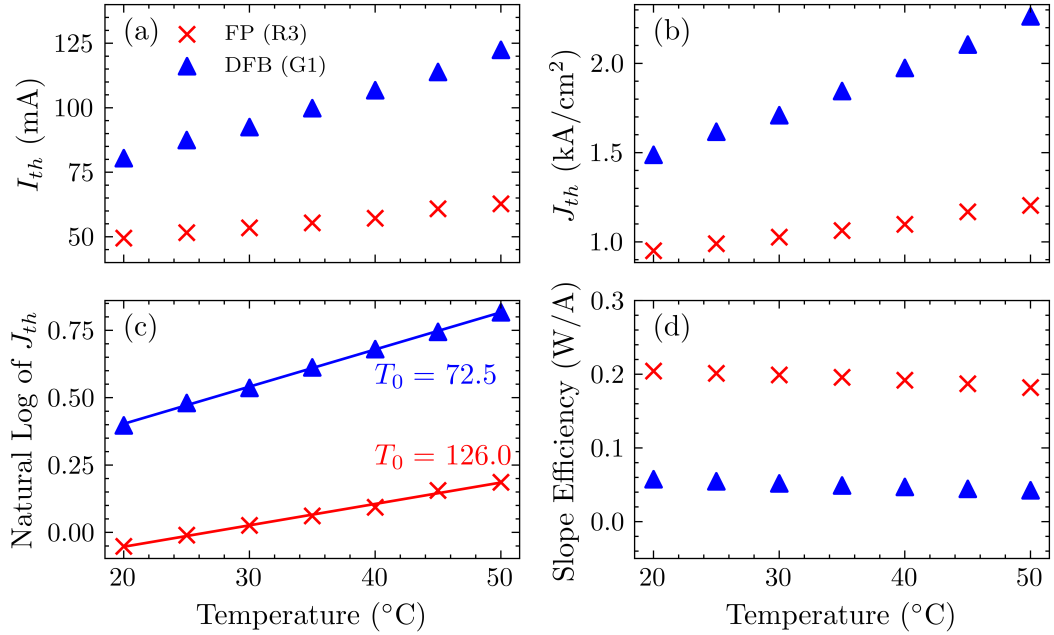


Figure 5.12: (a) Threshold current, (b) threshold current density, (c) natural log of threshold current density and (d) slope efficiency as a function of temperature for the R3 FP and G1 DFB device.

wavelength sensitivity to temperature between 20 °C and 30 °C at which point the device exhibits a mode hop to a higher wavelength where it is again less sensitive to varying temperature. The wavelength shifts for both devices are quantified in Figure 5.13c. For the FP device, a shift of 18 nm was observed across the measured temperature range, this corresponded to a rate of 0.6 nm K⁻¹. For the DFB laser, the device exhibits a wavelength shift of 0.1 nm K⁻¹ both before and after the mode hop. The shift with changing temperature with changing modes is significantly reduced compared to the FP device. This indicates that the shift is the result of the change in refractive index rather than the shift in the gain peak as is the case for the FP device. At lower temperatures, the device favours the lower wavelength of the two modes. This is likely the 1st order TE mode, which has a higher coupling strength than the fundamental TE mode, as shown in Figure 5.7. As the temperature increases, so does the wavelength of the gain peak. The mode hop occurs when the gain at the 1st order TE mode becomes reduced such that the threshold condition of the fundamental TE mode is lower despite the coupling strength being lower. The mode competition observed in these devices can be attributed to the broadening of the ridge width resulting from the lift-off process, as has been discussed earlier in this chapter.

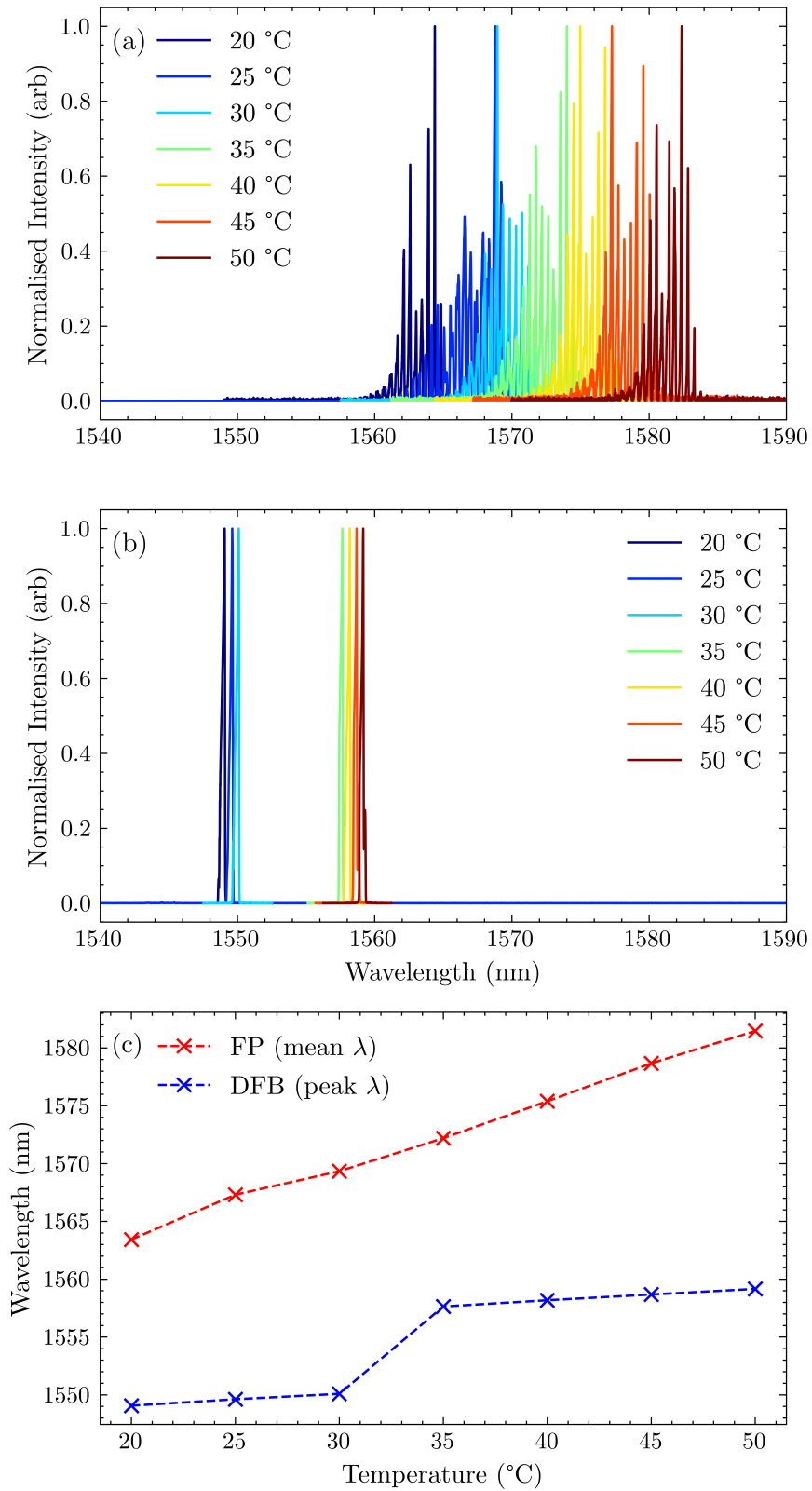


Figure 5.13: Normalised emission spectra as a function of temperature for both the (a) R3 FP and (b) G1 DFB device. (c) Average wavelength as a function of temperature for both devices.

5.6 Summary

This chapter has demonstrated DFB lasing in a device with an 11th order grating fabricated using projection lithography. A two-step lithography and deposition process has been used to define the grating, in absence of the ability to perform dose correction to achieve sharp interior features. The results of this process development have been presented here and significant variability in both pitch and duty cycle were observed. This was attributed to variation in focusing of the projection lithography system. This resulted in a varying dose at the edge of the grating features, causing the duty cycle to vary across the sample. The lift-off procedure was also found to increase the ridge width following deposition of the mask. This phenomenon was attributed to the lift-off procedure used to create the ridge. It was suggested that the use of an angled substrate holder during the deposition of the second hard mask facilitated a wider than designed ridge due to the undercut profile of the photoresist.

Device results were then presented for both a DFB device and a RWG FP control device under pulsed current operation. Increased threshold current density as well as reduced slope efficiency were observed for the DFB device compared to the FP control. This suggested an increased loss in the DFB device which may have been a result of the diffraction loss introduced by the high-order grating structure. Emission spectra of the two devices at room temperature confirmed DFB laser operation for the high order grating structure with a SMSR of 25 dB at a wavelength of 1549.6 nm. Temperature dependent LIV results indicated T_0 values of 125 °C and 76 °C for the FP and DFB devices respectively. The reduced T_0 value found in the DFB device was thought to be due to the designed DFB lasing wavelength being offset from the gain peak. Finally, the spectral performance of the devices were examined as a function of current and temperature. The DFB laser was found to exhibit wavelength shifts with temperature on the order of 0.1 nm K⁻¹, which corresponded to the shift of refractive index with temperature, while the FP device exhibited shifts of 0.6 nm K⁻¹. Examination of the spectral performance also highlighted the mode competition present in the DFB device and mode hops were exhibited as a result of both current and temperature variation. The hopping behaviour present here was likely a result of the widened RWG caused during the lift-off procedure when depositing the mask, the length of the grating teeth may also have contributed to this effect. Future work should

aim to focus the design work on achieving single lateral mode lasing. This may be achieved by using a narrower ridge portion and/or reducing the extrusion length of the grating teeth.

Chapter 6

Grating Order Effects on LC-DFB Lasers using QD and QW Material

6.1 Introduction

This chapter discusses the design, fabrication and measurement of LC-DFB lasers fabricated on both a state-of-the-art commercially grown quantum well epitaxial structure as well as a more specialised quantum dot laser structure grown using MOCVD. The aims of this work were firstly to compare the fabrication and performance of low order (1st and 3rd) gratings with higher order (11th order) gratings similar to those presented in the previous chapter. Secondly, this work aimed to compare the range of accessible wavelengths on the two material systems, as QD material systems may offer wider gain spectra due to inhomogeneous size broadening, the advantages of which are described in the next section. The chapter will cover the motivation behind this work, the design and fabrication of the devices and finally, the performance of the fabricated lasers.

6.2 Motivation

6.2.1 Affects of Varying Grating Order

As discussed in the previous chapter, DFB lasers with grating orders higher than three, are rarely reported in the literature. This is despite the fact that increasing the grating size allows these devices to be fabricated with lower resolution, higher throughput techniques, as well as reducing the effects of aspect ratio dependent etching. In a 1st order grating, single-mode operation is encouraged through the addition of a quarter wavelength phaseshift or the application of facet coatings. Another method of mode selection is the use of radiation loss. This was described theoretically in some of the earliest work on DFB lasers [21, 91]. The mode selection mechanism works on the basis that the two DFB lasing modes have significantly different threshold gain values due to radiation modes. The radiation modes are phaseshifted differently for each of the modes either side of the grating stopband, resulting in an asymmetrical threshold gain [92]. The early work describing these effects noted that the effect increases with grating order, potentially meaning that higher grating orders could achieve better mode selection and therefore higher SMSR. Later work by Millet et al modelled these effects for LC-DFB lasers, suggesting that the mode selectivity effects observed for higher order gratings are dependent on the degree of complex coupling present in the device and thus are dependent on the duty cycle [45]. Other than the design work described, little work has been done to compare the performance of varying grating orders in the InP material system. This work aims to compare a series of grating orders 1st, 3rd and 11th, assessing the difference in performance and reveal whether significantly better single-mode performance may be achieved from higher order gratings.

6.2.2 1550 nm Quantum Dot Lasers

In recent years, lasers fabricated on self-assembled quantum dot material have attracted significant interest due to their many potential advantages. These include reduced threshold current density with lower temperature dependence and less sensitivity to optical feedback as well as high defect tolerance when growing on non-native substrates [93]. In principle, QD material would have a limited range of accessible wavelengths due to three-dimensional confinement. It is well

known however, that dots grown using the Stranski-Krastanov method have an inhomogeneous dot size distribution and as such the gain spectrum is broadened [94]. For a DFB laser specifically, this represents a potential advantage as there may be a wider range of accessible wavelengths or potential for a wider temperature operating range, since the gain spectrum can shift over a larger range before the detuning is too high to enable lasing at the Bragg wavelength. Furthermore, a WDM system using the QD material may be able to have more channels than one based on QWs, with improved stability. Lasers based on InAs/GaAs QDs targeting the wavelengths in the o-band are well established and these devices have now reached the point of outperforming even the best QW devices in terms of threshold current density for example [93, 95]. This is attributed to significant advances in growth techniques. As a result of this, a number of DFB lasers based on InAs/GaAs QD material system have been presented, including LC-DFBs [96, 97]. Similar devices targeting the c-band on InP substrates, however, are far less common. The quantum dots themselves are usually islands of InAs, which are self-assembled on a layer of InGaAs, InAlGaAs or GaAs. The size and therefore the optical properties of the dots are heavily dependent on growth conditions, surrounding material as well as substrate orientation. For this reason, the shape of these can be rather unstable, often leading to more dash-like structures rather than dots [98]. Additionally, many of the lasers presented on these materials are grown by molecular beam epitaxy, which is slow, expensive and often involves significant down time between growth runs. It is therefore, not suitable for scalable manufacturing. Growing quantum dots using MOCVD is more desirable, and is already the standard for QW epitaxial structures and is widely used in industry. Compared to MBE growth however, MOCVD is challenging for QDs, partly because the temperatures are relatively higher which introduces intermixing in the dots during the growth of the capping layer. This typically results in a blueshift in the emission wavelength, which means that high performance QD lasers grown by MOCVD for the c-band wavelength range are rather uncommon [99].

6.3 Design

6.3.1 Material Structure

Two epitaxial materials were used in this work. Both structures were grown on InP substrates. The first structure contained a MQW active region and was grown by Compound Semiconductor Centre Ltd using MOCVD. This structure is shown in Figure 6.1a. On top of the InP substrate, a 1.5 μm lower cladding layer of n-doped InP was grown. This was followed by a separate confinement heterostructure consisting of 9 QWs with a width of 6 nm surrounded by two InAlGaAs layers. Above the SCH, an upper cladding layer of p-doped InP was grown, with a highly doped p-type InGaAs contact layer added on top to facilitate current flow. The second structure (Figure 6.1b) included QD containing active region and followed a similar structure to the QW-based material. The epitaxial structure was grown on an n-type InP substrate. The lower cladding of n-doped InP was 1.1 μm thick. This was followed by the SCH which included 7 layers of unintentionally doped InAs/InAlGaAs dots surrounded by two InAlGaAs layers. The upper cladding was p-doped InP with a 140 nm highly doped p-type contact layer.

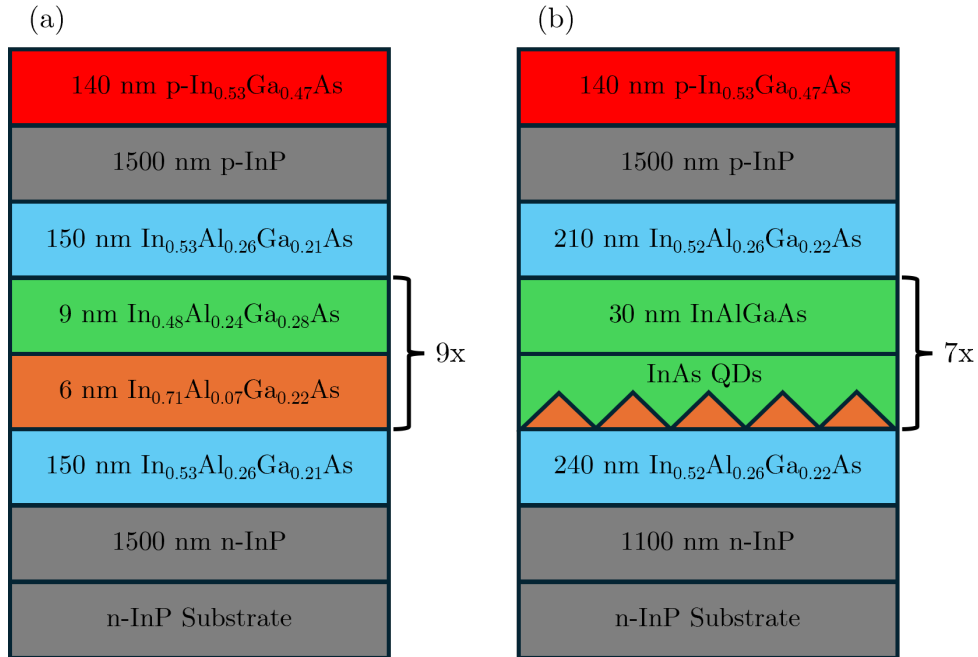


Figure 6.1: Layer diagrams showing the epitaxial structures containing the (a) quantum well active region and (b) quantum dot active region

6.3.2 Device Design

A diagram showing the device design is shown in Figure 6.2. The designed structure was a RWG with the gratings extruding laterally from the ridge. In contrast to the device from the previous chapter, which was shown in Figure 5.1, a high open area design was used. This means that the whole sample was etched excluding the RWG. This was chosen based on fabrication requirements. Specifically, this design minimised the EBL patterning time for the structures. The RWG was again set in BCB 3022 spin on dielectric, with the refractive index contrast coming from this and the upper InP cladding layer. The simulation work described in chapter 3 was utilised to choose the device dimensions. Table 6.1 shows the chosen design types. Five base designs were chosen targeting coupling strengths between 1.5 and 2.2 for a 300 μm cavity length. The devices were fabricated on four 15x15 mm tiles, which included two QW samples and two QD samples. For each material system, one sample included only 1st order and the other sample included both 3rd and 11th order devices. This allowed a reduced etch depth to be targeted for the 1st order devices, which was done to ensure the coupling strength was around a value of $\kappa L = 2$ for a 300 μm length, as well as reducing the aspect ratio of the structures. Additionally, the 11th order devices fabricated in this work were different from those described in the previous chapter. The extrusion

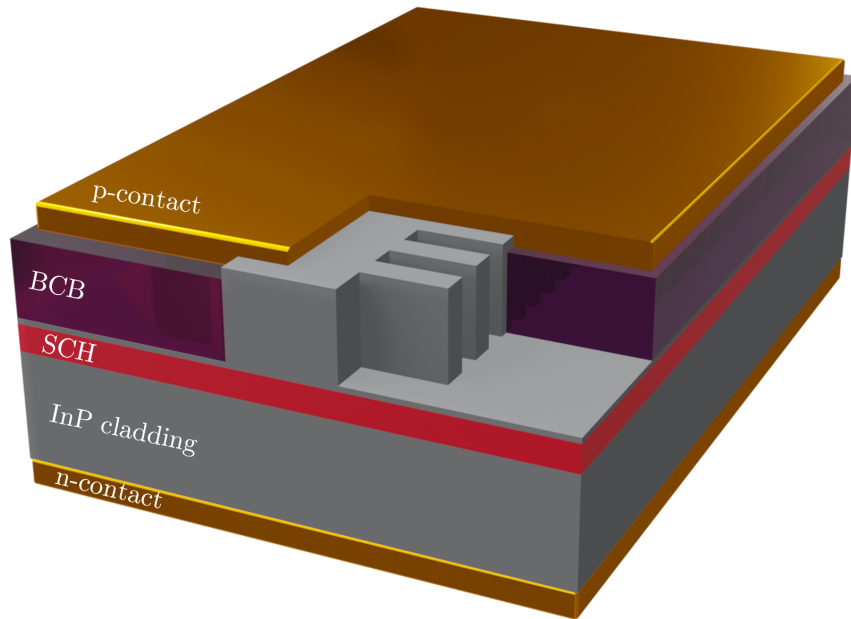


Figure 6.2: High open area RWG LC-DFB structure fabricated in this work.

Table 6.1: Design parameters chosen for the devices in this work.

Grating Order	Etch Depth (μm)	Ridge Width (μm)	Extrusion Length (μm)	Coupling Strength	kL ($L = 300\mu\text{m}$)
1 st	1.35	2	0.5	72.0	2.16
3 rd	1.6	2	0.5	71.0	2.13
11 th	1.6	1.5	4	51.1	1.5

length was reduced to $4\mu\text{m}$ and the ridge width was reduced to $1.5\mu\text{m}$. These changes were made to reduce the effective width of the device, and eliminate the lateral mode competition issues observed in the previous chapter. The devices were also designed with varying pitches in order to compare the range of accessible wavelengths of the QD and QW material systems. These different channels are described in Table 6.2, which shows the designed channel wavelength calculated using equation 3.1, as well as the grating pitch used to target this wavelength for all grating orders.

Table 6.2: Designed wavelength and grating pitches for the 9 channels fabricated in this work.

Channel Number	Designed Wavelength (nm)	Pitch (nm)		
		1 st Order	3 rd Order	11 th Order
1	1538	235	705	2585
2	1550	237	711	2607
3	1564	239	717	2629
4	1577	241	723	2651
5	1590	243	729	2673
6	1603	245	735	2695
7	1616	247	741	2717
8	1629	249	747	2739
9	1642	251	753	2762

The channels were designed across a wavelength range from 1538 - 1642 nm, covering much of the c-band as well as the l-band. This range was chosen as it matched well with results obtained in oxide stripe lasers from the same wafer, which were fabricated by another member of the research group, Z. Cao. On the oxide stripe devices, the emission wavelength was found to range from around 1560 nm for a $300\mu\text{m}$ device up to around 1590 nm for a 2 mm cavity length with no transition to excited state lasing observed, as shown in Figure 6.3. Importantly

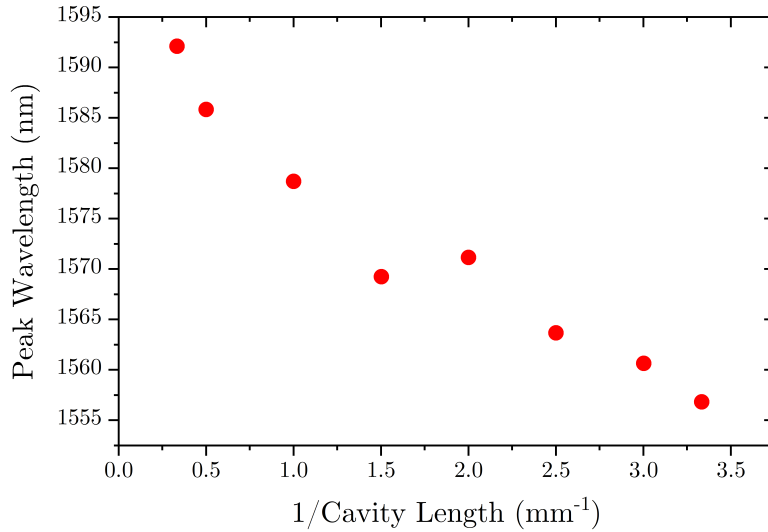


Figure 6.3: Measured peak wavelength as a function of cavity length for broad area devices fabricated on the QD material used in this work.

for later analysis, these results were achieved under pulsed current operation. Therefore, it was expected that the peak gain wavelength would be higher under CW operation due to the redshift that occurs as a result of device self heating [100].

6.4 Fabrication

6.4.1 Process flow

An illustrated process flow for the fabrication of the grating structures is shown in Figure 6.4. The process began with the deposition of a 500 nm SiO₂ hard mask as shown in Figure 6.4a. Following this, the ridge and grating structures were patterned together in the negative tone resist AZ2020. Normally used as a photoresist, AZ2020 is also sensitive to electrons and was chosen due to the fact that it has excellent dry etch resistance. The most commonly used negative tone resist for EBL is hydrogen silsesquioxane (HSQ). This resist is expensive compared to AZ2020 photoresist. Furthermore, HSQ has a recommended dose of 400 - 700 $\mu\text{C}/\text{cm}^2$. As described in the following section, the dose required to expose AZ2020 is significantly less. This leads to an almost seven-fold reduction in patterning time. Following the EBL patterning, the LC-DFB structure was etched

into the hard mask using ICP-RIE with a fluorine based chemistry providing the structure shown in Figure 6.4c. The SiO_2 was then used as a mask during the Cl-based etching of the epitaxial structure. Following this, the remaining hard mask was removed using the same dry etching method as for the original mask etch. The result of this is shown in Figure 6.4d and it represents the completion of the LC-DFB structure. After this point was reached, BCB was spun onto the sample and back etched using a fluorine based chemistry. This was followed by a deposition and lift-off procedure for the p-contact, which was Ti/Pt/Au. The sample was then thinned to $120\ \mu\text{m}$, polished and an n-contact of AuGe/Ni/Au was deposited. Individual chips consisting of up to 12 devices were then cleaved from the sample, mounted onto TO-8 headers and connected to the pins using wirebonding. A detailed process flow can be found in Appendix A.2.

6.4.2 Electron Beam Lithography Process Development

Achieving the correct dimensions during this fabrication was highly dependent on the success of the EBL process step. Process development work was undertaken

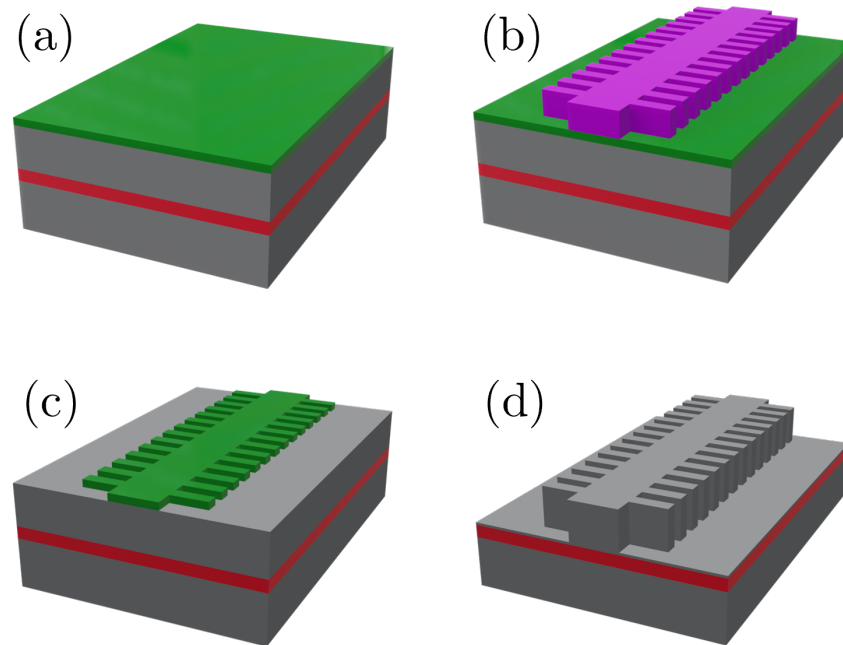


Figure 6.4: (a) Deposition of SiO_2 hard mask using e-beam evaporation. (b) Grating structure patterned in AZ2020 resist. (c) Grating structure etched into the hard mask. (d) Completion of the grating structure following etching into the epitaxial structure.

to assess the best parameters for defining the designed structures. Test structures matching the designs described in Table 6.1 were patterned onto test samples with the same hard mask as would be used during the real fabrication. Test structures were patterned with various dose values and coated with a thin layer of gold using sputtering. The first test used undiluted AZ2020 resist, which was spun at 5000 rpm for 45 s. Following the exposure, a 2 minute post-exposure bake was performed at 110 °C and the samples were developed in room temperature AZ726 developer for 2 minutes. Results from the first test are shown in Figure 6.5. The third order structure shown in Figure 6.5b was well-defined. The ridge width and extrusion length were measured to be $(2.044 \pm 0.019) \mu\text{m}$ and $(431 \pm 7) \text{nm}$, respectively. The duty cycle was measured to be (0.47 ± 0.01) . Conversely, the 1st order structure, as shown in Figure 6.5b, exhibited some broadening and merging of the grating structures at the bottom of the resist. This is likely attributed to forward scattering of the electron beam exacerbated by the thickness of the resist. The resist was measured to be 1.5 μm thick using profilometry, significantly thicker than most standard EBL resists. To remedy the forward scattering issue, an additional dose test was performed using AZ2020 diluted with edge bead removal (EBR) solvent to a ratio of 10:7 grams. Following the same post exposure bake and development methodology as before, the thickness of this resist was measured to be 419 nm. The results of the dose testing performed using this resist are shown in Figure 6.6. Figure 6.6a, b and d show 1st, 3rd and 11th order gratings, respectively. In all cases, well-defined structures were observed and the broadening issue for the 1st order grating structures was no longer present. The duty cycle as a function of dose is shown in Figure 6.6c. From this, a greater

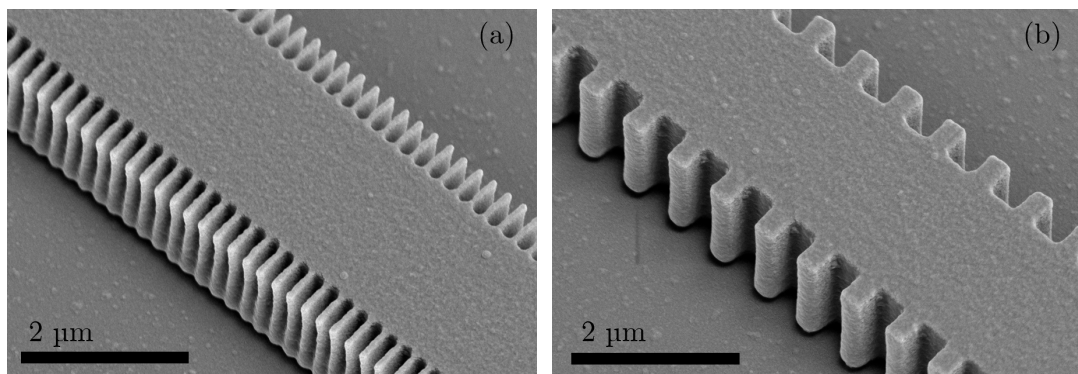


Figure 6.5: (a) 1st order and (b) 3rd order gratings patterned into undiluted AZ2020 resist. The dose used was $50 \mu\text{C}/\text{cm}^2$.

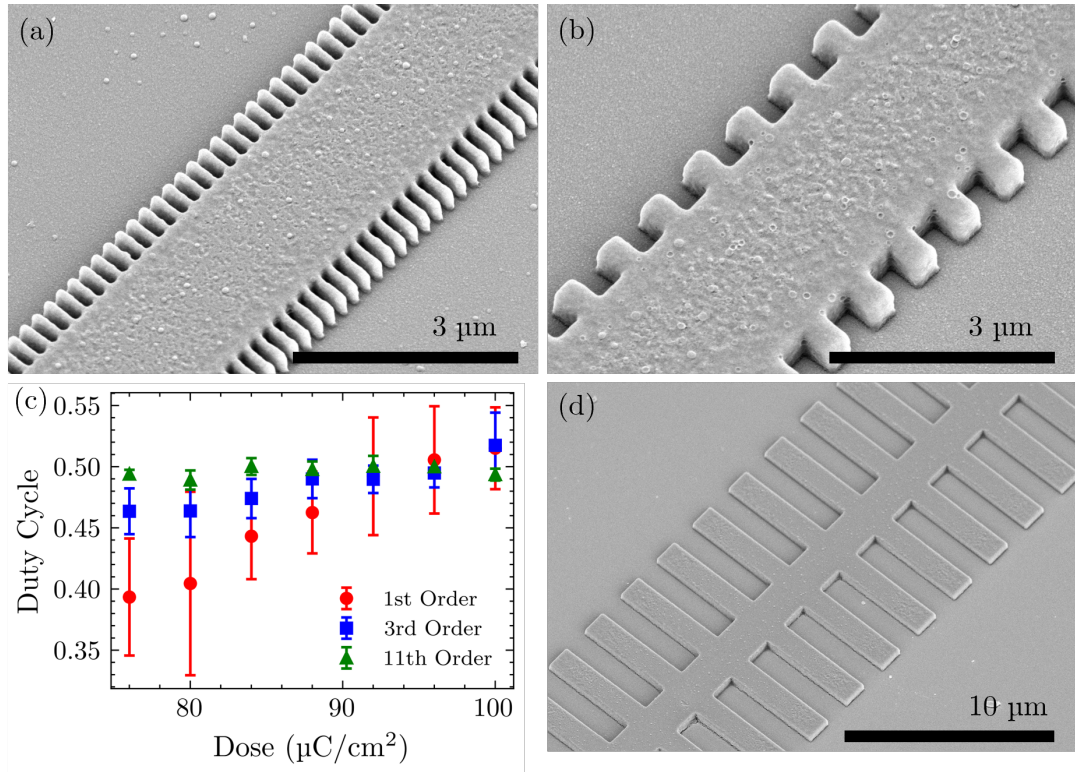


Figure 6.6: (a) 1st, (b) 3rd and (d) 11th order gratings in diluted AZ2020 resist using a dose of 100 $\mu\text{C cm}^{-2}$. (c) Duty cycle as a function of dose for all grating orders.

sensitivity to duty cycle was observed for lower grating orders. This is expected due to the fact that the feature size increases with grating order. Therefore, a characteristic broadening of the resist as result of the electron beam will have a bigger impact on the duty cycle of lower order gratings. The error bars in Figure 6.6c represent the standard deviation in the measured values obtained using SEM imaging. The measurements were made across the entire extrusion length, which means that a large standard deviation indicated a non uniform duty cycle along the grating region. This error was observed to be higher for the first order gratings but generally lower at higher dose values. Therefore, a dose of 100 $\mu\text{C/cm}^2$ was chosen for the rest of the work described in this chapter, as it provided a duty cycle close to 0.5 for all grating orders.

6.4.3 Fabrication Results

Scanning electron micrographs showing various devices at different stages of the fabrication are shown in Figure 6.7. Figures 6.7a - c show the 1st, 3rd and 11th

order gratings respectively, following the etching of the epitaxial structure and removal of the SiO₂ hard mask. All images are shown on a tilt of 30°, allowing the calculation of the etch depth on the exterior of the LC-DFB structure. The first order structure shown in Figure 6.7a was a channel 7 device. The pitch was measured to be (247 ± 8) nm, which agreed with the targeted value of 247 nm. The duty cycle at the top surface of the structure was found to be (0.39 ± 0.05) . The reduction in this value relative to the patterned resist may be attributed to lateral etching of the resist mask during the hard mask etch. The duty cycle was also observed to be non-uniform in the z-direction and some merging of the features was observed at the bottom of the structure. This can be attributed to two things. Firstly the aspect ratio dependent etching (ARDE) effect [88], which may have resulted in a reduced etch rate in the narrow gaps found in the 1st order grating structure. Secondly, if a degree of lateral etching of the resist mask occurred during the hard mask etch, the top surface of the resist would be affected more. This would likely result in non uniformity of the grating teeth width in the z-direction. This could then be transferred to the epitaxial structure during the second dry etch step. Optimising the hard mask etch to limit the lateral etching of the resist may remedy this problem. Figure 6.7b shows a channel-5 3rd order grating structure. The pitch was found to be (732 ± 4) nm which agreed with the target value of 729 nm. The etch depth was found to be (1.67 ± 0.05) μm, slightly higher than the designed value of 1.6 μm. The duty cycle was measured to be (0.61 ± 0.02) at the bottom of the structure, significantly higher than the targeted value of 0.5. As discussed in chapter 3, slight changes in the duty cycle for grating orders larger than 1 can introduce significant changes in the coupling coefficient of the grating, this will be discussed later in this chapter. Figure 6.7c shows the grating structure for a channel-3 11th order device. The pitch in this case was (2631 ± 18) nm, which was in agreement with the designed value of 2629 nm. The etch depth was 1.59 μm. Additionally, the duty cycle was measured to be (0.49 ± 0.02) .

Analysis of the SEM images described above was not sufficient to provide all the necessary dimensions to estimate the coupling coefficient. Specifically, imagery of the interior portion of the grating structure next to the ridge was required to perform an accurate assessment of the coupling coefficient, especially for the 1st order devices. Therefore, following the completion of the fabrication, some the facets of cleaved devices were imaged using SEM. The result of this is shown in Figure

6.8. Imaging in this way provided accurate values for the etch depth achieved, particularly close to the ridge. The etch depth was calculated by measuring the unetched cladding thickness, which is shown in Figure 6.8, then subtracting from the known height of the epitaxial structure above the SCH. Using this technique, the achieved etch depths were compared with the targeted values shown in Table 6.1. A cross section of a 1st order device is shown in Figure 6.8a. Severe footing was observed at the interior portion of the grating structure, which caused the etch depth to be as low as 642 nm close to the RWG. This severe footing can be attributed to ARDE. Specifically, the flux of the etchants is poor within the small gaps in the 1st order grating structure, which leads to a severe reduction in etch rate compared to the open area. A degree of footing was observed in all grating orders, however, the footing in the 3rd and 11th order structures was less severe. This is shown in Figures 6.8b and c. In all cases, the etch depth close to the ridge was lower than designed, which was likely due to the samples not being in the etch long enough. The final fabricated dimensions are shown in Table 6.3.

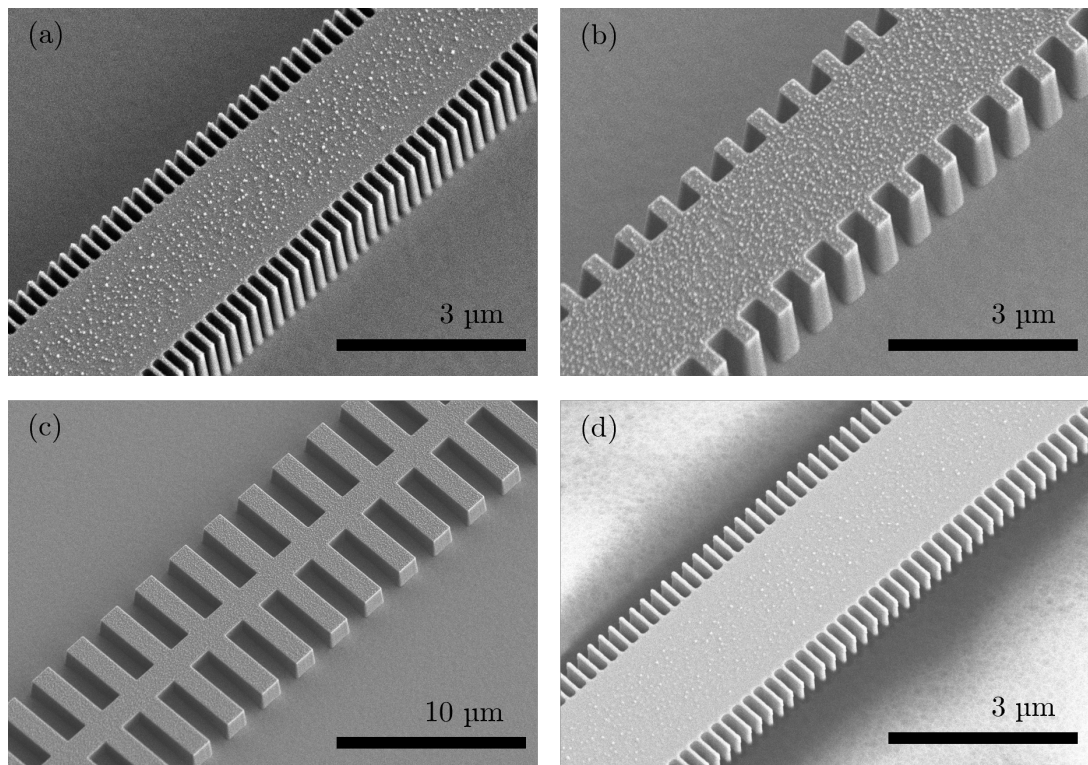


Figure 6.7: SEM images of (a) 1st order, (b) 3rd order and (c) 11th order devices following the etching of the epitaxial structure. (d) shows a 1st order device following the BCB planarisation process.

Table 6.3: Measured device dimensions and recalculated coupling coefficients after completion of the fabrication process.

Grating Order	Ridge Width (μm)	Extrusion Length (μm)	Duty Cycle	Etch Depth (μm)	Simulated Coupling Strength (cm^{-1})
1 st	2	0.5	0.39	497 – 860	0.8 – 3.7
3 rd	2	0.5	0.61	1.04 – 1.37	3.6 – 36.6
11 th	1.5	4	0.49	1.19 – 1.37	17.8 – 40.0

Also shown in this Table are the estimated coupling strengths based on the measured etch depths. The two etch depths represent the measured etch depth at the innermost part of the grating and the outside edge of the grating respectively. The coupling coefficient values were calculated at both of these points. For these calculations the rest of the values remained constant as these were not found to vary significantly compared to the etch depth. The measured coupling strength for the first order devices was found to be significantly lower than designed as

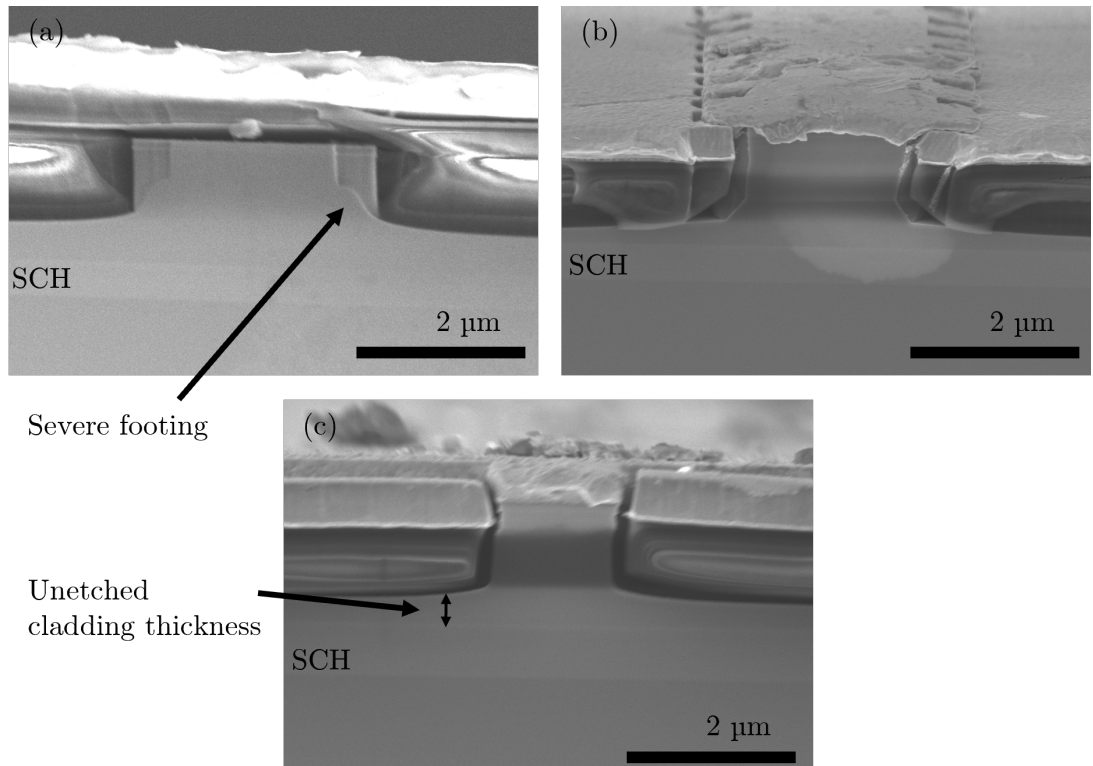


Figure 6.8: Cross sections of (a) 1st order, (b) 3rd order and (c) 11th order devices following the completion of the fabrication.

a result of the etch profile. Even assuming the maximum coupling strength of 3.7 cm^{-1} , cavity lengths of greater than 3 mm would be required to achieve a κL value greater than 1. This was significantly lower than the designed value of 2.16 (Table 6.1). Similarly, the coupling coefficient was found to be lower than designed for both the 3rd and 11th order structures, however, the reduction was not as severe. The range of estimated coupling strength was also smaller for the 11th order devices on account of the reduced variation in etch depth. Taking the midpoint of the two values as an estimate, the κL values would be 2 and 2.9 for the 3rd and 11th order devices respectively, for a cavity length of 1 mm. The fabrication results described here highlight the challenges associated with the fabrication of 1st order LC-DFB gratings. Optimisation of the etch chemistry may provide a remedy to the issues presented here. For example, work has shown that the addition of H₂ into the Cl₂/Ar chemistry may aid in the fabrication of high aspect ratio structures, due to the surface passivating affect from the H₂ [101]. Moreover, reducing the extrusion length may allow the etch products to be extracted more easily, improving the profile. Another issue exists, however, which is that for low order gratings, fine control of the coupling strength is very difficult to achieve. This is because the coupling strength changes rapidly with etch depth in the region above the SCH. Implementing the grating structures away from the ridge such that they do not need to be etched at the same time as the ridge would potentially allow much tighter control of the coupling strength. Such structures will be discussed in later chapters of this work.

6.5 Comparison of Grating Order

The rest of this chapter will be focused on the results of the characterisation undertaken on the completed devices. This will begin with a comparison of the performance of devices with varying grating order. To make this comparison, only devices fabricated on the commercially grown QW material will be described. Furthermore, single mode lasing was not observed in any of the fabricated 1st order devices. This was somewhat expected given the estimated coupling strength values presented in Table 6.3 and was attributed to the poor etch profile observed in these devices (Figure 6.8a). Single mode lasing was, however, observed in both the 3rd and 11th order devices with a cavity length of 1 mm. The results of these devices will form the basis of the comparison described here.

6.5.1 LIVT Results

Figure 6.9 shows the LIVT results for both the 3rd and 11th order devices under CW current operation. Near-field experiments revealed a FWHM of the near-field profile of 3.15 μm and 5.37 μm for a 3rd and 11th order device, respectively. This was used to approximate the current spreading and calculate threshold current density. It is worth noting that this measurement suggests significantly greater current spreading in the 11th order device, despite the fact that the central ridge portion was 1.5 μm compared to the 2 μm ridge width of the 3rd order device. This can be attributed to the width of the contact metal in the two designs. Specifically, since the contact metals cover the whole structure and the extrusion length in the 11th order device is significantly longer, a wider region is being pumped. Figure 6.9a and b show the LIV curves for channel-4 3rd and 11th order devices respectively. Maximum powers exceeding 4 mW were observed for both grating orders. Additionally, the 11th order device exhibited fluctuations in power at higher currents. This may be attributed to shifts to and from DFB operation and will be discussed further in the next section of this chapter. From the IV characteristics, it can be seen that the voltage is higher in the 3rd order devices at the same current density, indicating increased resistance in the device. This is likely a result of the smaller device footprint in the 3rd order devices. Figure 6.9c and d show the threshold current density and slope efficiency as a function of temperature, respectively. Similar values for threshold current density were observed, with only the 11th order channel-5 device exhibiting a slightly

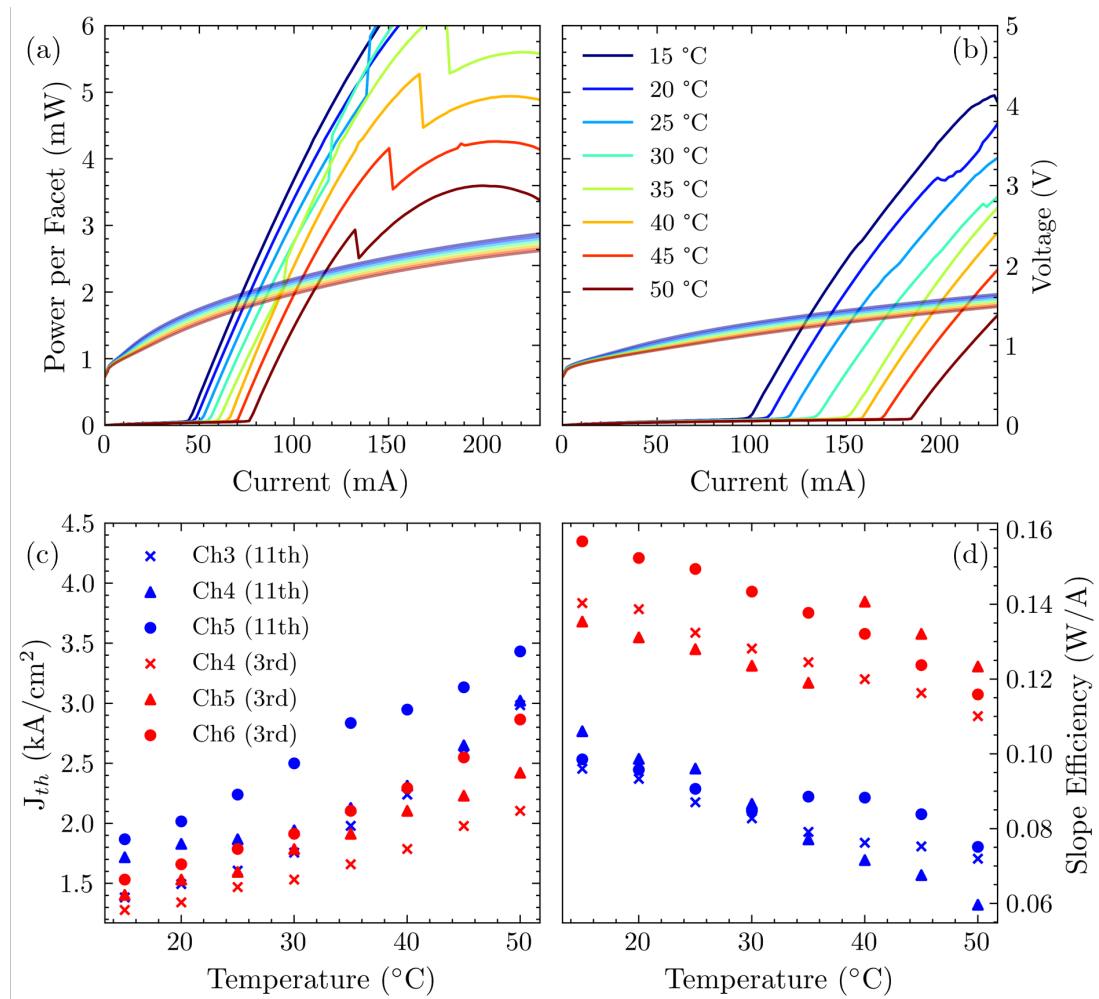


Figure 6.9: LIVT results for QW devices with varying grating orders. (a) and (b) show the LIV curves for channel-4 3rd and 11th order device respectively. (c) shows the threshold current density as a function of temperature for the 6 devices measured. (d) shows the slope efficiency, defined between threshold and 1 mW of power output, as a function of temperature for the 6 devices measured.

increased value. For slope efficiency, however, a clear difference between 3rd and 11th order was observed. For the 3rd order devices slope efficiencies exceeding 0.15 W/A were measured from threshold to an output power of 1 mW, in order to exclude the observed power fluctuations. The highest values achieved for the 11th order devices was around 0.10 W/A. The rate of decay in the slope efficiency was broadly similar between the different grating orders, however. These results may indicate the presence of an optical loss in the 11th order devices that is not as severe in the 3rd order devices, potentially emanating from radiation modes. As these devices have been measured as-cleaved, with no coating applied on the facets, measuring the total light output does not provide a full picture. The reason for this is that it is difficult to tell if this loss affects the DFB mode and FP modes equally. The next section will discuss the spectral results from these devices in an attempt to address this.

6.5.2 Spectral Results

In order to characterise the spectral behaviour of the devices, emission spectra were recorded at current increments of 10 mA across a temperature range of 15-50 °C. Of the 9 channels fabricated, only channels 3-5 exhibited single mode lasing for the 11th order devices. In the case of the third order devices, channels 4-6 exhibited single-mode lasing across the studied temperature range. Example emission spectra of channel-4 3rd and 11th order devices are shown in Figure 6.10. Single mode emission was observed in both cases and the emission wavelength was

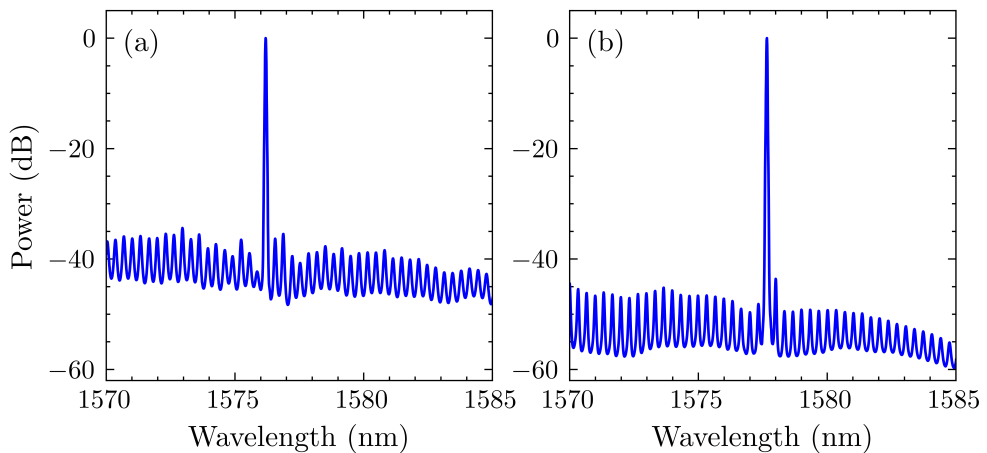


Figure 6.10: Emission spectra recorded at 20 °C and 180 mA for a (a) 3rd order and (b) 11th order channel-4 devices.

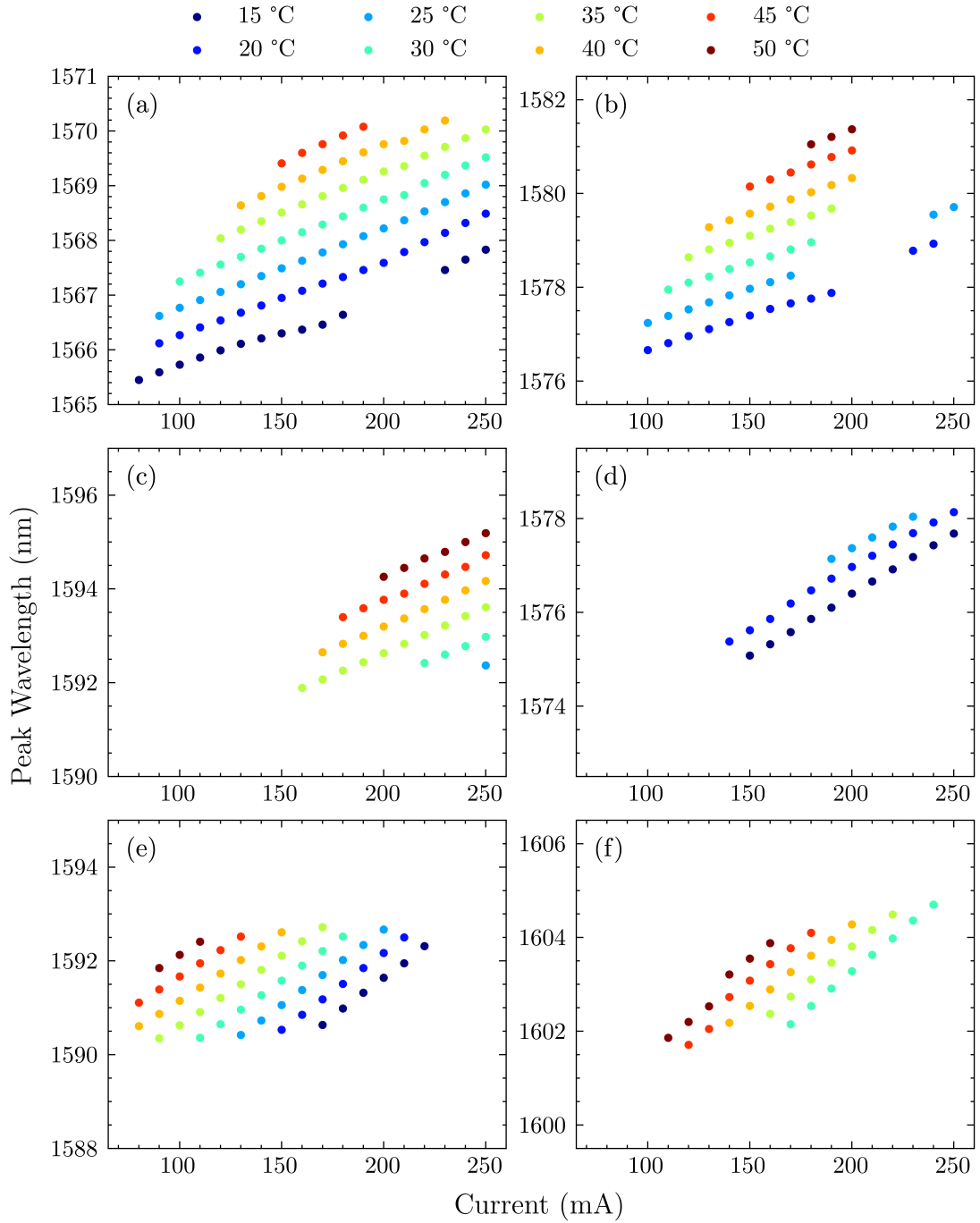


Figure 6.11: Peak wavelength as a function of current at varying temperature for the 11th order (a) channel-3, (b) channel-4, (c) channel-5 and 3rd order (d) channel-4, (e) channel-5 and (f) channel-6. Only the regions where single mode lasing was observed are shown.

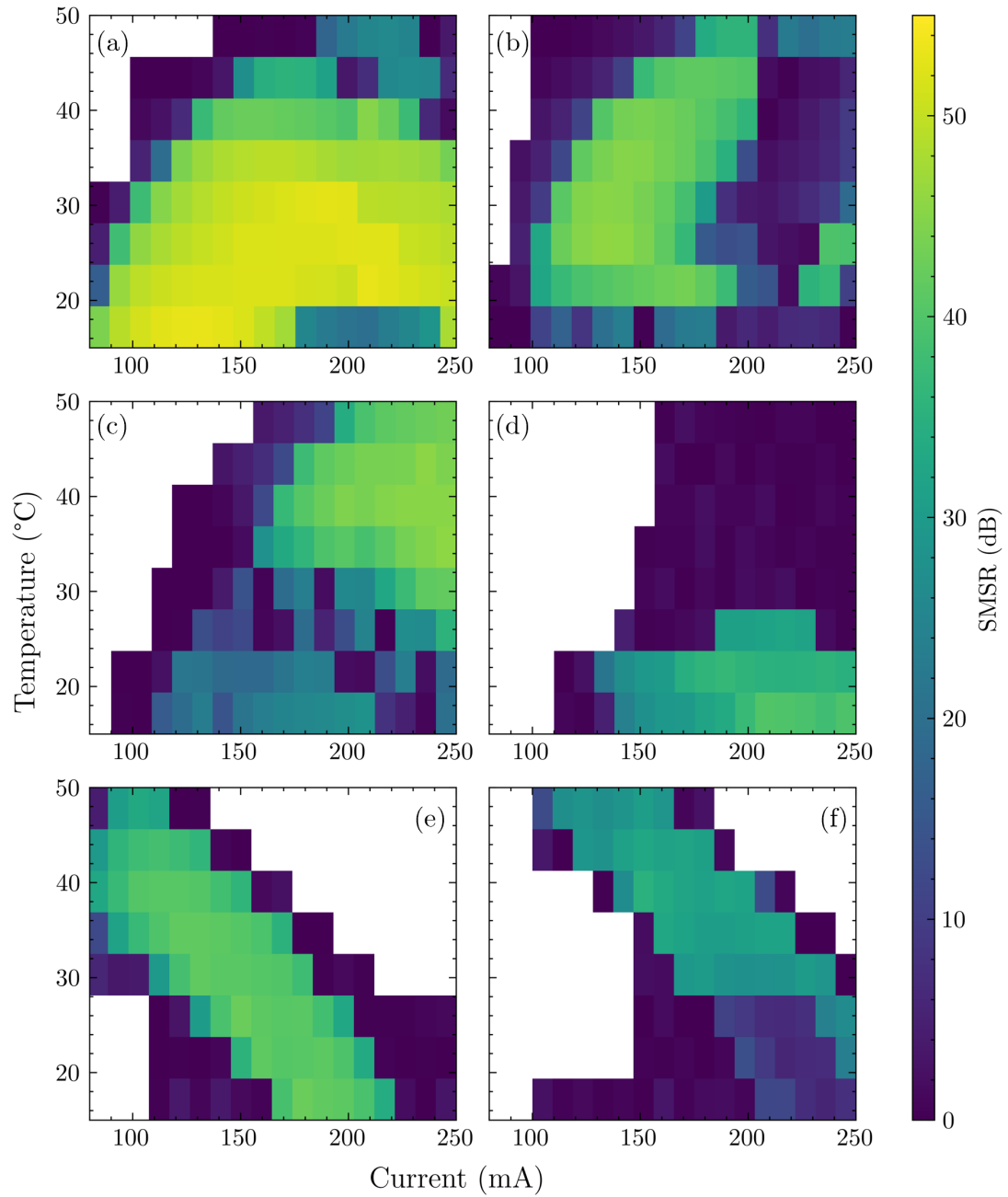


Figure 6.12: SMSR heatmaps for the 11th order (a) channel 3, (b) channel 4, (c) channel 5 and 3rd order (d) channel 4, (e) channel 5 and (f) channel 6.

found to be 1576 nm and 1577 nm for the 3rd and 11th order devices, respectively. This was close to the designed wavelength for this channel, which was 1577 nm. Figure 6.11 shows the peak wavelength as a function of current and temperature for the six DFB device types. Stable wavelength tuning across various ranges was observed. For the 3rd order devices, the channel-5 (1590 nm) exhibited the widest range of accessible temperatures, exhibiting stable single mode behaviour across the whole measured temperature range. Among the 11th order devices, none exhibited single mode behaviour across the whole temperature range. This could be attributed to reduced coupling strength, which would be contrary to the estimated values in Table 6.3. Specifically, when the temperature increases, the gain peak is redshifted at a higher rate than the DFB emission wavelength. Therefore, the detuning between the two increases with temperature. At high detuning values, a greater coupling strength is required to maintain single mode lasing. Additionally, the fact that these devices were measured with facets as-cleaved meant that as the detuning became larger, the cavity modes became more dominant. The addition of an AR coating on one of the facets would likely remedy this issue to some extent, broadening the operational temperature range of these devices. The peak wavelength tuning values are summarised in Table 6.4. In general, similar peak wavelength shifts were observed for the 3rd and 11th order devices when adjusting the stage temperature at a fixed driving current. When adjusting the current under a fixed stage temperature, however, the shift in the peak wavelength was significantly higher for the 3rd order devices. This is likely to be attributed to a higher degree of self heating which arises from the fact that the resistance was larger in the third order devices on account of the reduced device area.

Table 6.4: Measured tuning values with current and temperatures for varying order QW devices.

Device	Temp Shift (nm/K)	Current Shift (mA/K)	Max SMSR (dB)
11 th (Ch3)	0.11	0.01	53.2
11 th (Ch4)	0.11	0.01	45.8
11 th (Ch5)	0.11	0.02	44.3
3 rd (Ch4)	0.14	0.03	40.2
3 rd (Ch5)	0.10	0.03	42.5
3 rd (Ch6)	0.10	0.04	35.1

The SMSR was also studied as a function of temperature and driving current. The

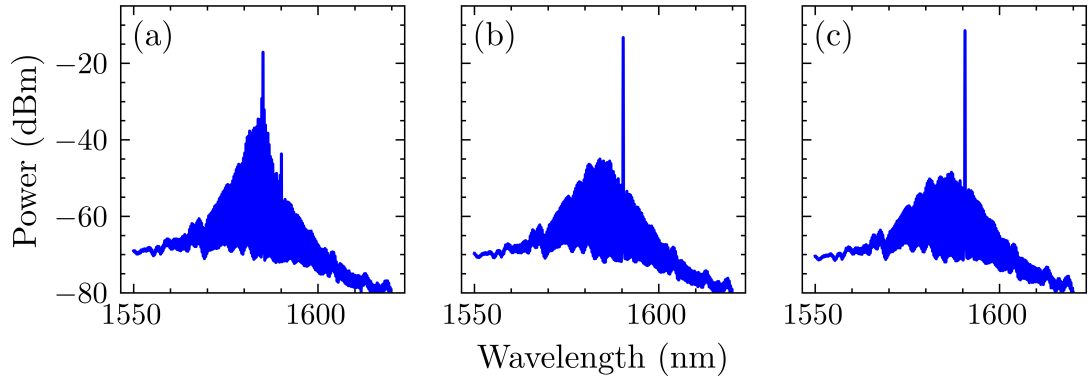


Figure 6.13: Emission spectra of a 3rd order channel-5 device at a stage temperature of 35 °C and a driving current of (a) 80 mA, (b) 90 mA and 100 mA

results of this analysis are shown in Figure 6.12, which shows the SMSR mapped as a function of current and temperature for the 6 device types. Additionally, the max SMSR values are presented in Table 6.4. SMSR values exceeding 35 dB were observed for all devices. In general, however, the 11th order devices exhibit significantly higher SMSR. This can be attributed to radiation modes initiating loss at undesired wavelengths or the fact that the estimated coupling strength was higher for the 11th order devices. These results suggest that the loss introduced with a high order grating is not as severe as expected, as higher SMSR values have been obtained at similar driving currents. One potential avenue for further research in this regard, would be through the fabrication of devices with a AR/HR facet coating scheme. This would remove the influence of cavity modes as much as possible. In the previous section, power fluctuations were observed in the LI curves shown in Figure 6.9a and b. The drop in power that occurs for the channel-5 3rd order device at a temperature of 35 °C (Figure 6.9a), is found to occur at a current density value of 3 kA/cm², which corresponds to a current value of approximately 90 mA. Figure 6.13 shows the emission spectra of the channel-5 3rd order device at values around the power fluctuation. At driving current values less than 90 mA, the FP cavity modes are dominating, with the DFB lasing mode observed at a wavelength of around 1590 nm. As the driving current was increased to 90 mA, as shown in Figure 6.13b, the DFB lasing mode became dominant, increasing the driving current further resulted in an increase in SMSR (Figure 6.13c). This provides evidence that the power fluctuations observed in Figure 6.9 are in fact the result of the devices transitioning from the FP modes to the DFB lasing mode.

6.6 Comparison of 11th Order QW and QD Devices

In this section, the comparison between devices fabricated on the QW material are compared with those on the QD material. All the results presented here were performed under CW operation in the cryostat measurement system described in chapter 4. This was necessary because lasing was not observed in any of the devices fabricated on the QD material system under CW operation at room temperature. The reasons for this will be discussed along with a comparison of the different material systems in this section. 11th order devices were compared as they presented the highest spectral quality. As the temperature was being reduced, channel-1 devices were compared. The reason for this being that the reduction in temperature introduced a blueshift in the gain peak, meaning that DFB lasing was observed only in channels 1 and 2 for the QW material.

6.6.1 LIVT Results

The results of the LIV analysis performed for varying temperatures in the two devices are shown in Figure 6.14. The measurements were performed from 200 K up to 290 K for the QW devices and up to 250 K for the QD devices as lasing under CW conditions was not observed above this temperature. Near-field results for a QD 11th order device revealed a FWHM of 6.47 μm , slightly wider than the 11th order QW devices. This result was again used to calculate threshold current density. Figure 6.14a and b show the LIV curves under varying temperatures for the QW and QD devices respectively. The difference in the IV curves suggest that the QD device has a higher electrical series resistance. The power output was observed to be similar in both material systems achieving a maximum output of greater than 4 mW for the current density range shown. In both devices, power fluctuations were observed throughout the temperature range. This is attributed to the device changing between the DFB lasing regime and the FP regime. Power fluctuations like this may be remedied by the introduction of a facet coating scheme, which would suppress the FP cavity modes. In order to understand the self heating effects present in the two devices, LIV characterisation was performed under both pulsed and CW operation. Figure 6.14c shows the threshold current density as a function of ambient temperature for both devices

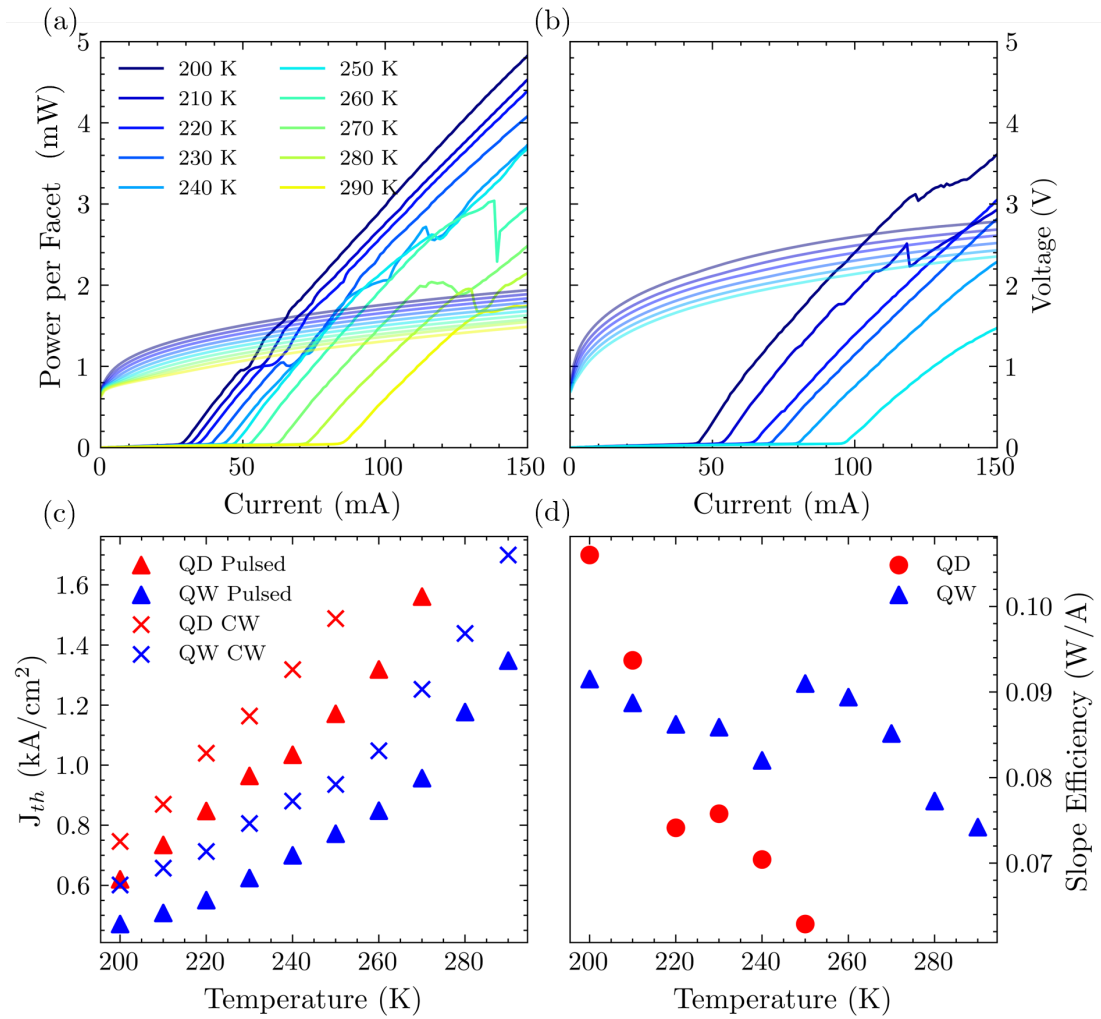


Figure 6.14: (a) and (b) show the LIV curves for varying temperature for the channel 1 QW and QD devices respectively. (c) shows the threshold current density as a function of temperature for both materials under pulsed and CW operation. (d) shows the slope efficiency as a function of temperature for both devices on both materials.

under the two current conditions. From this we observe a greater rate of threshold current density increase for the QD material under both conditions. Furthermore, the characteristic temperature value under pulsed current operation was found to be 80 K and 86 K for the QD and QW devices respectively, which suggests a similar response to changing ambient temperature. Under the CW current operation these values were found to be 73 K and 89 K for the QD and QW devices respectively. This provides evidence of increased temperature sensitivity from the QD material, which is contrary to what has been observed in QD devices targeting o-band wavelengths [102]. Finally, we can quantify the extent to which the temperature of the active region is increased by measuring the difference in temperature values for the same threshold current densities under pulsed and CW operation. For both devices this was found to be around 20 K. This result suggests that the devices exhibit similar levels of self heating but the QD device is more sensitive to changes in temperature. The reasons for this are not obvious based on the results described here and remedies for this are more likely to be gained with advances in growth technology rather than device architecture.

6.6.2 Gain Measurements

One of the aims of this work was to assess the accessible region of wavelength for both material systems. In particular, if the QD material had undergone inhomogeneous size broadening, the gain spectrum would be wider and a greater range of wavelengths would be accessible at the same temperature than the QW material. As CW lasing was not observed under CW current conditions above 250 K, however, a direct comparison could not be made. This was due to the fact that the channels were not designed at a low enough wavelength to accommodate the shift in the gain spectrum at the lower temperatures used for the comparison. Therefore, in order to compare the gain spectra between the two materials, the Cassidy method was performed. This method was described in chapter 4 and in order to perform the measurement, emission spectra of the 11th order channel-1 devices were taken sub-threshold. Figure 6.15 shows the calculated gain spectra for both devices at a temperature of 250 K. The driving current density was determined to be 0.78 kA/cm² and 1.42 kA/cm² for the QW and QD devices, respectively, using the near-field methodology described in chapter 4. These driving conditions were chosen so that the peak gain magnitude was approximately the same for both devices. The width of the gain spectra were measured at 0 cm⁻¹

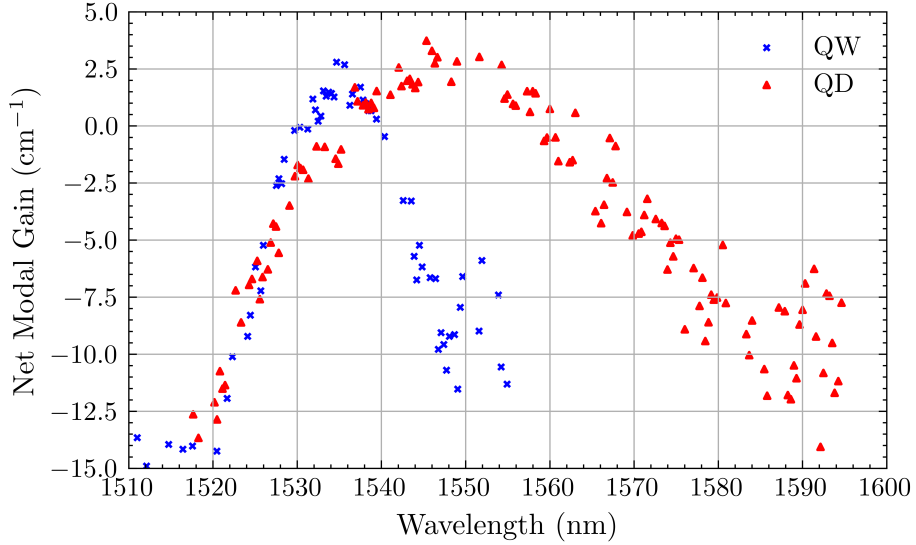


Figure 6.15: Net modal gain spectra for the both materials at 250 K, calculated using the Cassidy method. The driving current for the QW device was 0.78 kA/cm^2 and 1.42 kA/cm^2 for the QD device.

and were found to be $(26 \pm 3) \text{ nm}$ and $(7 \pm 2) \text{ nm}$ for the QD and QW devices, respectively. This result suggests that a wider region of positive gain exists in the QD material assessed here, likely as a result of inhomogeneous size broadening during the growth stage.

Comparing the gain width measured here with previous work described in the literature is challenging since the gain spectra were measured here below the threshold current density and at a reduced temperature. A comparison of the photoluminescence spectrum can be made, however. Photoluminescence data measured by the MOCVD research group at Cardiff University revealed a full width half maximum (FWHM) value of 69 meV at room temperature. This was measured after the growth of the QD layers but prior to the growth of the upper cladding layers of the laser structure. This value is large compared to examples of InAs/InAlGaAs QDs previously described in the literature, particularly those grown using molecular beam epitaxy (MBE). For example, Banyoudeh and Reithmaier presented dots targeting C-band emission with FWHM values as low as 21 meV with 6 layers of QDs [103]. More recently, the same research group has demonstrated even lower linewidth values of 18.8 meV [104]. It is worth pointing out that these measurements have been carried out at a temperature of 10 K which may narrow the FWHM further. Recent examples where the measurement

has been carried out at room temperature include work by Yu et al, which demonstrated 5 layers of InAs/InAlGaAs dots with a FWHM value of 50.9 meV [105], still significantly lower than material used in this work. Comparing to recent examples where MOCVD has been used as the growth technique, work by Wang and colleagues demonstrated five QD layers with a measured FWHM at room temperature of 40.1 meV, which represents the lowest value for MOCVD grown InAs dots to date [106]. Overall, the material used here exhibits a wider FWHM than the current state of the art presented in the literature, suggesting a greater degree of size broadening in the dots used in this work. Whilst this may result in increased threshold current density for lasers fabricated on the material, it may offer the ability to access a greater wavelength range.

6.6.3 Spectral Results

In order to compare the accessible wavelength range of the two material systems, spectral measurements were taken at a range of temperatures for channel-1 devices. Since the gain peak is more sensitive to temperature change than DFB lasing wavelength, the temperature range where single mode lasing occurs can give further indication of whether the useful width of the gain spectrum is larger for the QD material system. Figure 6.16 shows the wavelength results for this comparison. Figure 6.16a and b show the peak wavelength as a function of driving current with varying temperature. Only the range where single mode lasing occurred is shown. A wider range of temperatures is observed for the QD material, where an operating range of 55 K for the DFB mode was observed. It is also worth noting that temperature degradation effects above 250 K, meant higher values could not be measured. Additionally, some fluctuations of the wavelength were observed for the QD device. This is potentially attributed to mode hops between the two lasing modes either side of the Bragg wavelength or mode hops between lateral modes in the device. Notably, no transition to excited state lasing was observed for the device under the measured conditions. For the device on the QW material, a DFB operating temperature range of 30 K was observed. The tuning values for temperature and current are described in Table 6.5. A similar tuning performance with temperature was observed for both materials, however, increased wavelength sensitivity to changing driving current was observed in the device on the QD material. This is likely attributed to the higher resistance observed in the QD device, the result of which is a more rapid increase

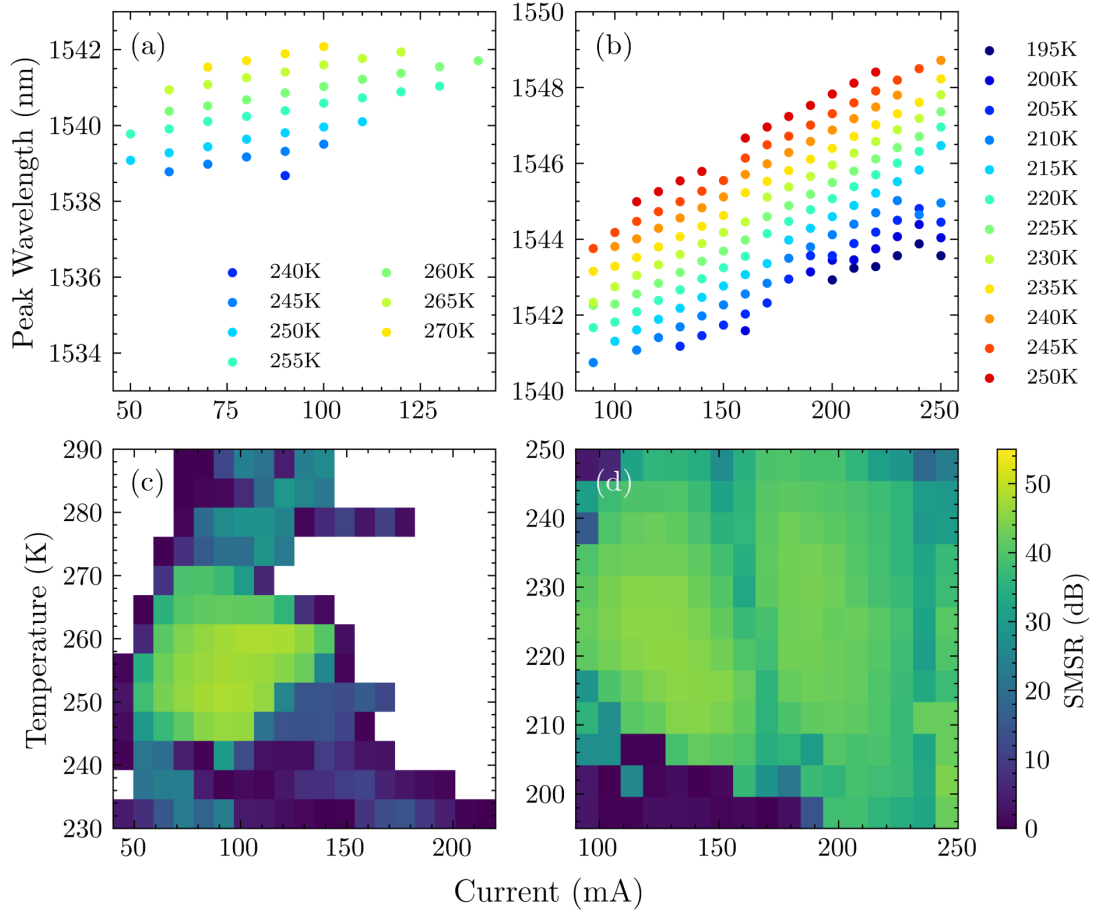


Figure 6.16: Wavelength characteristics of 11th order channel 1 devices on both the QW and QD material. Peak wavelength as a function of current for varying temperature is shown for the (a) QW device and (b) QD device. SMSR heatmaps are also shown for the (c) QW device and (d) QD device.

in temperature with increasing driving current.

Table 6.5: Measured tuning values and SMSR for the channel 1 11th order QW and QD devices.

Material	Temp Shift (nm/K)	Current Shift (mA/K)	Max SMSR (dB)
QD	0.10	0.03	45.5
QW	0.10	0.02	48.3

Figure 6.16c and d show the SMSR heatmaps for the QW and QD devices respectively. Similarly high maximum SMSR values were achieved of 48 dB for the QW device and 45 dB for the QD device. The range at which high SMSR values were

achieved, however, was significantly larger for the device on the QD materials system for both current and temperature changes. This provides further indication of a larger accessible wavelength range, potentially resulting from inhomogeneous size broadening in the QDs.

The spectral performance demonstrated here compares well with previous results achieved by other groups. For example, Kim et al demonstrated an InAs/InAlGaAs QD DFB laser targeting C-band laser emission in 2006 [107]. In this case, a buried grating RWG structure was used with a 1 mm cavity length and one facet HR coated. An SMSR value of 42 dB was achieved with a threshold current density of 1.23 kA/cm². More recent work from Duan and colleagues improved on this value demonstrating SMSR values exceeding 50 dB with a threshold current of 46 mA [108]. In this case a buried grating was also used with an HR/AR facet coating scheme. LC-DFB laser structures have also been implemented on InAs/InAlGaAs QD material. A recent example of this includes work by Sep-ton et al, which presented a 1st order LC-DFB laser with a SMSR exceeding 50 dB with a single mode operating temperature range of 60 K and a threshold current less than 50 mA for a 1.5 mm cavity length [109]. In this case, multiple phase shifts were used in the grating along with an HR/AR facet coating scheme. Additionally, work performed at Waseda University in Tokyo demonstrated an LC-DFB laser on InAs/InAlGaAs QD material with 14 layers of dots [49]. In this case, a first order grating was also used here with a two step etch process used in its fabrication. A threshold current density of 2.2 kA/cm² was demonstrated with an SMSR of 44 dB. Moreover, the device exhibited single mode lasing over a temperature range of 70 K [110]. Once again, HR/AR facet coatings were used in this case to suppress the FP modes. Contrasting the previous examples described with the results obtained in this work, it is clear that the spectral purity compares well what has previously been presented. Specifically, the SMSR values achieved here, which are as high as 45 dB for the QD devices measured, have been achieved without the need for facet coating schemes as in all the other examples discussed. This fact highlights the ability of the 11th order grating structure to simplify the fabrication procedure through the removal of extra coating steps. Furthermore, the single mode temperature operating range observed here of 55 K, compares well with the examples discussed and would likely have been higher if lasing was observed above 250 K. Where the results presented here differ from the previous literature is in their electrical performance. The threshold current density of the

devices measured here is higher than the recent examples on similar material systems and the examples discussed all demonstrated results at room temperature under CW operation. As has been mentioned previously, this discrepancy may be due to the growth itself. Specifically, the photoluminescence spectrum observed for the material used in this work suggested that a large degree of size broadening was present. Improving the size homogeneity of the dots would likely reduce the threshold current density values and improve device efficiency.

6.7 Summary

This chapter has described the design, fabrication and characterisation of various grating order DFB lasers on both commercially grown QW material and MOCVD grown QD material. This chapter had two primary aims, the first of which was to compare the performance of low-order gratings with higher-order gratings. Secondly, this chapter aimed to assess whether a wider range of wavelengths could be accessed using QD material as a result of inhomogeneous size broadening.

The results of the fabrication highlighted the challenges associated with defining 1st order LC-DFB gratings on the InP material system, due to aspect ratio dependent etching. As a result of these issues, the 1st order devices fabricated in this work did not exhibit single mode lasing. Dimensions closer to the designed values were achieved for the 3rd and 11th order gratings, however, a reduction in the estimated coupling coefficient was observed due to variation in the etch profile as well as insufficient etch depth.

The characterisation of 3rd and 11th order gratings revealed similar threshold current densities, with a reduction in the slope efficiency observed for the 11th order devices. This was attributed to the diffraction loss associated with the use of higher order reflections. Analysis of the spectral performance of the devices revealed that the existence of the diffraction loss did not affect the single mode performance of the devices. In fact, the 11th order devices exhibited higher SMSRs at a reduced current density. These results suggest that, as well as offering simpler fabrication, there no penalty for increasing grating order on spectral performance. The reduction in slope efficiency observed for the 11th order devices may, however, be an issue in some applications.

The final section of this chapter compared the performance of 11th order gratings

fabricated on both the QW and QD material systems. Lasing under CW conditions was only observed for the QDs at temperatures lower than 260 K, potentially due to the high electrical resistance observed in these devices. In order to assess whether a widened gain spectrum was present in the QD material system, sub threshold spectral measurements were taken of devices on both materials in order to calculate the gain through the Cassidy method. The current density values for the QW and QD material were 0.78 kA/cm^2 and 1.42 kA/cm^2 , respectively, which corresponded to a peak gain of approximately 3 cm^{-1} . The gain spectrum width was observed to be almost 20 nm wider for the device on the QD material. Additionally, analysis of the photoluminescence spectra of the QD material demonstrated a FWHM value of 69 meV, suggesting significant size broadening had taken place during the growth. Further spectral measurements of the emission above threshold demonstrated peak SMSR values of 48 dB for the QW device and 45 dB for the QD device. Additionally, the QD device had a single mode temperature operating range of 55 K, significantly higher than that of the QW device, which was 30 K. These results suggest the presence of a widened gain spectrum in the QD material system as a result of inhomogeneous size broadening.

Chapter 7

Direct Milling of LC-DFB Grating Structures Using Focused Bismuth and Gold Ions

7.1 Introduction

This chapter describes the design and process development for laterally coupled DFB laser gratings fabricated with FIB nanofabrication. The aim of this work was to harness some of the key advantages that FIB has over other direct write lithography techniques such as electron beam lithography and overcome issues with etching high aspect ratio nanostructures such as 1st order gratings. A context of this work will be provided along with a discussion of the design parameters and simulation work performed to predict performance. Finally a discussion on the process development that was performed on the FIB lithography system to realise the designed structures will be presented along with the results of the fabrication and expected performance.

7.2 Motivation

Although high spectral purity can be achieved using higher order gratings, as shown in chapter 6, it is still desirable to have the ability to create first order DFB laser gratings. The reason for this is that to achieve the maximum coupling

strength, and therefore the shortest cavity length, 1st order grating structures are required. Short cavity lengths less than 300 μm are a requirement when devices are to be directly modulated. Furthermore, single mode transmission sources in PICs, such as the SG-DBR laser require grating mirror sections with relatively high coupling coefficients, often of the order of 300 cm^{-1} [111]. Achieving these values with higher order gratings would require long mirror regions increasing the device footprint substantially. As shown in the previous chapter, however, achieving 1st order laterally coupled gratings in the InP material system is challenging. The main reason for this is due to ARDE. FIB nanofabrication presents itself as a potential way of circumventing this issue, as the grating structure can be defined by a milling procedure separate from other large scale features on the sample. In a DFB laser process flow, this means that the RWG structure can be defined using standard photolithography and etched in a conventional way, followed by direct milling of the grating structure. The aim of this work was to assess the suitability of direct milling with heavy ions in the fabrication of DFB laser gratings.

Historically, applications in the semiconductor industry using FIB systems have been found in material and device characterisation, particularly for failure analysis [112], repair [113] and transmission electron microscopy (TEM) sample preparation [114]. The use of focused ion beams to define photonic structures has been presented in the literature previously. In particular, FIB has been used for developing prototypes for photonic crystals [115] and fibre Bragg gratings (FBGs) [116] among others. In these previous works, gallium is most often used as the source ion due to the fact that stable liquid metal ion sources (LMISs) are readily available in this material [117]. So far, however, applications for FIB have been limited to small-scale prototyping, on account of the long patterning times required. Work has been done to address this, and in the context of DFB lasers, Rennon et al demonstrated a LC-DFB laser with a grating defined using a gallium focused ion beam [118]. In this work they used the gallium ions to locally implant the grating region, after which an annealing process results in quantum well intermixing in the implanted regions. An HF etch was then used in this case to selectively remove the implanted areas. The result was a complex coupled grating due to both the index modulation and the modulation of the band gap absorption. A high SMSR of 45 dB was achieved in this case, however, the profile of the grating structure is determined by the implantation profile [119]. This

cannot be controlled in the same way as direct milling of the grating structures would allow. Routes to decreasing the patterning time of direct milling methods are, therefore, of high importance.

One potential time saving is to use sources that utilise heavy ions. Heavier ions such as bismuth and gold offer increased sputter yields and therefore reduced patterning times [120, 121]. Since these ions are not liquid at room temperature like gallium, creating stable sources using these materials is more challenging. Recent developments in source technology, however, have resulted in sources where the heavier elements are alloyed with other elements to encourage stability. These are referred to as liquid metal alloy ion sources (LMAISs) and they have the added benefit of offering the ability to change ion depending on the application. For example, having the ability to switch to a lighter ion such as lithium improves the imaging resolution of the FIB [122].

In this work, the heavy ions, bismuth and gold have been used to define DFB gratings on RWG laser structures. Two structures are described, the first of these is the on-ridge grating DFB structure, which is similar to that which has been studied in chapter 6 and is shown in Figure 7.1a. The second structure which has been examined is the off-ridge DFB grating structure. In this case the grating is defined adjacent to the RWG on the floor of the etched trench, as shown in Figure 7.1b.

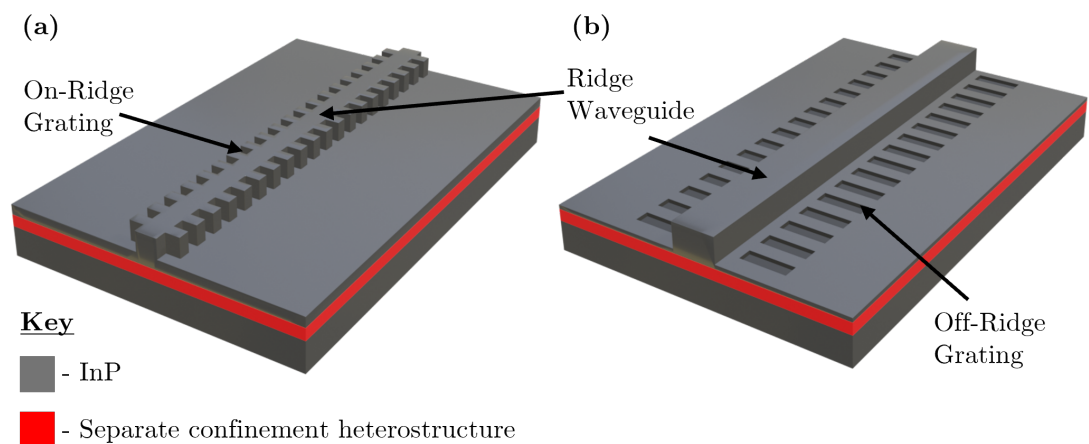


Figure 7.1: Schematics showing the (a) on-ridge and (b) off-ridge grating structures [123].

7.3 Ridge Waveguide Preparation and Testing Methodology

All the work described in this chapter was performed on the same material system described in previous chapters (Figure 6.1a). The ridge waveguides were defined first using projection lithography into AZ2020 negative tone photoresist. This pattern was then etched into a 400 nm SiO₂ hard mask, which was then used as the mask to etch the ridge into the epitaxial structure. The target etch depth for the RWG was 1.5 μm . The RWG had a range of widths varying from 1.5 μm to 4 μm . Test gratings were then milled into the RWG structures, which each had 20 periods on a grating pitch of 238 nm, corresponding to a target wavelength of 1550 nm. SEM imaging was used to examine the fabricated test structures. Additionally, FIB cross sectioning was used to reveal sub-surface features.

7.4 Milling Parameters

All of the FIB work described here was performed by the author at the University of California Santa Barbara (UCSB) Nanofabrication facility, on the Raith Velion system described in chapter 4. A beam current of 30 pA was used with a 40x40 μm writefield and a beam step size of 5 nm. Three types of scanning routine were used in this work; single pixel line (SPL), longitudinal area and concentric area. In the SPL scanning routine the gaps in a grating structure are defined as lines with a width of 1 pixel or beam shot with a periodicity equal to the pitch of the designed grating structure. This is by far the simplest method for the design process as the number of parameters that can be changed is limited. For example, a SPL can only be scanned in two directions limiting the degree of control achievable on the milled profile.

For the two area scanning routines on the other hand, each gap is defined by a 2d rectangle. This means that each shape can be scanned in a number of different ways. The longitudinal scan separates the shape into a series of lines and scans each one as a SPL. Among this scanning routine there is flexibility over whether individual lines that make up the shape are scanned in the same direction or alternate directions. In the concentric scanning routine, the shape is scanned radially either outwards or inwards. The three types of scanning routine are

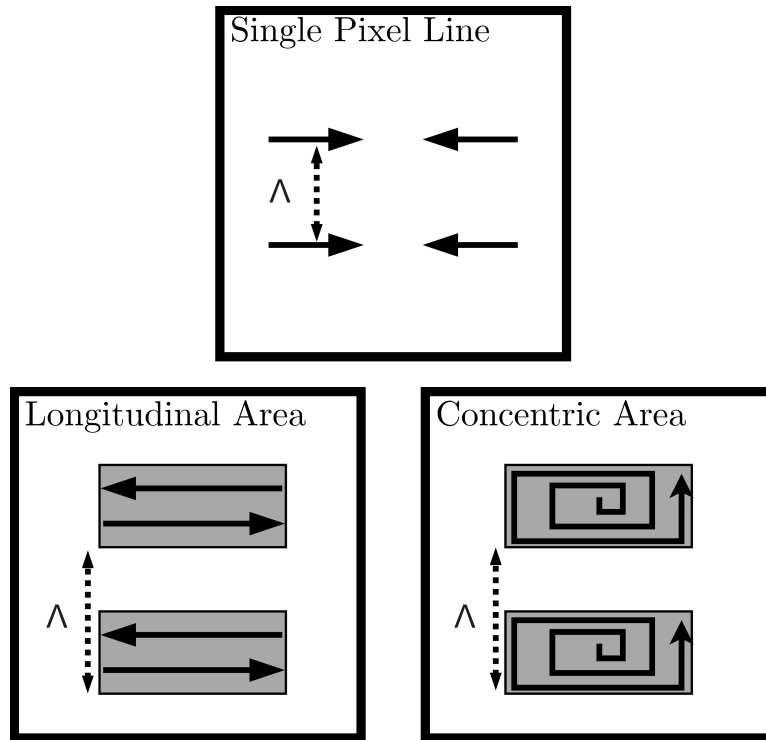


Figure 7.2: Schematic illustrating the scanning routines used in this work [123].

illustrated in Figure 7.2. A common parameter shared among all the scanning routines described here is known as loops. This parameter represents the number of times each pixel is addressed by the FIB. Increasing the number of loops has the effect of distributing the dose in each pixel over the number of loops chosen i.e. each pixel receives a dose of $1/n$ multiplied by the dose, where n refers to the number of loops. Increasing the number of loops is usually done to minimise the redeposition effect [124], which is where removed material gets deposited onto an area that has recently been milled, affecting the depth of the finished structure.

7.5 On-Ridge Grating Structures

Milling of the grating structures directly onto the RWG will be described first. This type of device followed the same structure as the first order devices described in the previous chapter. The results of both the SPL scanning and area scanning routine will be described here. The ridge depth was variable across the test samples used, therefore, the target milling depth also changed depending on the sample.

7.5.1 Single Pixel Line Scanning Routine

Figure 7.3 shows the results of using the SPL scanning routine to define the on-ridge gratings with both bismuth and gold ions. Figure 7.3a shows the result of using bismuth ions and a SPL scanning routine with a dwell time of 3 ms per pixel. This gave a dose of 158 nC/cm which was delivered in a single loop. In all cases where a SPL scanning routine has been used with a single loop, the beam direction was chosen to start from the outside of the ridge and move inwards. Doing this takes advantage of more efficient milling that occurs when moving against topography as sputter yield increases with the incidence angle of the beam [125]. Where only a single loop has been used, the milled gaps appear teardrop shaped on the top surface of the ridge. Measurements of the pitch and gap size suggested a pitch of (239 ± 5) nm, which was close to the designed pitch of 238 nm. The gap width at the ridge surface was found to be (22 ± 5) nm at its narrowest point and (115 ± 7) nm at its widest point, which correspond to duty cycles of 0.91 and 0.52 respectively. When the number of loops is increased to 1000, as is shown in Figure 7.3b, the profile on the ridge appears more uniform. In this case however, a dose of 264 nC/cm with a pixel dwell time of 5 μ s was required in order to mill the gaps to the bottom of the ridge at the exterior. The pitch was again found to be (239 ± 7) nm and the gap size was measured to be (128 ± 7) nm throughout the structure, providing a duty cycle of 0.46. The effects observed here can be attributed to redeposition, as where a single loop is used, some of the removed material is immediately deposited behind the beam which had previously been milled. This means that the milled area is wider on the surface at the end of the milled shape. The disadvantage to increasing the number of loops in this case is that some of the benefit of milling against the ridge is lost, due to the fact that the beam is scanning in both directions. This explains

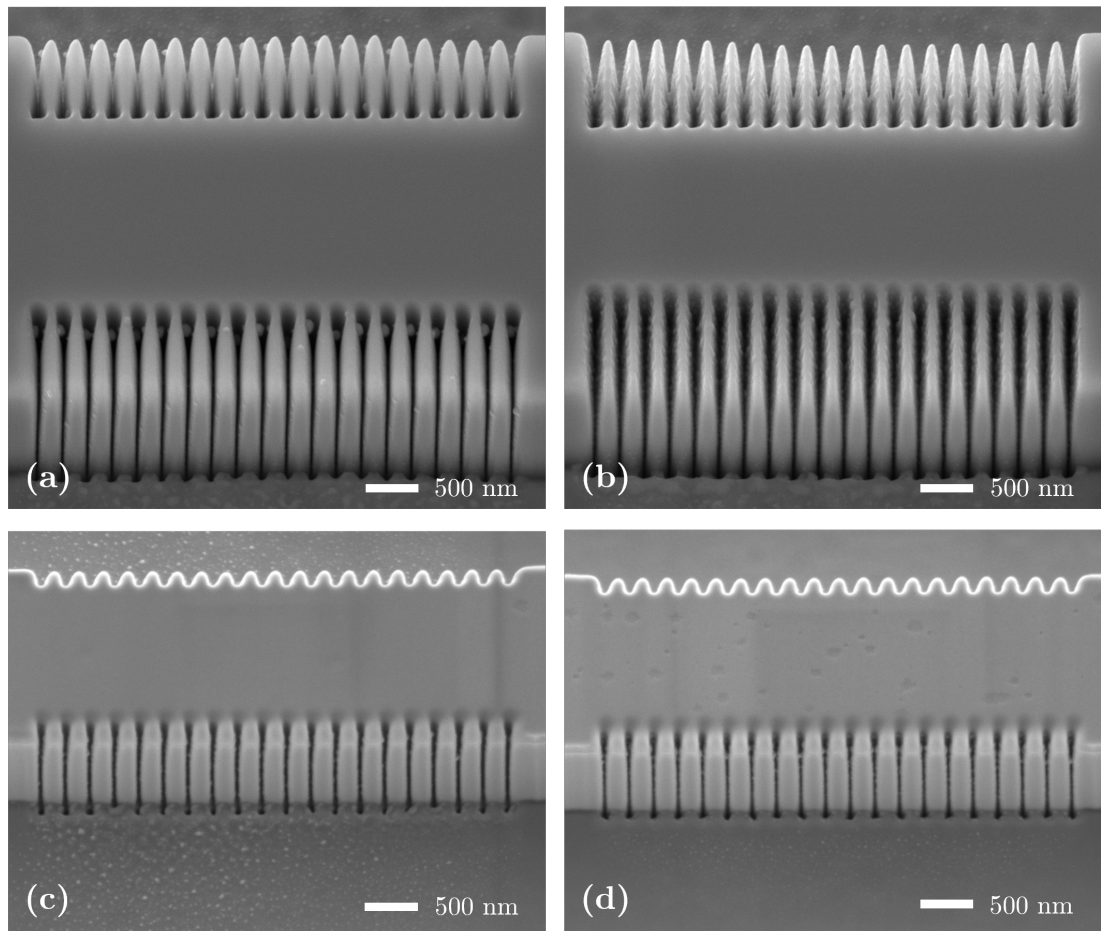


Figure 7.3: Gratings milled on-ridge with the SPL scanning routine and bismuth ions with a dose of (a) 158 nC/cm and 1 loop and (b) 264 nC/cm and 1000 loops. Gold ions with a dose of (c) 150 nC/cm and 1 loop and (d) 250 nC/cm and 1000 loops [123].

why increasing the number of loops required a higher dose to fully mill through the ridge. Where the gold ions were used for the same test, as shown in Figures 7.3c and 7.3d for 1 and 1000 loops respectively, the effect of changing loops was not observed to be as dramatic. This is likely attributed to the different ridge dimensions between the test samples used for each ion.

7.5.2 Cross-sections

Cross-sections were achieved by depositing a protective layer of platinum and subsequently milling grating structures to reveal their interior. Cross-sectioning was performed on structures milled using gold ions on RWG structures with

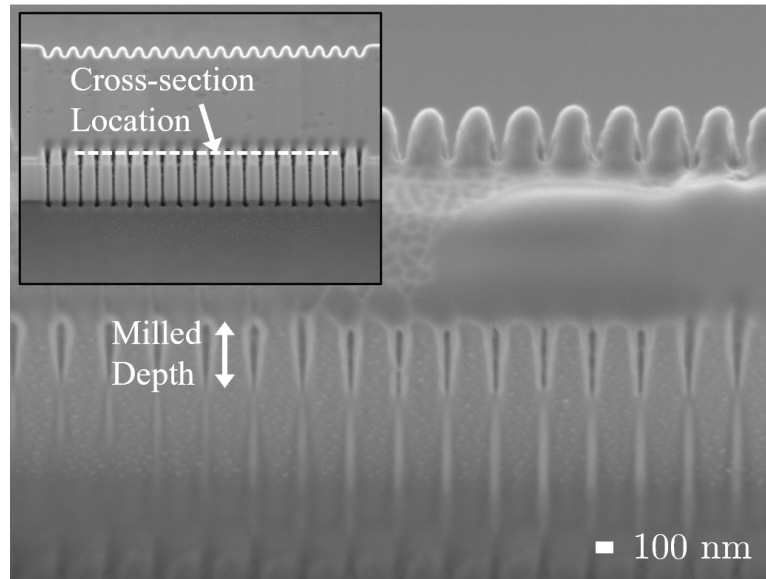


Figure 7.4: Cross-section of a grating milled on-ridge using gold ions and a dose of 400 nC/cm [123].

a depth of 1.6 μm , with 1 and 1000 loops. The required total dose to fully mill through the exterior of the RWG was found to be 300 nC/cm and 400 nC/cm for 1 and 1000 loops respectively. In both cases, cross sectioning revealed that although the gaps has been milled completely through the exterior of the ridge, in the interior portion, the gratings were not milled through the structure completely. Figure 7.4 shows an example of this in the case where 1000 loops were used. In this case the gratings were found to be milled to a depth of (786 ± 9) nm at the interior of the grating structure. Where a single loop was used, the depth achieved was (1078 ± 16) nm. In both cases, the milled depths were substantially less than required. Since the interior portion of the grating is the part which interacts most with the optical mode, it is likely that this would reduce the coupling strength of these gratings significantly. The larger depth achieved using a single loop suggests that this is the most efficient way of milling these structures. One way of achieving the desired depth using this method would be to use a higher dose at the end of the scan, this may balance the achieved depth across the length of each grating gap.

7.5.3 Area Scanning Routine

The previous section showed that achieving the desired depths, particularly in the interior of the grating structure, was challenging when using the SPL scanning routine. Furthermore, achieving duty cycles close to 0.5 at the bottom of the milled structure was not possible due to the characteristic milling profile of the ion beam. Area scanning was investigated as a way of remedying these issues. Test structures with doses varying from $10\,000\ \mu\text{C}/\text{cm}^2$ to $100\,000\ \mu\text{C}/\text{cm}^2$ and gap widths of 50 nm and 100 nm were milled using gold ions, a single loop and imaged using SEM. Two examples of these structures are shown in Figure 7.5. Figure 7.5a shows a grating with a designed gap size of 50 nm milled using a longitudinal area scanning routine with a dose of $50\,000\ \mu\text{C}/\text{cm}^2$ and a dwell time of 0.42 ms. Figure 7.5b shows a grating with a designed gap size of 100 nm milled with a dose of $30\,000\ \mu\text{C}/\text{cm}^2$ and a dwell time of 0.25 ms. Although some control of the duty cycle was achieved and the interior of the gratings were cleared, significant damage to the milled area was observed. This damage was also observed to be more severe for the test structure with wider gaps. Increasing the number of loops may improve this, however, as has been shown in previous sections, the required dose is likely to be higher. For a grating with a 50 nm designed gap size, and an extrusion length of 500 nm, a dwell time of 0.25 ms gives a total time per tooth of 250 ms. The total dwell time required for a 300 μm DFB laser would therefore be around 10 mins. This patterning duration would not be suitable for wafer scale fabrication of DFB lasers, which may include over 100 000 devices. Different structures must therefore be considered that can be patterned in less time and do not exhibit the same level of damage to the areas surrounding the

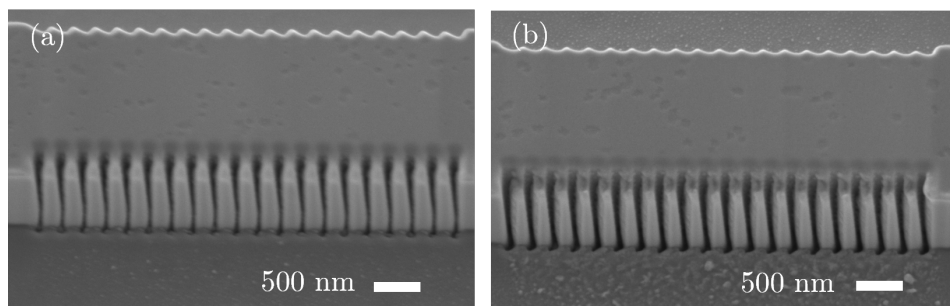


Figure 7.5: On ridge test structures milled with a single loop and (a) 50 nm designed gap size with a dose of $50\,000\ \mu\text{C}/\text{cm}^2$. (b) 100 nm gap size with a dose of $30\,000\ \mu\text{C}/\text{cm}^2$

milled structure.

7.6 Off-Ridge Grating Structures

The use of focused ion beam nanofabrication offers a major benefit that cannot be achieved with EBL currently. This is that patterning can be performed irrespective of the grating topography. For the LC-DFB laser, this means that the grating can be placed differently than would be permitted with conventional lithography techniques. As described earlier in this chapter, and shown in Figure 7.1, in this work the gratings have been placed adjacent to the RWG on the floor of the etched trench. Structures like this have been achieved previously using resist-based lithography [109]. However, multiple etch steps are required, which increases the fabrication complexity. The potential benefits of this type of structure include the fact that less milled depth is required to achieve reasonable coupling strength, since the floor of the etched trench is closer to the active region and optical mode. The following sections describe the design and process development undertaken to develop directly milled off-ridge grating structures.

7.6.1 Design and Simulation

In order to assess the achievable coupling strength values for the off-ridge grating structure, the simulation work described in chapter 3 was modified to describe the new structure. Figure 7.6a shows the cross section of the off-ridge structure. For the modelling work, two new parameters must be considered. These are the

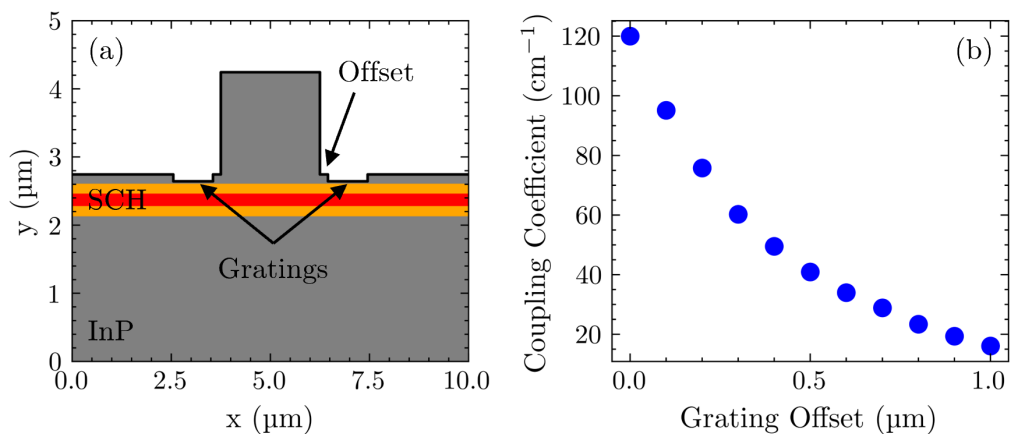


Figure 7.6: (a) cross section of the off-ridge LC-DFB structure. (b) coupling coefficient as a function of grating offset for a grating with an etch depth of 1.5 μm, a grating depth of 100 nm, a ridge width of 2 μm and a grating length of 500 nm.

grating offset, which describes the distance between the ridge waveguide and the grating in the x-direction, and the grating depth, which is the depth of the grating below the bottom of the ridge etched region. Figure 7.6b shows the coupling coefficient as a function of grating offset. For this modelling, the etch depth was $1.5\ \mu\text{m}$, the grating depth was $100\ \text{nm}$, the ridge width was $2\ \mu\text{m}$ and the length of the grating was $500\ \text{nm}$. Based on the modelling, with a relatively shallow grating depth, coupling values as high as $100\ \text{cm}^{-1}$ can be achieved for a 1st order grating, which would correspond to $\kappa L = 3$ for a $300\ \mu\text{m}$ cavity length. There are a number of advantages to this geometry. Firstly, the ridge etch depth, which can be challenging to control, is known before the gratings are defined. This means they can be tailored in response to the results of metrology. Secondly, control of the grating etch depth with the FIB is far more reliable than controlling the profile of an on-ridge structure etched using ICP-RIE. This means that fine control can be achieved by tuning the grating offset, this depends on FIB beam positioning which is accurate to less than $1\ \text{nm}$.

7.6.2 Single Pixel Line Scanning

The SPL scanning routine for off-ridge grating structure is described first. Figure 7.7a and b show the result of SPL scanning using bismuth ions with a single loop and 1000 loops respectively. The dose used for the single loop scan was $150\ \text{nC cm}$ and $264\ \text{nC cm}$ for the case where 1000 loops were used. For the single loop test structure, the grating gaps were milled with the beam moving away from

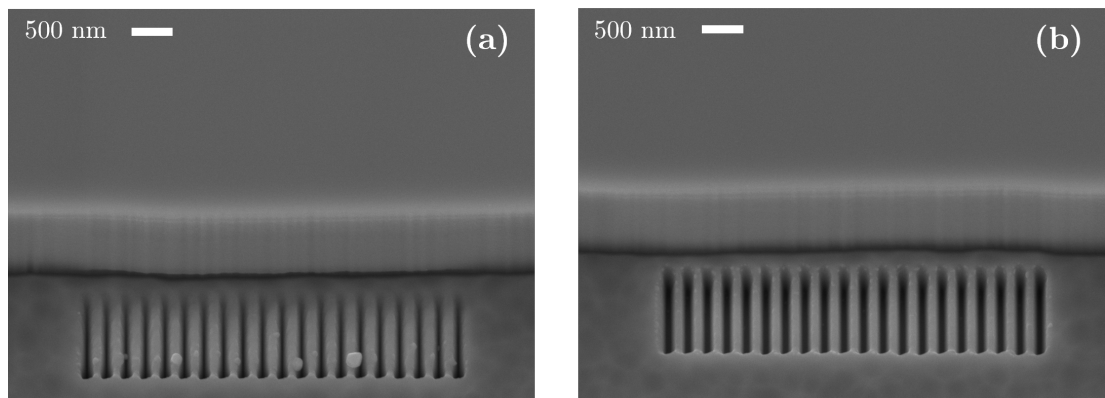


Figure 7.7: Off-ridge test structures milled using the SPL scanning routine and (a) A single loop with a dose of $150\ \text{nC cm}$ and (b) 1000 loops with a dose of $264\ \text{nC cm}$ [123].

the RWG. As a result the widest point is farthest away from the ridge because the area of the pattern milled last will be the least affected by the redeposition effect. The width at the top surface was measured to be (27 ± 5) nm at the narrowest point and (111 ± 5) nm at its widest point. Furthermore, large particles of redeposited material are present around the milled area. This redeposition effect is not observed in the test structure where 1000 loops have been used. This can be attributed to the fact that when a single loop is used, a higher dose is applied per pixel, leading to the removal of more material per beam shot. Large particles like this are undesirable on an optical structure as they may result in unwanted loss. Additionally, where 1000 loops have been used, the gap size appears wider and more uniform, suggesting some control over the duty cycle can be achieved by varying the number of loops. Although not shown, the same effect was observed when using gold ions to mill these structures. This is shown in Figure 7.8, which presents the gap size as a function of number of loops when milling using gold ions. An increase in the gap size with the number of loops was observed until 100 loops, where the gap size stabilises. Adjusting the loops in this way offers the ability to control the duty cycle from around 0.55 to 0.8. The error bars indicate the standard deviation across all measurements taken for each grating. Notably, measurements were taken at different points across the width of the grating structure. Therefore, the higher standard deviation observed for

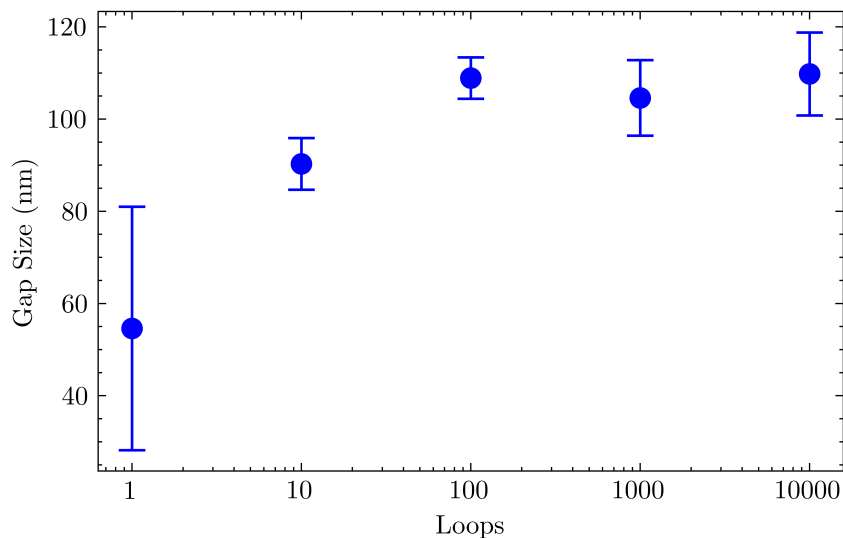


Figure 7.8: Gap size as a function of number of loops using gold ions with a dose of 150 nC cm and an SPL scanning routine [123].

the single loop grating structures indicates a high degree of variability in the gap size across the width of the grating, as shown in Figure 7.7a.

7.6.3 Area Scanning

Off-ridge test structures were also milled using an area scanning routine. An example of this is shown in Figure 7.9, which shows a test structure milled with a longitudinal area scan with a dose of $52\,800\ \mu\text{C}/\text{cm}^2$ and a dwell time of $0.5\ \mu\text{s}$ per pixel per loop. The designed gap size of the grating was $50\ \text{nm}$, which produced an actual milled gap width of $(153 \pm 11)\ \text{nm}$. This value corresponds to a duty cycle of 0.46 , close to the desired value of 0.5 .

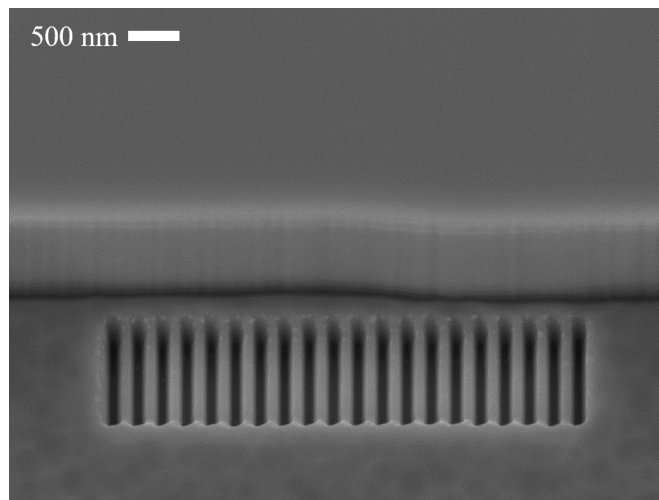


Figure 7.9: Off-ridge test grating structure milled with a dose of $52\,800\ \mu\text{C}/\text{cm}^2$

7.6.4 Off-Ridge Grating Cross Sections

The previous sections have presented both ways of remedying the redeposition effects resulting from FIB nanofabrication as well ways of reaching the desired duty cycle value of 0.5 . The closest portion of the grating is that which is nearest the active region, however, which in this case is subsurface at the bottom of the grating structure. Cross sections were taken on a series of test gratings with varying dose for the SPL, longitudinal and area scanning routines. Prior to cross sectioning, a protective platinum layer was deposited using the gas injection system in the Raith Velion. Three examples of these cross sections are shown in Figure 7.10. Figure 7.10a shows a test grating milled with the SPL scanning routine and a dose of $120\ \text{nC}/\text{cm}$ and a single loop. The depth achieved using this

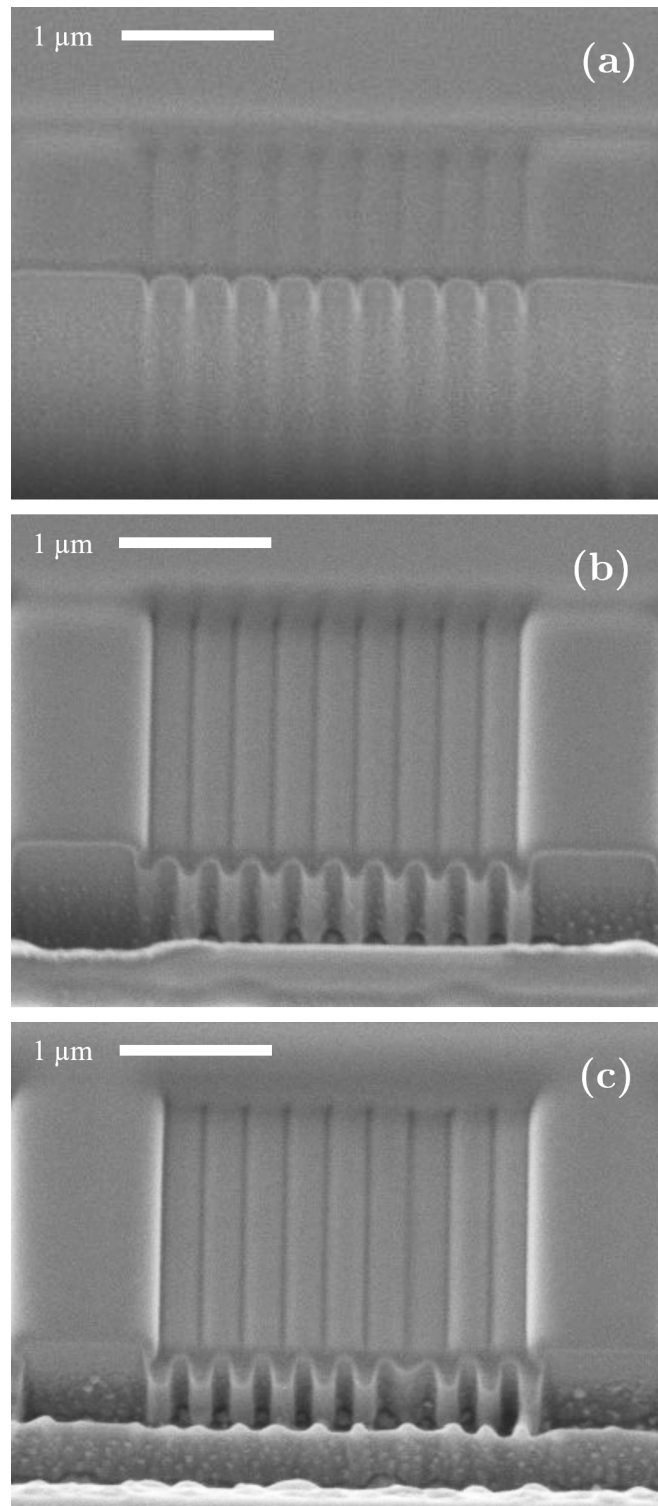


Figure 7.10: Cross sections of off-ridge test structures. (a) SPL with dose of 120 nC/cm. (b) longitudinal with a dose of 120 000 $\mu\text{C}/\text{cm}^2$. (c) concentric with a dose of 120 000 $\mu\text{C}/\text{cm}^2$ [123].

method was (432 ± 9) nm, however, the duty cycle was found to be very high at the bottom of the structure and non-uniform across the whole grating. In particular, the gap size was measured as (102 ± 9) nm and (54 ± 5) nm at the top and bottom of the grating structure respectively, corresponding to duty cycle values of 0.55 and 0.7. This level of variability in the duty cycle would make the coupling coefficient difficult to predict and filling the narrow gaps at the bottom of the trench with dielectric would be challenging. Test structures using area scanning routines with a dose of $52\,800 \mu\text{C}/\text{cm}^2$ are shown in Figure 7.10b (longitudinal) and 7.10c (concentric). The area scans appear to deliver profiles closer to the desired values. In both cases the gap size was designed at 50 nm and the number of loops was 100 with a dwell time of $10 \mu\text{s}$ per pixel per loop. Where the longitudinal scan was used, the depth was measured to be (280 ± 4) nm and for the concentric scan the milled depth was (378 ± 5) nm. Additionally, the sidewall angles were measured to be 30° and 18° for the longitudinal and concentric methods, respectively. From these results it appeared that the concentric scanning routine was milling the structures more efficiently, as a greater depth was achieved using the same dose. Figure 7.11 describes this further, showing the milled depth as a function of dose. Control over the depth is achieved from less than 100 nm to over 300 nm. Smaller milling depths might be achievable but cross sections were not observed for dose values lower than $60\,000 \mu\text{C}/\text{cm}^2$, most likely due to the cross-sectioning

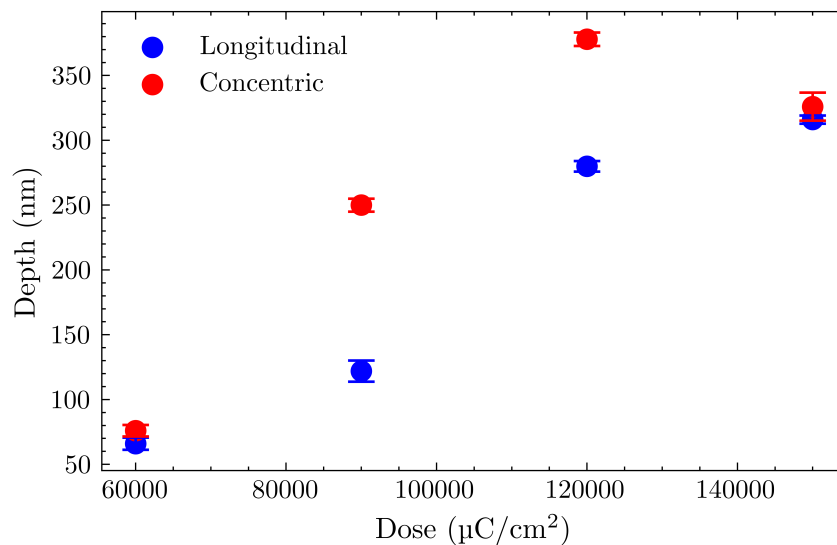


Figure 7.11: Milled depth as a function of dose for off-ridge test structures milled using longitudinal and concentric scanning routines.

procedure. Greater depths are achieved for the same dose when using concentric scanning for middle doses, however, similar depths are achieved at the highest dose value of $150\,000\ \mu\text{C}/\text{cm}^2$. This is likely due to overall damage of the milled area reducing the grating depth at these high dose values. The coupling coefficient for a grating milled using a dose of $60\,000\ \mu\text{C}/\text{cm}^2$ assuming a ridge width of $2\ \mu\text{m}$, etch depth of $1.5\ \mu\text{m}$ and an offset of $100\ \text{nm}$, is estimate to be $73\ \text{cm}^{-1}$. This value would provide a $\kappa L = 2.2$ for a grating with a length of $300\ \mu\text{m}$. Using the method described above, the patterning time for this grating structure would be 20 mins. Once again, this is too high for large scale wafer fabrication. In a situation where a wafer contained relatively less grating area, such as in a PIC, however, this patterning time may not be as much of an issue. This would be especially true if direct milling was the only way that high coupling strength gratings could be fabricated without the need for regrowth. Methods for reducing patterning time will be discussed in the final chapter of this work.

7.7 Summary

This chapter has described the process development for the fabrication of 1st order LC-DFB grating structures using bismuth and gold FIBs. Two types of structure were investigated, on-ridge and off-ridge LC-DFB structures.

In the case of the on-ridge gratings, it was shown that increasing the number of loops resulted in less efficient milling due to the fact that the benefit of milling against topography was lost. Additionally, when using the SPL scanning routine for these structures, it was found that milling through the entire ridge was challenging due to redeposition effects and the high aspect ratio of the structures. Using area scanning methods limited this issue to some extent, however, significant damage was observed on the top of the ridge when using this method.

The off-ridge grating structure was also presented and the fabrication of this structure was found to be simpler. Among the three scanning routines used in this work, the concentric area scanning method was shown to be optimal, producing higher milling depths for the same dose as the longitudinal area scanning routine as well as more vertical sidewalls. This resulted in grating structures that would provide coupling strengths sufficient for a $kL = 2.2$ for a $300\ \mu\text{m}$ cavity length DFB laser.

Although the task of producing fabrication tolerant first order LC-DFB gratings has been achieved, the patterning time for these structures is likely too high for wafer scale DFB laser fabrication. For applications such as PICs, where relatively few gratings are required, however, this method offers an attractive method for fabricating regrowth-free 1st order gratings.

Chapter 8

Conclusions and Future Work

8.1 Conclusions

In this work, the design, fabrication and materials for DFB lasers targeting the c-band were investigated. Firstly, the use of projection lithography in the fabrication of high-order LC-DFB lasers was presented. Secondly, a comparison between varying order LC-DFBs was made and the performance of LC-DFB lasers on different material systems was compared. Finally, the fabrication of 1st order gratings was discussed using bismuth and gold focused ion beams.

An 11th order LC-DFB laser fabricated with projection lithography was demonstrated. The fabrication process involved a two-step lithography and mask deposition process to define the grating structure. This fabrication technique was found to deliver sharp grating features, however, significant variability in both the pitch and duty cycle was observed across the whole sample. This was attributed to variations in the depth of focus in the projection lithography system, altering the dose at the edge of grating features. Furthermore, the width of the central ridge portion of the structure was found to be widened significantly, as a result of the angled substrate holder used in the deposition of the mask. Despite these issues, single mode lasing was observed under pulsed current operation and SMSR values of 25 dB were observed. Comparison of the DFB device with a conventional RWG FP device revealed a reduced temperature shift in the wavelength, which was 0.1 nm K^{-1} for the DFB laser and 0.6 nm K^{-1} for the FP device. The spectral performance of the DFB laser, however, was found to be limited by the existence

of multiple lateral modes caused by the widened central ridge. Overall, this work demonstrated another method of fabricating LC-DFB lasers without the need for expensive high resolution techniques such as electron beam lithography, although optimisation of the fabrication process should be undertaken.

A comparison of 1st, 3rd and 11th order LC-DFB lasers has also been undertaken. The lithography process development was presented and it was found that dilution of AZ2020 negative tone photoresist was adequate for the patterning of all three types of grating. Following the etching process, however, it was observed that the effects of ARDE were significant for the 1st order grating structures. Although not as severe in the 3rd and 11th order devices, a reduction in coupling coefficient from the designed values was observed as a result of both the etch profile and insufficient etch depth. Due to the etch issues, single mode lasing was not observed in the 1st order devices. Single mode lasing was, however, observed for the 3rd and 11th order devices and a comparison of their device characteristics was performed. The threshold current density was observed to be similar between the different grating orders, however, a significant reduction in slope efficiency was observed for the 11th order devices. This was attributed to diffraction loss introduced by the use of a high order grating. Despite this, spectral measurements revealed SMSR values exceeding 53 dB for the 11th order devices significantly larger than the maximum value achieved for the 3rd order devices, which was 42 dB. This discrepancy may be either a result of radiation modes initiating loss at undesired wavelengths or reduced coupling strength values in the 3rd order devices.

A comparison of 11th order LC-DFB lasers on QW and QD material was also performed. The QD devices did not exhibit lasing above a temperature of 250 K under CW operation. Comparisons of threshold current density between pulsed and CW current operation revealed that the level of self-heating in both materials was similar. It was noted, however, that the device on the QD material was more sensitive to temperature change, as both the threshold current density and slope efficiency changed more rapidly with temperature than the QW device. Comparison of the spectral performance of the devices initially involved the measurement of sub-threshold spectral measurements. These were then used to calculate the gain spectra with the Cassidy method. The gain spectrum width for each device at a value of 0 cm^{-1} was measured. This value was found to be $(26 \pm 3) \text{ nm}$ for the device on the QD material and $(7 \pm 1) \text{ nm}$ for the device on the

QW material. This result was evidence of a broadened gain spectrum as a result of inhomogeneous size broadening. The effect of this on the spectral performance was also assessed through the measurement of the peak wavelength and SMSR as a function of temperature and current. Similar peak SMSR values were achieved exceeding 40 dB. Furthermore, a wider range of DFB operating temperature and current was observed in the QD device. Specifically, the temperature range for the device on the QD material was measured to be 55 K and 30 K for the QW device. These results further highlight the promise of a wider accessible wavelength range from MOCVD grown QD material.

Finally, chapter 7 described the process optimisation of direct milling of 1st order grating structures using bismuth and gold focused ion beams. The suitability of the method in the patterning of on-ridge and off-ridge LC-DFB architectures was compared as well as different scanning routines. The SPL scanning routine was found to be most effective for on-ridge grating designs, due to the efficiency benefits of milling against the topography. In general, however, the high aspect ratio of the structure made complete milling through the RWG challenging due to the redeposition effect. For the off-ridge grating structures, the direct milling approach was found to be effective at achieving controllable grating structures with desirable profiles. The concentric area scanning routine was found to be most effective and it resulted in grating structures that were estimated to have coupling strengths exceeding $\kappa L = 2$ for device lengths of 300 μm . This work demonstrates the potential of using FIB in the definition of structures independent of sample topography. This method would be suitable in the fabrication of PICs where the grating area is limited. For larger-scale DFB laser fabrication, however, methods of reducing patterning time are worth pursuing.

8.2 Future Work

The results of this work have generated several avenues for future research. These areas are itemised and described below.

8.2.1 High Order LC-DFB Lasers

Chapter 6 in this work demonstrated the potential of high order DFB lasers for providing high spectral purity even with as-cleaved facets. Chapter 5 also demonstrated that these devices may be fabricated with conventional photolithography. Further development of this concept, particularly the two-step lithographic process, to bring the performance of the devices fabricated with photolithography closer to the electron beam lithography devices is worth undertaking. Optimising the focusing optics of the projection system used in this work to remove the variance observed in pitch and duty cycle is essential for the scale up of this technology. Furthermore, the use of other photolithography techniques such as contact lithography with a mask aligner may remedy the fabrication issues. Additionally, the minimum cavity length for these devices demonstrated here was $700\ \mu\text{m}$. This may be suitable for applications where the device is not to be directly modulated, such as where it is integrated with an electro absorption modulator [126], as well as gas sensing applications which utilise wavelengths of $1.57\ \mu\text{m}$ [127, 128]. Future work should aim to decrease this cavity length with the view to achieving direct modulation, where short cavity lengths are required. This involves increasing the coupling strength of these devices, which may be achieved through further optimisation of the etch depth, duty cycle and ridge width.

8.2.2 1st Order LC-DFB Lasers

The challenge of fabricating 1st order LC-DFB lasers on the InP material system has been highlighted in this work. This challenge is mainly associated with the effects of ARDE during the epitaxial etch process. In this work, a Cl_2/Ar chemistry was used to etch the structures. Recent work has demonstrated the successful implementation of 1st order laterally coupled grating structures [50, 129, 130]. The etch chemistries used in these examples involved the addition of H_2 , which is chosen due to its surface passivation effect [131], although they do still report

a reduction in coupling strength due to ARDE. One method to limit the effect of ARDE may be to reduce the extrusion length of the grating structure. This would potentially allow easier entrance and extraction of the etchants/products, limiting the effect of ARDE. The issue with this method is that it places a limit on the achievable coupling strength, potentially limiting how short the cavity length can be. Further improvements could also be made with regards to etching through the use of an etch stop layer in the epitaxial structure. This would remedy the high degree of variability in the coupling strength at etch depths just above the active region to some extent, which was described in chapter 3 of this work.

8.2.3 FIB Device Processing

This thesis has demonstrated the flexibility of using FIB nanofabrication to pattern LC-DFB laser gratings. Future work in this field should focus on reducing the patterning time, which is the main limitation in the adoption of FIB for larger scale fabrication runs. A promising area of research that may be undertaken is the use of FIB to mill a mask for a subsequent dry etch step. The off-ridge grating structure described in chapter 7 lends itself well to this technique. An example process would be that the ridge lithography and etch is carried out as normal. This would then be followed by the deposition of a thin mask, likely using atomic layer deposition (ALD). The grating structures could then be patterned into the mask and etched into the InP using a conventional grating dry etch. Since the required grating depth is relatively shallow at around 100 nm, ARDE effects would not be as prevalent. This methodology could be expanded further through the use of a mask stack. For example, SiO₂ could be used as the mask for the grating etch, with an Al or AlN used as a mask for the SiO₂. The upper mask may only need to be a few nm thick as the selectivity of both Al and AlN is known to be high [132].

8.2.4 QD DFB Laser Development

The final avenue of future work that will be described here is the development of MOCVD grown QD DFB lasers. This thesis has demonstrated the potential for a greater range of accessible wavelengths using the InAs/InAlGaAs QDs. The devices, however, did not lase above 250 K under CW conditions. Therefore, whilst

the development of DFB lasers and WDM transmitter systems is worthwhile, this should be undertaken once the growth is mature enough to provide operation of RWG lasers at elevated temperature.

Bibliography

1. Coldren, L. A., Corzine, S. W. & Mashanovitch, M. *Diode lasers and photonic integrated circuits* 2nd ed. *Wiley series in microwave and optical engineering* **218** (Wiley, Hoboken, N.J, 2012).
2. Selmic, S. *et al.* Design and characterization of 1.3- μm AlGaInAs-InP multiple-quantum-well lasers. *IEEE Journal of Selected Topics in Quantum Electronics* **7**, 340–349 (2001).
3. Keiser, G. E. A Review of WDM Technology and Applications. *Optical Fiber Technology* **5**, 3–39 (1999).
4. Wemple, S. H. Material dispersion in optical fibers. *Applied Optics* **18**, 31 (1979).
5. Cho, J. *et al.* Trans-Atlantic Field Trial Using High Spectral Efficiency Probabilistically Shaped 64-QAM and Single-Carrier Real-Time 250-Gb/s 16-QAM. *Journal of Lightwave Technology* **36**, 103–113 (2018).
6. Bowers, J. E. & Liu, A. Y. *A comparison of four approaches to photonic integration* in *2017 Optical Fiber Communications Conference and Exhibition (OFC)* (2017), 1–3.
7. Smit, M. *et al.* An introduction to InP-based generic integration technology. *Semiconductor Science and Technology* **29**. Publisher: IOP Publishing, 083001 (2014).
8. Debackere, P *et al.* *Recent Trends in the Manufacturing of InP Photonic Integrated Circuits* in (New Orleans, 2025).
9. Neamen, D. A. *Semiconductor physics and devices: basic principles* 3. ed (McGraw-Hill, New York, 2003).
10. Grillot, F. *Advanced Semiconductor Lasers* 2010.
11. Blood, P. *Quantum confined laser devices: optical gain and recombination in semiconductors* First edition. *Oxford master series in physics. Atomic,*

- optical, and laser physics* **23**. OCLC: ocn930017961 (Oxford University Press, Oxford, 2015).
12. Hayashi, I., Panish, M. B., Foy, P. W. & Sumski, S. JUNCTION LASERS WHICH OPERATE CONTINUOUSLY AT ROOM TEMPERATURE. *Applied Physics Letters* **17**, 109–111 (1970).
 13. Panish, M., Casey, H., Sumski, S. & Foy, P. Reduction of threshold current density in GaAs–Al x Ga $1-x$ As heterostructure lasers by separate optical and carrier confinement. *Applied Physics Letters* **22**, 590–591 (1973).
 14. Thompson, G. & Kirkby, P. (GaAl)As lasers with a heterostructure for optical confinement and additional heterojunctions for extreme carrier confinement. *IEEE Journal of Quantum Electronics* **9**, 311–318 (1973).
 15. Kawaguchi, H. & Kawakami, T. Transverse-mode control in an injection laser by a strip-loaded waveguide. *IEEE Journal of Quantum Electronics* **13**, 556–560 (1977).
 16. Tsukada, T. GaAs–Ga $1-x$ Al x As buried-heterostructure injection lasers. *Journal of Applied Physics* **45**, 4899–4906 (1974).
 17. Kogelnik, H. & Shank, C. V. Coupled-Wave Theory of Distributed Feedback Lasers. *Journal of Applied Physics* **43**, 2327–2335 (1972).
 18. Kogelnik, H. & Shank, C. V. Stimulated Emission in a Periodic Structure. *Applied Physics Letters* **18**, 152–154 (1971).
 19. Yamada, M. & Sakuda, K. Analysis of almost-periodic distributed feedback slab waveguides via a fundamental matrix approach. *Applied Optics* **26**, 3474 (1987).
 20. Numai, T. *Fundamentals of semiconductor lasers Springer series in optical sciences* **93** (Springer, New York, 2004).
 21. Streifer, W., Burnham, R. & Scifres, D. Radiation losses in distributed feedback lasers and longitudinal mode selection. *IEEE Journal of Quantum Electronics* **12**, 737–739 (1976).
 22. Matsuoka, T., Yoshikuni, Y. & Nagai, H. Verification of the light phase effect at the facet on DFB laser properties. *IEEE Journal of Quantum Electronics* **21**, 1880–1886 (1985).
 23. Yoffe, G., Zou, S., Pezeshki, B., Rishton, S. & Emanuel, M. High-Precision High-Yield Laser Source Using DFB Array. *IEEE Photonics Technology Letters* **16**, 735–737 (2004).

24. Pezeshki, B. *et al.* 20-mW widely tunable laser module using DFB array and MEMS selection. *IEEE Photonics Technology Letters* **14**, 1457–1459 (2002).
25. Soda, H. *et al.* Stability in single longitudinal mode operation in GaInAsP/InP phase-adjusted DFB lasers. *IEEE Journal of Quantum Electronics* **23**, 804–814 (1987).
26. Carroll, J. E., Whiteaway, J. & Plumb, D. *Distributed feedback semiconductor lasers SPIE Press monograph 52* (Institution of Electrical Engineers SPIE Optical Engineering Press, London, 1998).
27. Zory, P. & Comerford, L. Grating-coupled double-heterostructure AlGaAs diode lasers. *IEEE Journal of Quantum Electronics* **11**, 451–457 (1975).
28. Miller, L. *et al.* A distributed feedback ridge waveguide quantum well heterostructure laser. *IEEE Photonics Technology Letters* **3**, 6–8 (1991).
29. Martin, R. *et al.* CW performance of an InGaAs-GaAs-AlGaAs laterally-coupled distributed feedback (LC-DFB) ridge laser diode. *IEEE Photonics Technology Letters* **7**, 244–246 (1995).
30. Chen, N., Watanabe, Y., Takei, K. & Chikuma, K. InGaAsP/InP Laterally Coupled Distributed Feedback Ridge Laser. *Japanese Journal of Applied Physics* **39**. Publisher: IOP Publishing, 1508 (2000).
31. Kamp, M., Hofmann, J., Forchel, A., Schäfer, F. & Reithmaier, J. P. Low-threshold high-quantum-efficiency laterally gain-coupled InGaAs/AlGaAs distributed feedback lasers. *Applied Physics Letters* **74**. Publisher: AIP Publishing, 483–485 (1999).
32. Zeller, W. *et al.* DFB Lasers Between 760 nm and 16 μm for Sensing Applications. *Sensors* **10**. Publisher: MDPI AG, 2492–2510 (2010).
33. Jian Wang *et al.* 1.55- μm /m AlGaInAs-InP laterally coupled distributed feedback laser. *IEEE Photonics Technology Letters* **17**. Publisher: Institute of Electrical and Electronics Engineers (IEEE), 1372–1374 (2005).
34. Li, J. & Cheng, J. A laterally-coupled distributed feedback laser with equivalent quarter-wave phase shift. *Optics Express* **21**, 26936 (2013).
35. Viheriälä, J. *et al.* Applications of UV-nanoimprint soft stamps in fabrication of single-frequency diode lasers. *Microelectronic Engineering* **86**, 321–324 (2009).

36. Dridi, K., Benhsaien, A., Zhang, J. & Hall, T. *1.55 μ m laterally coupled ridge-waveguide DFB lasers with third-order surface grating* in (ed Kieffer, J.-C.) (Montreal, Canada, 2012), 84121R.
37. Millett, R. *et al.* Fabrication-tolerant 1310 nm laterally coupled distributed feedback lasers with high side mode suppression ratios. *Photonics and Nanostructures - Fundamentals and Applications. Emerging Trends and Novel Materials in Photonics* **9**, 111–118 (2011).
38. Laakso, A. *et al.* Optical modeling of laterally-corrugated ridge-waveguide gratings. *Optical and Quantum Electronics* **40**, 907–920 (2008).
39. Fricke, J, Wenzel, H, Matalla, M, Klehr, A & Erbert, G. 980-nm DBR lasers using higher order gratings defined by i-line lithography. *Semiconductor Science and Technology* **20**, 1149–1152 (2005).
40. Slight, T. J. *et al.* Continuous-wave operation of (Al,In)GaN distributed-feedback laser diodes with high-order notched gratings. *Applied Physics Express* **11**. Publisher: IOP Publishing, 112701 (2018).
41. Teng, J. H. *et al.* Self-aligned metal-contact and passivation technique for submicron ridge waveguide laser fabrication. *Journal of Vacuum Science & Technology B: Microelectronics and Nanometer Structures Processing, Measurement, and Phenomena* **26**, 1748–1752 (2008).
42. Kim, H. *et al.* Dark current reduction in APD with BCB passivation. *Electronics Letters* **37**, 455–457 (2001).
43. Liu, Q., Chiang, K. S., Reekie, L. & Chow, Y. T. CO₂ laser induced refractive index changes in optical polymers. *Optics Express* **20**, 576 (2012).
44. Streifer, W., Scifres, D. & Burnham, R. Coupling coefficients for distributed feedback single- and double-heterostructure diode lasers. *IEEE Journal of Quantum Electronics* **11**. Conference Name: IEEE Journal of Quantum Electronics, 867–873 (1975).
45. Millett, R. R., Hinzer, K., Hall, T. J. & Schriemer, H. Simulation Analysis of Higher Order Laterally-Coupled Distributed Feedback Lasers. *IEEE Journal of Quantum Electronics* **44**, 1145–1151 (2008).
46. Design, P. *Fimmwave, Version 7.2* 2021.
47. Yoo, B.-S., Park, S.-J. & Park, K.-H. Reactive ion etching-induced damage in GaAs/AlGaAs quantum well structures and recovery by rapid thermal annealing and hydrogen passivation. *Journal of Vacuum Science & Technology A: Vacuum, Surfaces, and Films* **13**, 931–934 (1995).

48. David, K. *et al.* Gain-coupled DFB lasers versus index-coupled and phase shifted DFB lasers: a comparison based on spatial hole burning corrected yield. *IEEE Journal of Quantum Electronics* **27**, 1714–1723 (1991).
49. Kaneko, R. *et al.* 1550 nm-Band InAs/InGaAlAs Quantum Dot Distributed Feedback Lasers Grown on InP(311)B Substrate with Side-Wall Gratings Simultaneously Fabricated with a Ridge Waveguide. *physica status solidi (a)* **219**, 2100453 (2022).
50. Ye, S. *et al.* 1.55- μ m Sidewall Grating DFB Lasers Integrated With a Waveguide Crossing for an Optical Beam Forming Network. *IEEE Photonics Technology Letters* **35**. Conference Name: IEEE Photonics Technology Letters, 785–788 (2023).
51. Williams, R. E. *Gallium arsenide processing techniques* (Artech House, Dedham, MA, 1984).
52. Guivarc’h, A., L’Haridon, H., Pelous, G., Hollinger, G. & Pertosa, P. Chemical cleaning of InP surfaces: Oxide composition and electrical properties. *Journal of Applied Physics* **55**, 1139–1148 (1984).
53. Rebaud, M. *et al.* Chemical Treatments for Native Oxides Removal of GaAs Wafers. *ECS Meeting Abstracts MA2015-02*. Publisher: IOP Publishing, 1048 (2015).
54. Franssila, S. in *Introduction to Microfabrication* (Wiley, 2004).
55. Menon, R., Patel, A., Gil, D. & Smith, H. I. Maskless lithography. *Materials Today* **8**, 26–33 (2005).
56. Sandstrom, T. *et al.* *OML: optical maskless lithography for economic design prototyping and small-volume production* in (ed Smith, B. W.) (Santa Clara, CA, 2004), 777.
57. Belokopytov, G. V. & Ryzhkova, Y. V. Optical maskless lithography. *Russian Microelectronics* **40**, 414–427 (2011).
58. McCord, M. A. & Rooks, M. J. Electron Beam Lithography. **PM39**. Publisher: SPIE, 139–250 (1997).
59. Hofmann, U. *Electron Scattering and Proximity Effect* Webinar. Munich, 2020.
60. Arshak, K., Mihov, M., Arshak, A., McDonagh, D. & Sutton, D. *Focused ion beam lithography-overview and new approaches in 2004 24th International Conference on Microelectronics (IEEE Cat. No.04TH8716)* **2** (IEEE, Nis, Serbia, 2004), 459–462.

61. Recht, D. & Yao, N. in *Focused Ion Beam Systems* (ed Yao, N.) 1st ed., 318–336 (Cambridge University Press, 2007).
62. Puretz, J. & Swanson, L. W. Focused ion beam deposition of Pt containing films. *Journal of Vacuum Science & Technology B: Microelectronics and Nanometer Structures Processing, Measurement, and Phenomena* **10**, 2695–2698 (1992).
63. Huff, M. Recent Advances in Reactive Ion Etching and Applications of High-Aspect-Ratio Microfabrication. *Micromachines* **12**, 991 (2021).
64. Racka-Szmidt, K., Stonio, B., Żelazko, J., Filipiak, M. & Sochacki, M. A Review: Inductively Coupled Plasma Reactive Ion Etching of Silicon Carbide. *Materials* **15**, 123 (2021).
65. Booker, K., Mayon, Y. O., Jones, C., Stocks, M. & Blakers, A. Deep, vertical etching for GaAs using inductively coupled plasma/reactive ion etching. *Journal of Vacuum Science & Technology B, Nanotechnology and Microelectronics: Materials, Processing, Measurement, and Phenomena* **38**, 012206 (2020).
66. Donnelly, V. M., Flamm, D. L. & Ibbotson, D. E. Plasma etching of III-V compound semiconductors. *Journal of Vacuum Science & Technology A: Vacuum, Surfaces, and Films* **1**, 626–628 (1983).
67. Bothra, S., Kellam, M. & Garrou, P. Feasibility of BCB as an interlevel dielectric in integrated circuits. *Journal of Electronic Materials* **23**, 819–825 (1994).
68. Ivey, D. G., Wang, D., Yang, D., Bruce, R. & Knight, G. Au/Ge/Ni ohmic contacts to n-Type InP. *Journal of Electronic Materials* **23**, 441–446 (1994).
69. Simon, A. H. in *Handbook of Thin Film Deposition* 93–140 (Elsevier, 2025).
70. Erdman, N., Bell, D. C. & Reichelt, R. in *Springer Handbook of Microscopy* (eds Hawkes, P. W. & Spence, J. C. H.) Series Title: Springer Handbooks, 229–318 (Springer International Publishing, Cham, 2019).
71. Mobarhan, K. S. *Application Note 1: Test and Characterization of Laser Diodes: Determination and Principal Parameters*
72. Kihara, K., Soda, H., Ishikawa, H. & Imai, H. Evaluation of the coupling coefficient of a distributed feedback laser with residual facet reflectivity. *Journal of Applied Physics* **62**, 1526–1527 (1987).

73. Jeong, J. *Application Note 12: Near Field Imaging of a Laser Diode Using Scanning Method*
74. Jarvis, L. K. *Active region doping strategies in O-band InAs/GaAs quantum-dot lasers* PhD thesis (Cardiff University, Cardiff, UK, 2022).
75. Smowton, P. M., Pearce, E. J., Schneider, H. C., Chow, W. W. & Hopkinson, M. Filamentation and linewidth enhancement factor in InGaAs quantum dot lasers. *Applied Physics Letters* **81**, 3251–3253 (2002).
76. Partovi, A. *et al.* High-power laser light source for near-field optics and its application to high-density optical data storage. *Applied Physics Letters* **75**, 1515–1517 (1999).
77. Hakki, B. W. & Paoli, T. L. Gain spectra in GaAs doubleheterostructure injection lasers. *Journal of Applied Physics* **46**, 1299–1306 (1975).
78. Cassidy, D. T. Technique for measurement of the gain spectra of semiconductor diode lasers. *Journal of Applied Physics* **56**, 3096–3099 (1984).
79. Wang, H. & Cassidy, D. Gain measurements of Fabry-Pe/spl acute/rot semiconductor lasers using a nonlinear least-squares fitting method. *IEEE Journal of Quantum Electronics* **41**. Conference Name: IEEE Journal of Quantum Electronics, 532–540 (2005).
80. Blood, P. *et al.* Characterization of semiconductor laser gain media by the segmented contact method. *IEEE Journal of Selected Topics in Quantum Electronics* **9**, 1275–1282 (2003).
81. Chou, S. Y., Krauss, P. R. & Renstrom, P. J. Nanoimprint lithography. *Journal of Vacuum Science & Technology B: Microelectronics and Nanometer Structures Processing, Measurement, and Phenomena* **14**, 4129–4133 (1996).
82. Haring, K. *et al.* Laterally-coupled distributed feedback InGaSb/GaSb diode lasers fabricated by nanoimprint lithography. *Electronics Letters* **46**, 1146 (2010).
83. Guan, T. *et al.* Toward Defect-Free Nanoimprinting. *Small*, 2312254 (2024).
84. Li, N., Wu, W. & Chou, S. Y. Sub-20-nm Alignment in Nanoimprint Lithography Using Moiré Fringe. *Nano Letters* **6**, 2626–2629 (2006).
85. Li, F. *et al.* Pattern distortion in nanoimprint lithography using UV-curable polymer stamps. *Micro and Nano Engineering* **25**, 100293 (2024).
86. Bjorkholm, J. E. & Shank, C. V. Higher-Order Distributed Feedback Oscillators. *Applied Physics Letters* **20**, 306–308 (1972).

87. Telkkälä, J. *et al.* Narrow linewidth laterally-coupled 1.55 μm DFB lasers fabricated using nanoimprint lithography. *Electronics Letters* **47**, 400 (2011).
88. Huard, C. M., Zhang, Y., Sriraman, S., Paterson, A. & Kushner, M. J. Role of neutral transport in aspect ratio dependent plasma etching of three-dimensional features. *Journal of Vacuum Science & Technology A* **35**, 05C301 (2017).
89. Wang, Y., Yang, Y., Zhang, S., Wang, L. & He, J.-J. Narrow Linewidth Single-Mode Slotted Fabry–Pérot Laser Using Deep Etched Trenches. *IEEE Photonics Technology Letters* **24**, 1233–1235 (2012).
90. Stoffels, W. W., Stoffels, E. & Tachibana, K. Polymerization of fluorocarbons in reactive ion etching plasmas. *Journal of Vacuum Science & Technology A: Vacuum, Surfaces, and Films* **16**, 87–95 (1998).
91. Kazarinov, R. F. & Suris, R. A. Injection Heterojunction Laser with a diffraction grating on its Contact Surface. *Soviet Physics - Semiconductors* **6**, 1184–1189 (1973).
92. Kazarinov, R. & Henry, C. Second-order distributed feedback lasers with mode selection provided by first-order radiation losses. *IEEE Journal of Quantum Electronics* **21**, 144–150 (1985).
93. Deppe, D., Shavritranuruk, K., Ozgur, G., Chen, H. & Freisem, S. Quantum dot laser diode with low threshold and low internal loss. *Electronics Letters* **45**, 54 (2009).
94. Perret, N. *et al.* Origin of the inhomogeneous broadening and alloy intermixing in InAs/GaAs self-assembled quantum dots. *Physical Review B* **62**, 5092–5099 (2000).
95. Wan, Y., Norman, J., Liu, S., Liu, A. & Bowers, J. E. Quantum Dot Lasers and Amplifiers on Silicon: Recent Advances and Future Developments. *IEEE Nanotechnology Magazine* **15**. Conference Name: IEEE Nanotechnology Magazine, 8–22 (2021).
96. Li, Q. *et al.* Development of Modulation p-Doped 1310 nm InAs/GaAs Quantum Dot Laser Materials and Ultrashort Cavity Fabry–Pérot and Distributed-Feedback Laser Diodes. *ACS Photonics* **5**, 1084–1093 (2018).
97. Wang, Y. *et al.* Monolithic quantum-dot distributed feedback laser array on silicon. *Optica* **5**, 528 (2018).

98. Brault, J. *et al.* Surface effects on shape, self-organization and photoluminescence of InAs islands grown on InAlAs/InP(001). *Journal of Applied Physics* **92**, 506–510 (2002).
99. Gready, D. *et al.* High Speed 1.55 μm InAs/InGaAlAs/InP Quantum Dot Lasers. *IEEE Photonics Technology Letters* **26**. Conference Name: IEEE Photonics Technology Letters, 11–13 (2014).
100. Veerabathran, G. K. *et al.* Transient thermal analysis of semiconductor diode lasers under pulsed operation. *AIP Advances* **7**, 025208 (2017).
101. Karouta, F. A practical approach to reactive ion etching. *Journal of Physics D: Applied Physics* **47**, 233501 (2014).
102. Nishi, K., Takemasa, K., Sugawara, M. & Arakawa, Y. Development of Quantum Dot Lasers for Data-Com and Silicon Photonics Applications. *IEEE Journal of Selected Topics in Quantum Electronics* **23**, 1–7 (2017).
103. Banyoudeh, S. & Reithmaier, J. P. High-density 1.54 μm InAs/InGaAlAs/InP(100) based quantum dots with reduced size inhomogeneity. *Journal of Crystal Growth* **425**, 299–302 (2015).
104. Khatri, V. *et al.* Increased Modal Gain in 1.55 μm Quantum Dot Lasers Based on Improved Size Homogeneity Obtained by Comprehensive Growth Optimization. *ACS Photonics* (2025).
105. Yu, X. *et al.* Optically enhanced single- and multi-stacked 1.55 μm InAs/InAlGaAs/InP quantum dots for laser applications. *Journal of Physics D: Applied Physics* **56**, 285101 (2023).
106. Wang, B. *et al.* InAs quantum dots with a narrow photoluminescence linewidth for a lower threshold current density in 1.55 μm lasers. *Optical Materials Express* **14**, 1074 (2024).
107. Jin Soo Kim *et al.* InAs-InAlGaAs quantum dot DFB lasers based on InP [001]. *IEEE Photonics Technology Letters* **18**, 595–597 (2006).
108. Duan, J. *et al.* Narrow spectral linewidth in InAs/InP quantum dot distributed feedback lasers. *Applied Physics Letters* **112** (2018).
109. Septon, T. *et al.* Large linewidth reduction in semiconductor lasers based on atom-like gain material. *Optica* **6**, 1071 (2019).
110. Kaneko, R. *et al.* Fabrication and Temperature Characteristics of 1550nm InAs/InGaAlAs Quantum Dot Distributed Feedback Lasers with Side Grating in 2022 Compound Semiconductor Week (CSW) (IEEE, Ann Arbor, MI, USA, 2022), 1–2.

111. Mason, B., Barton, J., Fish, G., Coldren, L. & Denbaars, S. Design of sampled grating DBR lasers with integrated semiconductor optical amplifiers. *IEEE Photonics Technology Letters* **12**, 762–764 (2000).
112. Nikawa, K. Applications of focused ion beam technique to failure analysis of very large scale integrations: A review. *Journal of Vacuum Science & Technology B: Microelectronics and Nanometer Structures Processing, Measurement, and Phenomena* **9**, 2566–2577 (1991).
113. Harriott, L. R., Wagner, A. & Fritz, F. Integrated circuit repair using focused ion beam milling. *Journal of Vacuum Science & Technology B: Microelectronics Processing and Phenomena* **4**, 181–184 (1986).
114. Langford, R. M. & Petford-Long, A. K. Preparation of transmission electron microscopy cross-section specimens using focused ion beam milling. *Journal of Vacuum Science & Technology A: Vacuum, Surfaces, and Films* **19**, 2186–2193 (2001).
115. Hopman, W. C. L. *et al.* Focused ion beam scan routine, dwell time and dose optimizations for submicrometre period planar photonic crystal components and stamps in silicon. *Nanotechnology* **18**, 195305 (2007).
116. Kou, J.-l., Qiu, S.-j., Xu, F. & Lu, Y.-q. Demonstration of a compact temperature sensor based on first-order Bragg grating in a tapered fiber probe. *Optics Express* **19**, 18452 (2011).
117. Seliger, R. L., Ward, J. W., Wang, V. & Kubena, R. L. A high-intensity scanning ion probe with submicrometer spot size. *Applied Physics Letters* **34**, 310–312 (1979).
118. Rennon, S. *et al.* High-frequency properties of 1.55 μm laterally complex coupled distributed feedback lasers fabricated by focused-ion-beam lithography. *Applied Physics Letters* **77**, 325–327 (2000).
119. Reithmaier, J. P., Bach, L. & Forchel, A. Focused Ion Beam Technology for Optoelectronic Devices. *AIP Conference Proceedings* **680**, 584–587 (2003).
120. Bischoff, L., Pilz, W., Mazarov, P. & Wieck, A. D. Comparison of bismuth emitting liquid metal ion sources. *Applied Physics A* **99**, 145–150 (2010).
121. Kollmer, F. Cluster primary ion bombardment of organic materials. *Applied Surface Science* **231-232**, 153–158 (2004).
122. Klingner, N. *et al.* Imaging and milling resolution of light ion beams from helium ion microscopy and FIBs driven by liquid metal alloy ion sources. *Beilstein Journal of Nanotechnology* **11**, 1742–1749 (2020).

123. Salmond, B. *et al.* Fabricating distributed feedback laser gratings with bismuth and gold focused ion beams. *Journal of Vacuum Science & Technology B* **42**, 062214 (2024).
124. Yamaguchi, H., Shimase, A., Haraichi, S. & Miyauchi, T. Characteristics of silicon removal by fine focused gallium ion beam. *Journal of Vacuum Science & Technology B: Microelectronics Processing and Phenomena* **3**, 71–74 (1985).
125. Frey, L., Lehrer, C. & Ryssel, H. Nanoscale effects in focused ion beam processing. *Applied Physics A* **76**, 1017–1023 (2003).
126. Ozolins, O. *et al.* 100 GHz Externally Modulated Laser for Optical Interconnects. *Journal of Lightwave Technology* **35**, 1174–1179 (2017).
127. Weldon, V., O’Gorman, J., Phelan, P., Hegarty, J. & Tanbun-Ek, T. H₂S and CO₂ gas sensing using DFB laser diodes emitting at 1.57 μ m. *Sensors and Actuators B: Chemical* **29**, 101–107 (1995).
128. Li, P. *et al.* Recent advances in optical gas sensors for carbon dioxide detection. *Measurement* **239**, 115445 (2025).
129. Sun, Y. *et al.* DFB laser array based on four phase-shifted sampled Bragg gratings with precise wavelength control. *Optics Letters* **47**, 6237 (2022).
130. Fan, Y. *et al.* Dual-wavelength distributed feedback laser array based on four-phase-shifted sampled Bragg grating for terahertz generation. *Optics Letters* **49**, 3472 (2024).
131. Gatilova, L., Bouchoule, S., Guilet, S. & Chabert, P. Investigation of InP etching mechanisms in a Cl₂/H₂ inductively coupled plasma by optical emission spectroscopy. *Journal of Vacuum Science & Technology A: Vacuum, Surfaces, and Films* **27**, 262–275 (2009).
132. Bliznetsov, V., Lin, H. M., Zhang, Y. J. & Johnson, D. Deep SiO₂ etching with Al and AlN masks for MEMS devices. *Journal of Micromechanics and Microengineering* **25**. Publisher: IOP Publishing, 087002 (2015).

Appendix A

Process Flows

A.1 Process flow for Chapter 6

Table A.1: Detailed process flow for the fabrication of low open area LC-DFB lasers with projection lithography.

Step No.	Name	Details
1	Tile Preparation	Cleave wafer into 15x15 mm tiles
2	Solvent Cleaning	Acetone, Methanol, IPA
3	Hard Mask Deposition	Deposit 300 nm SiO ₂ hard mask using e-beam deposition
4	Spin-coat Resist	AZ2020 - 45 s @ 5000 rpm
5	Soft Bake	1 min @ 110 °C
6	Exposure	Expose gratings in DMO ML3 projection lithography system
7	Post-expose Bake	2 mins @ 115 °C
8	Development	90 s immersion in AZ726 developer
9	Plasma Ash	2 mins @ 50 W
10	Etch Hard Mask	ICP-RIE, Chemistry: C4F8+O2
11	Strip Resist	NMP1165 followed by solvent clean + Ash
12	Spin-coat Resist	AZ2020 - 45 s @ 5000 rpm
13	Soft Bake	1 min @ 110 °C
14	Exposure	Expose ridges in DMO ML3 projection lithography system
15	Post-expose Bake	2 mins @ 110 °C
16	Development	90 s immersion in AZ726 developer
17	Ridge Mask Deposition	Deposit 500 nm SiO ₂ hard mask using e-beam deposition
18	Strip Resist	NMP1165 followed by solvent clean + Ash
19	Etch Epi	ICP-RIE, Chemistry: Cl2 + Ar
20	Mask Removal	ICP-RIE, Chemistry: C4F8+O2
21	BCB Spin-coat	BCB 3022-57 - 45 s @ 4000 rpm
22	Partial-Cure	40 mins @ 210 °C in N2
23	BCB Back Etch	RIE, Chemistry: SF6 + O2
24	Solvent Cleaning	Acetone, Methanol, IPA
25	Plasma Ash	5 mins @ 100 W
26	Spin-coat Resist	AZ2035 - 45 s @ 5000 rpm
27	Soft Bake	1 min @ 110 °C

Step No.	Name	Details
28	Exposure	Expose oxide stripe in DMO ML3 projection lithography system
29	Post-expose Bake	2 mins @ 110 °C
30	Development	90 s immersion in AZ726 developer
31	Plasma Ash	2 mins @ 50 W
32	Dielectric Deposition	Deposit 300 nm SiO ₂ dielectric using e-beam deposition
33	Lift-off	Strip resist in NMP1165
34	Solvent Cleaning	Acetone, Methanol, IPA
35	Spin-coat Resist	AZ2035 - 45 s @ 5000 rpm
36	Soft Bake	1 min @ 110 °C
37	Exposure	Expose p-contacts in DMO ML3 projection lithography system
38	Post-expose Bake	2 mins @ 110 °C
39	Development	90 s immersion in AZ726 developer
40	Plasma Ash	2 mins @ 50 W
41	P-Contact Deposition	Ti/Pt/Au - 10/15/500 nm
42	Lift-off	Strip resist in NMP1165
43	Solvent Cleaning	Acetone, Methanol, IPA
44	Lapping	Thin sample to 120 μm and polish
45	N-contact deposition	AuGe/Ni/Au - 100/28/300 nm
46	Hard Cure BCB	60 mins @ 300 °C
47	Anneal Contacts	5 mins @ 350 °C
48	Sample Prep	Cleave and Mount onto TO-8 headers

A.2 Process flow for Chapter 6

Table A.2: Detailed process flow for the fabrication of high open area LC-DFB lasers.

Step No.	Name	Details
1	Tile Preparation	Cleave wafer into 15x15 mm tiles
2	Solvent Cleaning	Acetone, Methanol, IPA
3	Hard Mask Deposition	Deposit 300 nm SiO ₂ hard mask using e-beam deposition
4	Spin-coat Resist	EBR:AZ2020 (7:10g) - 45 s @ 5000 rpm
5	Soft Bake	1 min @ 110 °C
6	Exposure	Expose ridge +grating using EBL
7	Post-expose Bake	2 mins @ 110 °C
8	Development	120 s immersion in AZ726 developer
9	Etch Hard Mask	ICP-RIE, Chemistry: C4F8+O2
10	Strip Resist	NMP1165 followed by solvent clean + Ash
11	Etch Epi	ICP-RIE, Chemistry: Cl2 + Ar
12	Mask Removal	ICP-RIE, Chemistry: C4F8+O2
13	Solvent Cleaning	Acetone, Methanol, IPA
14	Plasma Ash	5 mins @ 100 W
15	BCB Spin-coat	BCB 3022-57 - 45 s @ 4000 rpm
16	Partial-Cure	40 mins @ 210 °C in N2
17	BCB Back Etch	RIE, Chemistry: SF6 + O2
18	Solvent Cleaning	Acetone, Methanol, IPA
19	Plasma Ash	5 mins @ 100 W
20	Spin-coat Resist	AZ2035 - 45 s @ 5000 rpm
21	Soft Bake	1 min @ 110 °C
22	Exposure	Expose p-contacts in MLA150 projection lithography system
23	Post-expose Bake	2 mins @ 110 °C
24	Development	90 s immersion in AZ726 developer
25	Plasma Ash	2 mins @ 50 W
26	P-Contact Deposition	Ti/Pt/Au - 10/15/500 nm
27	Lift-off	Strip resist in NMP1165
28	Solvent Cleaning	Acetone, Methanol, IPA
29	Lapping	Thin sample to 120 μm and polish
30	N-contact deposition	AuGe/Ni/Au - 100/28/300 nm
31	Hard Cure BCB	60 mins @ 300 °C
32	Anneal Contacts	5 mins @ 350 °C
33	Sample Prep	Cleave and Mount onto TO-8 headers